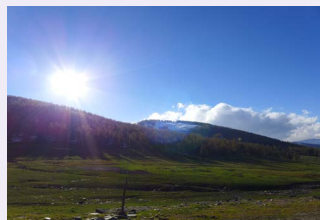


中国气象科学研究院年报

ANNUAL REPORT OF CAMS



2015



中国气象科学研究院

Chinese Academy of Meteorological Sciences



中国气象科学研究院年报 2015

主办单位：中国气象科学研究院
编辑出版：《中国气象科学研究院年报》编辑部
主 编：端义宏
执行主编：袁凤杰
制作印刷：北京永峰印刷有限责任公司
地 址：北京中关村南大街 46 号，邮编 100081
http: //qikan.camscma.cn
Email: kjdt@camscma.cn

ANNUAL REPORT OF CAMS 2015

Sponsor: Chinese Academy of Meteorological Sciences
Publication: Annual Report of CAMS Editorial Division
Chief Editor: Duan Yihong
Executive Chief Editor: Yuan Fengjie
Design and Printing: Beijing Yongzheng Printing Ltd. Co.
Address: 46 Zhongguancun Nandajie, Beijing, 100081, China
http: //qikan.camscma.cn
Email: kjdt@camscma.cn

中国气象科学研究院年报
ANNUAL REPORT OF CAMS

2015

中国气象科学研究院
Chinese Academy of Meteorological Sciences

目 次

科研成果与进展

灾害天气	4
气候系统与气候变化	18
大气探测与雷电防护	26
大气物理与人工影响天气	38
生态环境与农业气象	53
大气成分和大气化学	67

消息与动态	89
-------------	----

2015 年新项目	102
-----------------	-----

人才培养	106
------------	-----

合作与交流	110
-------------	-----

2015 年出版物	118
-----------------	-----

Scientific Achievements and Advances

Severe Weather	4
Climate System and Climate Change	18
Atmospheric Sounding and Lightning Protection	26
Atmospheric Physics and Weather Modification	38
Ecological Environment and Agrometeorology	53
Atmospheric Composition and Atmospheric Chemistry	67
News and Notes	89
New Projects in 2015	102
Education and Training	106
Cooperation and Communication	110
Publications in 2015.....	118

灾害天气研究进展

1 灾害天气监测与资料应用

1.1 X波段相控阵天气雷达测试定标方法和对流过程观测外场试验初步结果分析

中国气象科学研究院灾害天气国家重点实验室与安徽四创电子股份有限公司联合研发了专门用于快速观测对流过程、具有多波束观测能力的X波段相控阵天气雷达(XPAR)。该雷达利用相控阵技术实现垂直扫描,水平扫描采用机械扫描,能够发射 20° 的宽波束,并同时接收14层探测数据。XPAR采用3种观测模式进行观测:警戒模式(GM)、快速扫描模式(QM)和精细观测模式(FM)。3个模式的天线方向见图1。

根据有源相控阵雷达的体制特点,参考多普勒天气雷达测试定标方法,提出了一维(1D)扫描有源相控阵天气雷达的测试和定标方法,将测试重点放在了天馈系统、T/R组件、脉冲压缩、动态范围的测试和定标上,以解决不同观测模式、不同波位的天线增益等参数变化引起的回波强度测量误差问题。该雷达经过测试和定标后,于2014年5—8月分别在安徽定远和四川甘孜县进行外场试验,1部S波段多普勒天气雷达(SA)和1部C波段双线偏振雷达(C-POL)也在XPRA周边进行观测,以便分析XPAR的探测能力。测试结果表明:XPAR天馈系统在不同观测模式下的天线参数随仰角的变化情况、波束指向的准确度、T/R组件的动态范围等均符合设计要求,128个T/R组件的发射和接收性能比较一致,在外场试验观测期间T/R组件发射和接收性能的改变可通过校正网络作实时测试和校正;回波强度和径向速度定误差分别小于0.98 dB和0.1 m/s。与附近SA和C-POL雷达观测数据的对比分析结果表明,XPAR以FM模式观测的回波强度偏差小于1.0 dB,GM和QM模式的观测误差小于2.0 dB,3种观测模式观测的径向速度非常一致,XPAR观测的回波强度和径向速度的偏差在合理范围内。XPAR3种模式观测的强回波的水平位置和垂直位置、结构和系统误差均比较一致,数据可靠。这一定标结果为该雷达的定量应用提供了基础。

该雷达与C波段双线偏振雷达(C-POL)于2013年4—6月在广东省江门市鹤山站进行了对比观测试验,以检验该雷达观测模式及其对快速变化的对流云演变过程的观测能力,为进一步改进雷达观测模式提供依据。利用实测数据对比分析了3种观测模式观测的回波结构、灵敏度,并与C波段双线偏振雷达数据进行了对比,详细分析了2013年5月30日一次中尺度线状对流系统后部单体的发展和消亡过程,讨论了XPAR分钟级数据在对流过程演变中的作用。图2给出了XPAR以FM模式观测的2013年5月30日15:13—15:32时段对流过程发展的 3.5° 仰角回波强度和径向速度的PPI,图3为沿 64° 方位的RHI,时间间隔为1 min。

观测数据结果表明:(1)XPAR3种观测模式获取的降水回波结构合理,实现了在1 min内完成一个高空间分辨率体扫的探测功能,数据的时空分辨率远高于现有的机械扫描雷达;(2)XPAR的精细观测模式数据揭示了单体触发、发展和演变过程,清晰给出了2次径向辐合发展过程及其与回波发展的关系,给出了新一代天气雷达和C波段双线偏振雷达不能提供的新的事实;(3)XPAR分钟级数据对进一步认识对流单体内部 γ 中尺度及其更小尺度系统的发展和演变有很大的帮助(图1~3)。(刘黎平)

1.2 基于雷达三维(3D)拼图的灾害天气监测预警技术研发与推广应用

继续推进雷达三维(3D)拼图的灾害天气监测预警技术的发展和成果在业务单位的应用。研究了飊线大风识别预警方法,集成到雷达3D拼图系统中,已在电力部门投入应用,提高输电线路风灾预警能力。开展了雨滴谱数据在提高降水估测能力中的应用研究,改进了区域雷达网降水估算、降水预报效果,并增加了效果检验功能。在苏州市气象局、山西省气象局投入业务运行,提供精细化的降水监测和预警产品,今年在2个单位分别完成了项目的验收工作。此外,在华北空管局、贵州省人工影响天气办公室的推广工作仍在开展中,华北空管局的推广增加了机场雷达数据解读和拼图的处理功能,定制了航空管制区强对流定点监测和预警产品,在贵州省人工影响天气办公室的推广给出了降雹概率产品。在复杂地形条件下组网雷达估算降水的回波提取方法研究方面也完成了系统研发的相关工作,扩展新方法的雷达3D拼图系统已处于试运行阶段。完成了重点地区的业务天气雷达网有效覆盖区域的评估工作,给出了评估结果,为有效地发挥雷达组网监测预警作用提供了科学依据(图4)。(王红艳)

1.3 基于3DVar的区域雷达组网风场反演技术成果转化

首批参与中国气象局科研业务结合试点项目的3DVar雷达组网风场反演技术通过了2年的新技术测试后,于2015年初经推荐加入国家级短时临近预报系统(SWAN),9月底获得SWAN算法准入许可,第1版本的集成工作已于12月底基本完成。雷达风场产品填补了此前SWAN系统中雷达风场监测产品的空缺(图5)。(王红艳)

1.4 风廓线雷达相关研究与成果推广应用

将研发的全国风廓线雷达数据质量控制方法集成到广东省的业务系统中,并于2015年投入实时业务应用,从而为广东省业务应用的风廓线雷达网观测数据的质量提供支撑。风廓线雷达数据发布系统于2015年在江西省气象局气象业务中使用,为其提供了风廓线雷达网观测数据预处理和Web共享平台。同时还开展了风廓线资料与天气雷达VWP资料的对比融合研究。(王红艳)

1.5 不同背景场资料应用效果研究

通过对强降水个例和1个月的连续模式积分,开展了FNL和ERA-Interim两种背景场资料在华南区域再分析中的应用效果对比试验。结果表明,FNL对华南地区低层的温度场预报略优于ERA-Interim,但对风场和形势场,ERA-Interim明显好于FNL。(王东海,刘英)

1.6 风廓线以及卫星观测资料的同化效果对比试验研究

风廓线的对比试验结果表明,进行质量控制后的风廓线资料与背景场偏差明显减少,消除了小频率的大偏差事件,风廓线资料的质量控制直接影响其同化效果。同化风廓线资料后,对低层风场改进明显,激发上升运动,从而改进了降水的预报效果。基于AMSU-A、MHS和ATMS3种卫星观测资料分别对同化方法(3DVar、混合)和不同循环同化方案进行了对比试验,结果表明混合的同化效果明显优于3DVar,同化ATMS的效果要好于同化AMSU-A和MHS。(王东海,刘英,尹金方,梁钊明)

2 灾害天气结构与形成机理

2.1 涡旋初始结构对热带气旋(TC)快速加强的影响

基于1988—2012年北大西洋热带气旋(TC)最佳路径资料发现,初始涡旋的尺度和强度会影响后期TC的加强速度,特别是快速加强的速度。当TC强度小于(大于)70~80 kt时,加强速度与强度成正(反)相关。并与TC尺度及外核宽度(用34 kt半径减去最大风半径来表示)呈明显的反相关,即

初始涡旋尺度越大,眼墙到外核的宽度越宽,则TC加强速度越小。TC在加强过程中存在最大可能加强速度,统计事实表明,最大加强速度发生在强度80 kt左右、最大风半径(RMW)40 km左右,外核尺度(34 kt半径)及涡旋宽度在150 km左右。上述分析结果的应用价值在于证明了涡旋的强度以及尺度参数都是TC强度预报中的重要因子(图6)。(徐晶)

2.2 一次梅雨期暴雨过程中尺度可预报性及对流初生机制

借助显示对流集合模拟手段探讨了2007年7月8日夜间至次日上午淮河流域特大暴雨的中尺度可预报性问题。结果表明,尽管特大暴雨发生在天气尺度系统(梅雨锋、西太平洋副热带高压)强迫的背景下,降水模拟对初始场不确定性十分敏感,初始场的微小差异可显著影响中尺度对流系统(MCS)生成与否及其造成的地面累积降水的整体分布、强降水落区和降水极值的位置和大小。与减小初始温度场和风场的误差相比,减小初始水汽场误差可以更加显著地改善降水模拟,但是,强降水模拟的显著改善需要初始水汽场、温度场和风场的协同改善。模式物理参数化方案不确定性对降水模拟的影响不如初始场误差影响显著,但是可以显著影响强降水的精确落区和降水极值的大小。结合观测分析,证实了前一日下午至傍晚的降水在梅雨锋前遗留下的中尺度冷空气堆对于夜间对流触发的重要性,该冷空气堆帮助夜间加强的边界层内西南气流带来的高相当位温空气沿等熵面抬升,达到其自由对流高度发生对流。前一日下午至傍晚降水、夜间对流触发、上午强降水之间的关联反映了梅雨降水日变化(上午和下午)2个峰值之间物理机制方面的一种联系(图7)。(罗亚丽)

2.3 山东半岛冷流强降雪和非冷流强降雪的对比分析

利用1981—2000年常规气象观测资料和NCEP/NCAR再分析资料,采用合成分析和动力诊断分析方法,对山东半岛冷流强降雪与非冷流强降雪的空间分布、大气环流、水汽输送、稳定性和垂直运动进行对比分析。结果表明,冷流强降雪是发生在槽后西北气流里的中小尺度不稳定降雪,非冷流强降雪是发生在槽前西南气流中大尺度稳定性降雪。冷流强降雪具有明显的地方性特点,是强冷空气对下垫面物理状态强迫响应的结果。提出强冷空气与渤海暖水面相互作用产生的大气边界层不稳定是产生冷流降雪的本质,在这种边界层不稳定层结中发生的降雪是冷流降雪的概念。(施晓晖)

2.4 华南暖区暴雨发生发展机制及关键预报技术

华南西部降水日变化的峰值出现在清晨,与位于华南西部的低空西南急流夜间增强有关;华南东部降水日变化的峰值在午后,大多与地面加热导致的局地深对流有关。暖区暴雨的环境场特征为整层相对湿度较高,500 hPa以下为显著湿层;CAPE值普遍高于1500 J/kg,抬升指数普遍低于-4;850—400 hPa中层风场为较为一致的西南气流,同时具有弱的顺转。形成暖区暴雨的对流系统以多种形态的线状对流、低涡背景下的涡旋对流雨带等结构较为常见,华南沿海地区的中尺度地形对触发线状对流可能起着重要作用。对流涡度矢量、湿热力平流参数、广义 Q 矢量散度与暖区降水的相关性最好,对强降水过程的发展演变具有一定的预报能力。(姜智娜)

2.5 青藏高原的“气候调节”作用

中国东部夏季暴雨频数变化可描述出清晰年际和年代际特征,中国东部区域暴雨极端事件、亚洲季风年际与年代际变化均受到青藏高原动力和热力强迫因素的调制。研究亦表明,中国北方夏季暴雨频数与水汽输送通量及其“涡度带”密切相关,水汽通道及其“涡度带”可由青藏高原北缘延伸至下游地区,高原南北侧西风急流及其水汽输送大地形绕流结构调制着中国东部暴雨的时空分布。另外,观测和模式研究揭示了青藏高原热源的年际变化与中国东部霾天气亦相关显著。高原的热源效应可影响中国东部大气热力结构及季风环流强度,从而导致中国暴雨时空分布的变化,而且调制着霾灾害天气的变异。研究结果表明,青藏高原大地形动力、热力因素对于大气环流及其气候变化影响理论研

究,有助于对东亚与中国区域灾害天气气候的异常和霾天气频发的新认知。(徐祥德,赵阳,王寅钧)

3 数值天气预报和模式关键技术

3.1 模式区域和物理参数设置研究

利用欧洲中期天气预报中心(ECMWF)提供的ERA-Interim再分析资料计算了近10年(2005—2014年)12个月的月平均高低空的风、湿、压等要素场($0.25^{\circ} \times 0.25^{\circ}$),分析了东亚大区域近10年平均的高中低层形势场、高层急流和低层水汽通量输送的分布特征。重点关注了东亚大槽、西伯利亚高压脊、副热带高压、南亚高压、高空急流以及西南季风及副热带高压西侧东南风的水汽输送的分布特征。在尽量覆盖这些系统的分布演变情况下,确定了东亚区域再分析的区域,包括区域的中心经纬度、范围大小、参考经度、投影参数和分辨率等主要模式基本参数。在此基础上,通过调试工作确定了模式的参数设置,包括垂直层次、模式层顶、地表参数输入资料、动力参数和各物理参数方案。(王东海,梁钊明,尹金方)

3.2 青藏高原的云微物理及降水模拟研究

利用第3次青藏高原试验(TIPEX-III)期间的地基云雷达、偏振雷达资料,分析了2014年7月22日高原积层混合云发展演变全过程的云微物理特征,评估了WRF-CAMS云微物理方案的模拟能力,讨论了云微物理过程对高原云降水发展的影响。WRF-CAMS微物理方案合理地再现了24 h降水分布;模拟的C波段及Ka波段雷达反射率与观测基本一致;模拟的雨滴谱截距值在对流区较小,对流区的雨滴尺寸较层云区偏大,与偏振雷达观测一致。敏感试验表明,即使高原对流云下部的液水层很薄,暖云微物理过程仍起着重要的作用。不包含冰云过程(NICE)将导致云水含量及地面降水增加,但在较强对流时由于缺乏冰相物的融化,又会造成地面降水减小;增加云滴凝结(COND),导致降水强度及降水面积增加,结果与观测降水最为接近,反映了云凝结过程的重要性;减少雨滴蒸发(EVAP),导致降水面积最显著的增加;增加初始云滴尺寸(NUMB),导致云水及降水减弱,与云滴凝结作用相反。(高文华)

3.3 理想化盆地地区环流的数值模拟研究

利用理想化数值模拟考察盆地环流情况,工作重点在水平闭合涡旋和垂直环流的特征。当气流流过盆地地形时,会在盆地中低层产生回流,在水平方向形成闭合涡旋。本研究考察了盆地形状对环流的影响,具体而言,包括盆地深度、盆地坡度和盆地宽度对涡旋和回流的影响。科氏力的影响方面,在北半球,计算结果表明正涡度环流的范围随着纬度的升高而增大。日变化加热源影响方面,日变化的下垫面加热带来了水平辐合、辐散。当日变化加热强度足够大的时候,夜间盆地内的水平环流由辐合、辐散取代闭合涡旋。同时,增加日变化加热也改变了垂直环流的结构,在最大冷却时,盆地内出现逆时针环流(图8)。(钱婷婷)

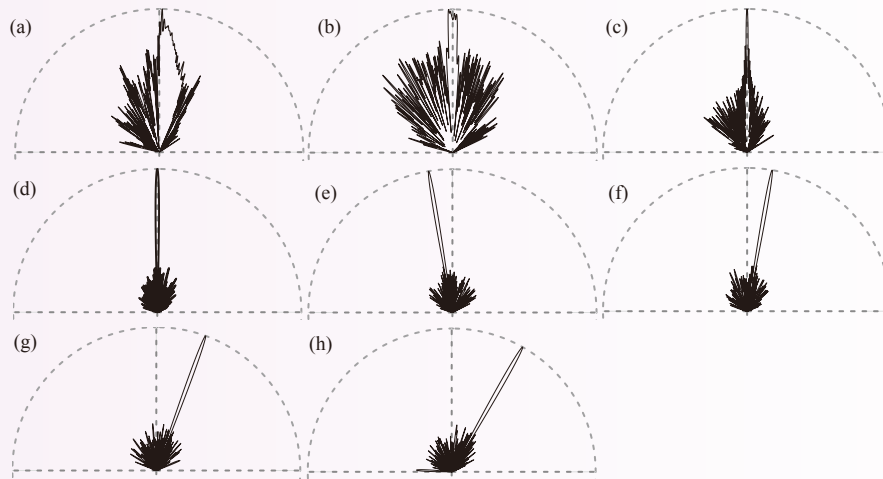


图1 X波段相控阵天气雷达(XPAR)归一化方向:(a)GM模式发射波形;(b)QM模式发射波形;(c)FM模式发射波形;(d)0°仰角的接收波形;(e)-9.5°仰角的接收波形;(f)9.5°仰角的接收波形;(g)19.5°仰角的接收波形;(h)29.5°仰角的接收波形

Fig. 1 Normalized directivity diagram of XPAR: (a) The emitting waveforms for GM; (b) The emitting waveforms for QM; (c) The emitting waveforms for FM; (d) The receiving waveforms for elevations of 0°; (e) The receiving waveforms for elevations of -9.5°; (f) The receiving waveforms for elevations of 9.5°; (g) The receiving waveforms for elevations of 19.5°; (h) The receiving waveforms for elevations of 29.5°

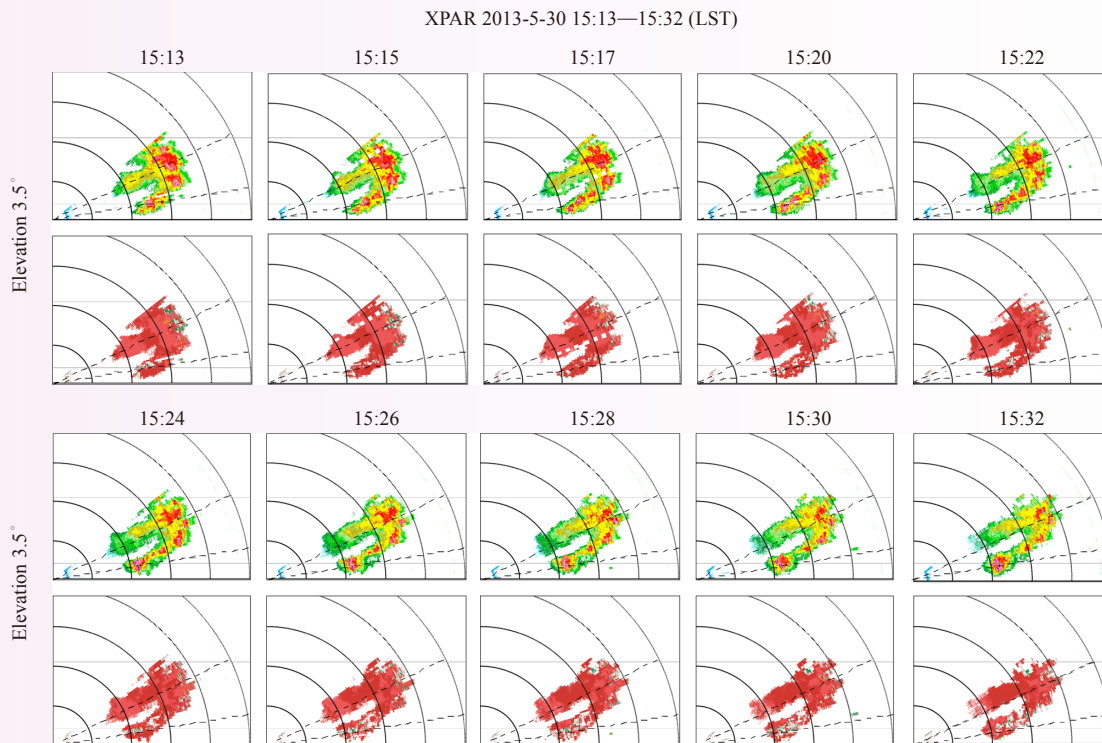


图2 X波段相控阵天气雷达(XPAR)以FM模式观测的2013年5月30日15:13—15:32时段对流过程发展的3.5°仰角回波强度和径向速度的PPI(时间间隔为2 min)

Fig. 2 Sequence of reflectivity and radial velocity at elevation of 3.5° between 15:13 and 15:32 observed by XPAR with FM mode. The temporal interval of PPI is 2 min

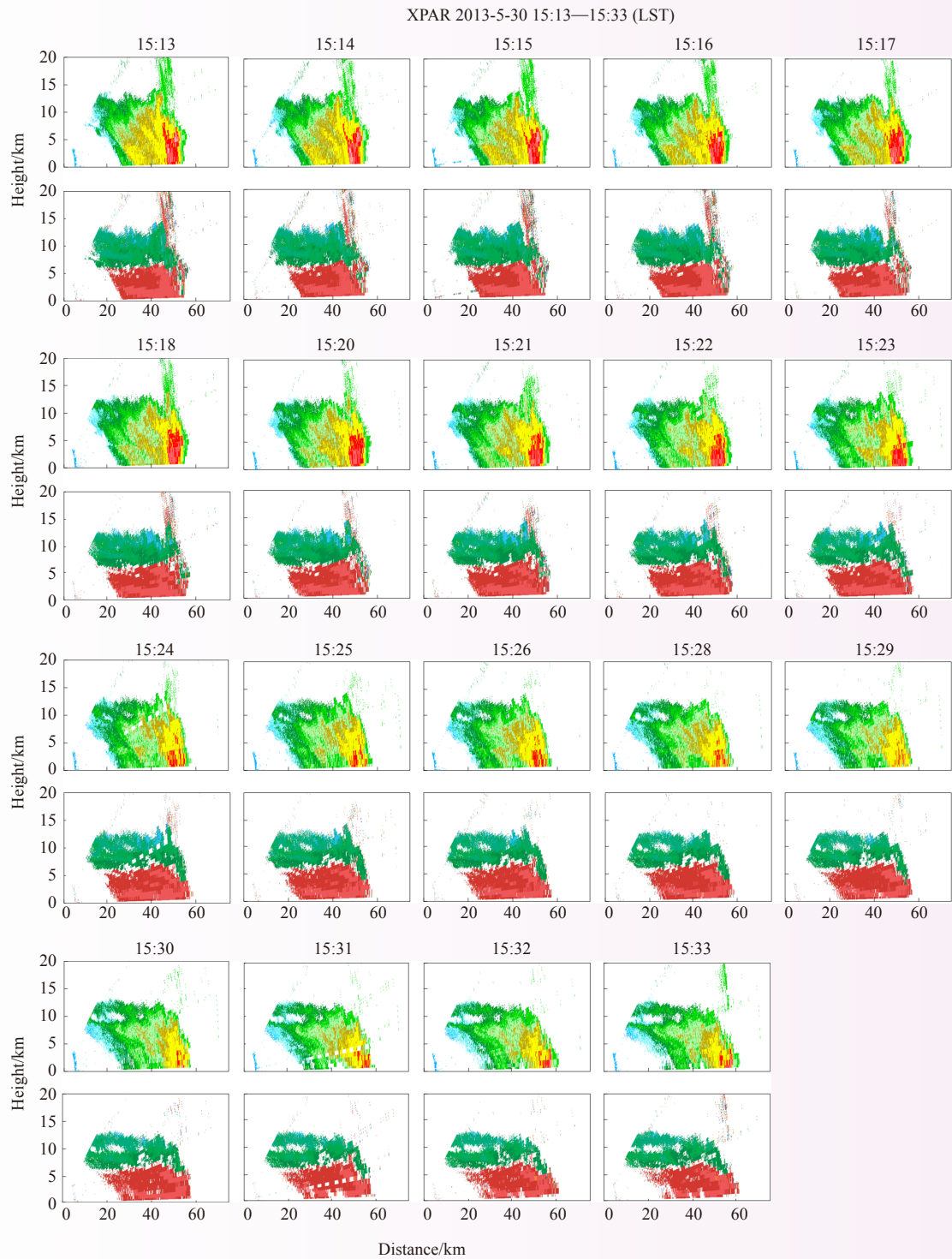


图3 与图2对应时段的沿64°方位的RHI (时间间隔为1 min)

Fig. 3 The RHI for reflectivity and radial velocity along azimuthal direction of 64°. The temporal interval is 1 min

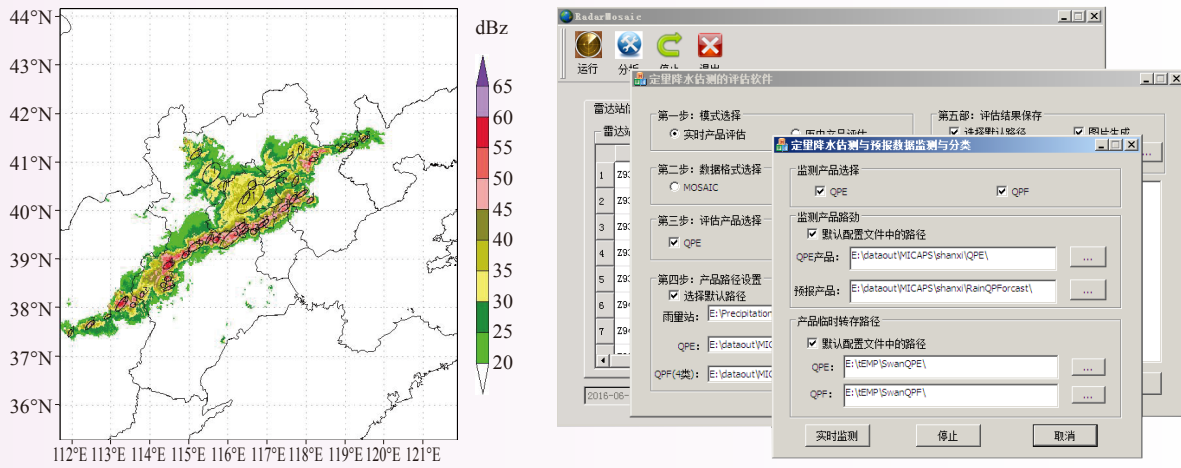


图4 飚线大风识别预警产品、降水估算效果检验功能实例
Fig. 4 The squall line wind detection and warning products and QPE effect testing software

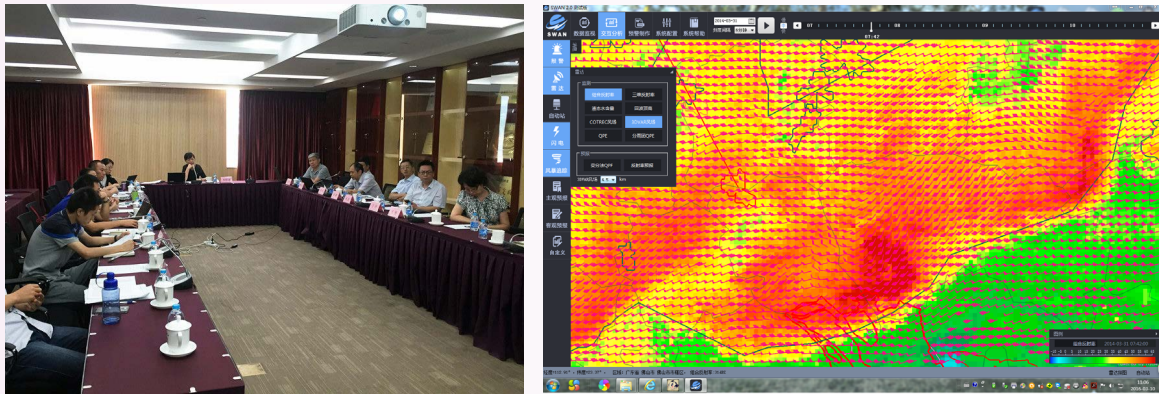


图5 雷达风场反演技术通过SWAN准入评审及集成后的风场产品
Fig. 5 Appraisal meeting for 3DVar regional wind method and integrated wind product of SWAN

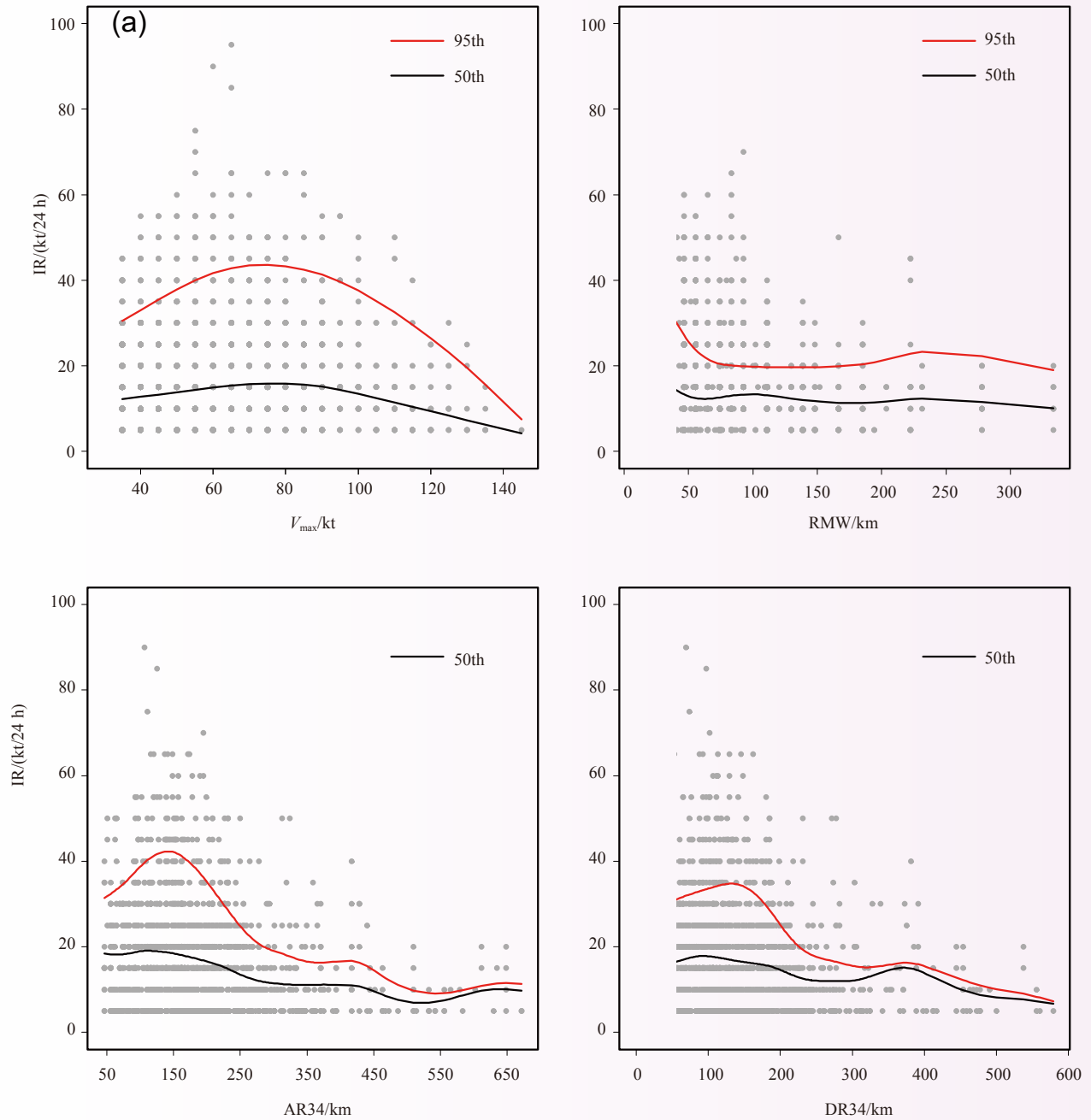


图 6 热带气旋 (TC) 的 24 h 加强速率 (IR) 与最大风速 V_{max} (a)、最大风半径 RMW (b)、34 kt 风半径 AR34 (c) 及最大风半径到 34 kt 风半径距离 DR34 (AR34-RMW) (d) 对应关系的散点图 (图中红色和黑色曲线表示样本所示 TC 的加强速度)

Fig. 6 Scatter diagrams of the subsequent 24 h IR against (a) storm intensity (V_{max} in terms of the max 1-min mean sustaining 10 m wind speed), (b) RMW, (c) AR34, and (d) DR34 (AR34-RMW). Red and black curves are the 95th and 50th percentiles of the IR for a given storm intensity in (a) and various size parameters in (b)-(d), respectively

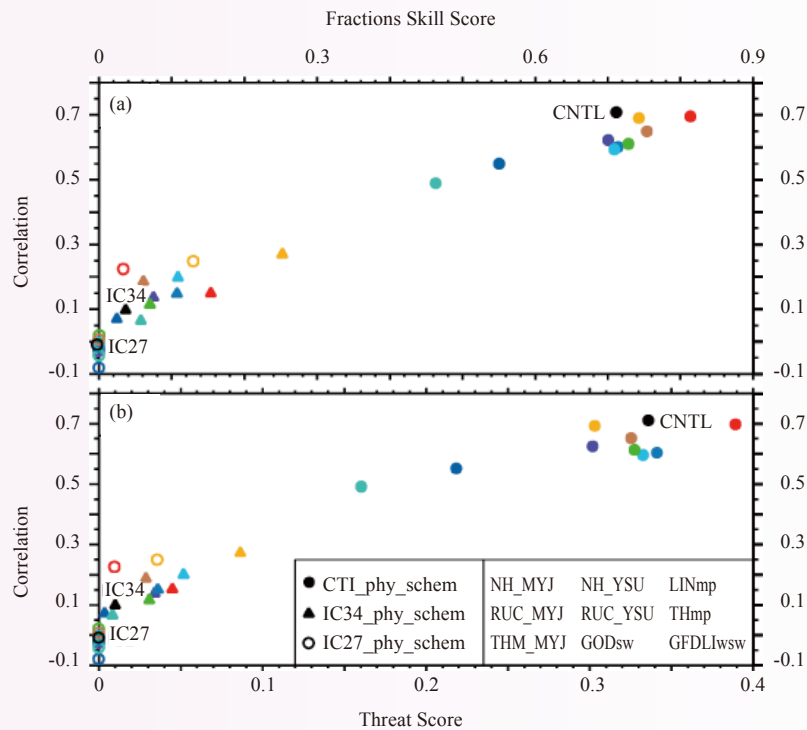


图 7 (a) 大于50 mm降水、56 km半径的FSS评分以及模拟和观测降水的空间相关系数(CC)，(b)大于50 mm降水的TS评分以及CC(点、空心圆、三角形分别代表3组采用不同初始场的数值试验，每一组包含9个不同的颜色，代表9个采用不同的物理过程参数化方案组合的试验)

Fig. 7 (a) Fraction skill score (FSS) applied to a 50 mm precipitation threshold with a neighborhood size of 56 km, and a spatial correlation coefficient of rainfall for the physics-scheme-sensitivity experiments with the same initial conditions as CNTL (dots), IC34 (triangles) and IC27 (circles). (b) As in Fig. 1a, the threat score (TS) applied to a 50 mm precipitation threshold is shown with the correlation coefficient. Colors denote the 9 different combinations of physical parameterization schemes used in the experiments

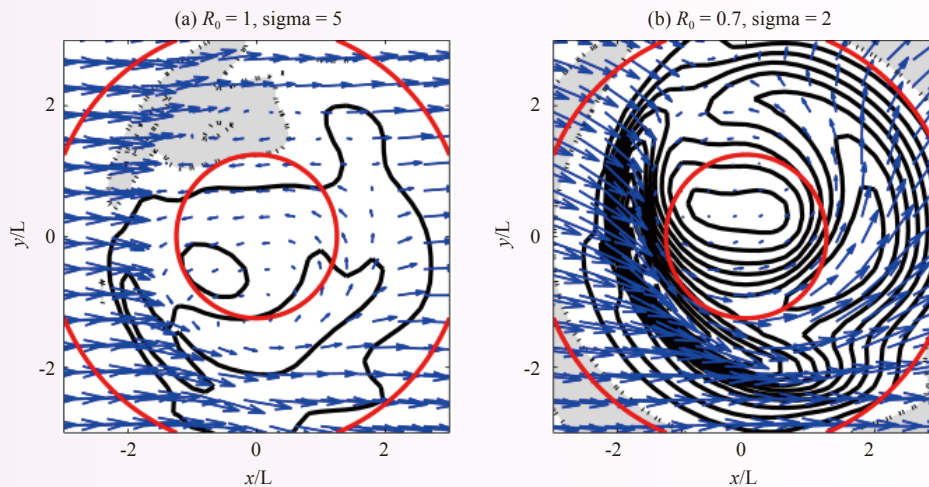


图 8 水平涡度随纬度的变化: (a) 30°N; (b) 45°N

Fig. 8 Horizontal distribution of low-level wind vectors and z-component vorticity (contour interval=0.1; solid lines: positive; dashed lines: negative and zero) at latitudes of (a) 30°N and (b) 45°N

Advances in Severe Weather Research

1 Severe weather monitoring technology and data application

1.1 The calibration methods and application of X band active phased-array weather radar

The X band phased-array radar (XPAR) was jointly developed by State key Laboratory of Severe Weather, Chinese Academy of Meteorological Science, and Anhui Sun-create Electronics Limited Company. XPAR scans electronically in elevation while scanning mechanically in azimuth, transmits radar wave with wide beam width (about 20° in vertical direction and 1° in horizontal direction) and receives 14 beams simultaneously. XPAR observes a precipitation system with three modes: Guard Mode, Quick Mode and Fine Mode. The normalized directivity diagram of XPAR for the three modes is shown in Fig.1.

According to the characteristics of the transmitter/receiver (T/R) and the multi-beam work mode, the testing and calibration of the XPAR were presented. The testing and calibration focus on the antennas, T/R, and pulse compress and the variations of gain and beam width, in order to reduce the observation bias introduced by different work modes. After being tested and calibrated, the XPAR was used to observe the 3D structures and evolutions of convective precipitation in field experiment in Dingyuan, Anhui Province and Ganzi, Sichuan Province from May to August 2014. Data observed by a S band operational radar (SA) and a C band polarization radar (C-POL) nearby the XPAR were used to examine the observation capability of the XPAR. The results show that the antenna gain and its variation with the scanning angle, the beam direction, dynamics ranges of T/R are in conformity with the design. The transmitting and receiving characteristics for 128 T/R are similar. The variations of T/R parameters in observation are watched and corrected by the correction network. The calibration biases for reflectivity and radial velocity measurement are less than 0.98 dB and 0.1 m/s, respectively. Comparing with the SA and C-POL, the bias of reflectivity with Fine Mode is less than 1.0 dB, the biases for Guard and Quick Modes are less than 2.0 dB, and the velocities observed by three modes correspond to each other very well. The biases of reflectivity and radial velocity by XPAR are reasonable. The horizontal and vertical structures of precipitation observed by 3 radars are similar. The calibration results inform a quantitative measurement of the XPAR.

XPAR was used to observe convective precipitation in Heshan, Jiangmen City, Guangdong Province from April to June, 2013, in parallel with C-POL in the same site. The SA data were also collected to examine the reflectivity bias of XPAR. The work modes and observation capability for convective precipitation were examined to improve the radar performances. The characteristics of the XPAR and work mode were first introduced. The precipitation structures and reflectivity sensitivities by three work modes were compared with those by C-POL and SA. The XPAR data with temporal resolution of one minute were used to analyze the genesis and evolution of convective cells developing in the rear of the line convection in May 30, 2013. Fig. 2 shows the sequence of reflectivity and radial velocity at elevation of 3.5° between 15:13 and 15:32 observed by XPAR with Fine Mode. The temporal interval of PPI is 2 min. Fig. 3 shows RHI the along azimuthal direction of 64° .

The results indicate that (1) XPAR can catch the main characteristics of 3D structures of precipitation with three work modes, complete one volume scan within 1 min with higher temporal and spatial resolutions than those of C-POL and SA. (2) The XPAR data with Fine Mode can reveal the initiation and evolution of a convective cell in detail, two convergence zones and the relationships with reflectivity structures, which are not observed by C-POL and SA; (3) XPAR data with high temporal and spatial resolutions are helpful to improving

the understanding of the meso- γ and more detailed structures in convective systems (Fig.1–3). (Liu Liping)

1.2 Development and application of severe weather detection and warning technology based on 3D radar mosaic

The severe weather monitoring and warning technology based on 3D radar mosaic was put into further application in 2015. A squall line wind detection method was studied and merged in the software system, which is running in the national electricity sector, improving the ability to warn a wind disaster along electricity lines. The accuracy of QPE and QPF is improved by using DSD data. The function of results verification is added to the application software system, which is running in Suzhou and Shanxi Meteorological Bureaus, to provide detailed QPE and QPF products. Furthermore, their application in North China Regional ATM Bureau and Guizhou Weather Modification Office is being carried out. For North China Regional ATM Bureau, this system processes airport radar data, and provides monitoring and warning products for the designated Aerodrome Areas. For Guizhou, hail probability is provided. Besides, a method of selecting reflectivity for QPE in a complex terrain was researched and integrated into the application software, which is being tested now. The coverage of an operational weather radar network in important regions was assessed to provide scientific support to the role to be played by a functioning weather radar network (Fig. 4). (Wang Hongyan)

1.3 Application of 3DVar regional wind retrieval technology

The 3DVar radar regional wind retrieval method, one of the first members participating in the China Meteorological Administration's program for combination of research and operation, was integrated into the National Short-term Nowcasting System (SWAN) after two-year test. The algorithm, which was recommended to SWAN in the early 2015, was permitted for its integration at the end of September. The first integrated version was finished in December 2015 to fill up a gap in the delivery of radar wind products in SWAN (Fig. 5). (Wang Hongyan)

1.4 Research on and application of wind profile radar

The national wind profile radar data quality control algorithm has been developed and applied in Guangdong Province. It is running in real time in this year to provide good quality data to the wind profile radar network in Guangdong Province. The wind profile radar data distribution system was put into use in Jiangxi Province as a wind profile radar data processing and Web sharing platform. A comparison and merging of wind profile data and weather radar VWP data were also carried out in 2015. (Wang Hongyan)

1.5 Research on the effects of different model background data

The effects of FNL and ERA-Interim reanalysis data on the reanalysis result were investigated based on the model simulation of severe rainfall cases and atmospheric circulation of one month in South China with input of such data. The results indicate that the simulation with FNL shows better low-level temperature forecasting but worse wind and circulation than that with ERA-Interim. (Wang Donghai, Liu Ying)

1.6 Research on the effects of the assimilation of wind profile and satellite data

An experimental result shows that the assimilation of wind profile with quality control leads to a better model output owing to the elimination of large-bias events of a small frequency as the departure between the wind profile and background data is obviously reduced. With the assimilation of wind profile, the low-level wind field is significantly improved, leading to a better motivation of vertical upward motion and thus a better prediction of rainfall. With experimentation of assimilating AMSU-A, MHS and ATMS satellite data with different assimilation methods (3Dvar and Hybrid) and cycle schemes, we found that the assimilation with

Hybrid produces a much better model output than that with 3Dvar and the assimilation of ATMS shows a better effect than that of AMSU-A and MHS. (Wang Donghai, Liu Ying, Yin Jinfang, Liang Zhaoming)

2 Structures and mechanisms of severe weather

2.1 A statistical analysis of the dependence of tropical cyclone intensification rate on the storm intensity and size in the North Atlantic

The dependence of tropical cyclone (TC) intensification rate (IR) on storm intensity and size was statistically analyzed for North Atlantic TCs during 1988–2012. The results show that IR is positively (negatively) correlated with storm intensity (the maximum sustaining near-surface wind speed V_{\max}) when V_{\max} is below (above) 70–80 knots (1 kt=0.51 m s⁻¹), and negatively correlated with storm size in terms of the radius of maximum wind (RMW), the average radius of gale-force wind (AR34), and the outer-core wind skirt parameter DR34 (AR34–RMW). The turning point for V_{\max} of 70–80 kt is explained as a balance between the potential intensification and the maximum potential intensity (MPI). The highest IR occurs for V_{\max} =80 kt, RMW=40 km, and AR34–DR34=150 km. The intensifying TCs of high frequency occur for V_{\max} =80 kt and RMW between 20 and 60 km, AR34=200 km, and DR34=150 km. Rapid intensification (RI) often occurs in a relatively narrow parameter space that covers storm intensity and both inner- and outer-core sizes. In addition, the intensity dependency has also been theoretically justified based on a previously constructed simplified dynamical system for TC intensity prediction (Fig. 6). (Xu Jing)

2.2 Investigation of the predictability and convective initiation mechanism of an extreme rainfall event during the Meiyu season in East China

Uncertainties in forecasting a quasi-linear extreme-rain-producing mesoscale convective system (MCS) along the Meiyu front in East China, during the midnight-to-morning hours on 8 July 2007, were studied using ensembles of convection-permitting simulation. The distribution of the simulated accumulative precipitation and the location and amount of the extreme rainfall reveal a strong sensitivity to uncertainties in the initial state, despite the synoptic environment being favorable for heavy rainfall production. Reducing errors in the initial moisture field lead to more significant improvements in the precipitation simulation compared to reducing errors in the initial temperature and wind fields. However, a significant improvement in extreme rainfall prediction requires simultaneous improvements to the initial moisture, temperature, and wind fields. Sensitivity to physical parameterization representing subgrid-scale processes in the model fails to account for large simulation errors (missing the MCS), which results in a large spread in the location and amount of accumulative rainfall. The fact that the nocturnal convective initiation of the MCS resulting from moist southwesterly monsoonal flows ascends cold domes left behind by convective activity that develops during the previous afternoon-to-evening hours, suggesting a possible linkage between the early morning and late afternoon peaks of the Meiyu rainfall (Fig. 7). (Luo Yali)

2.3 Contrastive analysis of cold-air and non-cold-air strong snowstorms in the Shandong Peninsula

According to the general meteorological observation over the period of 1981–2000 and NCEP/NCAR reanalysis datasets, coupled with a synthesis analysis and a dynamic diagnosis analysis, the paper illustrated the spatial distribution of cold-air and non-cold-air strong snowstorms, atmospheric circulation, vapor transport, stability and vertical movement for a contrastive analysis. Results indicate that cold-air strong snowstorms are meso- and micro-scale snowfalls which occur in a post-trough Northwesterly airflow, while non-cold-air snowstorms occur in a pre-trough southwesterly airflow or a large scale snowfall. Cold-air strong snowstorms,

which are distinctively local, result from physical conditions of an underlying surface response forced by strong cold air. It is proposed in this paper that the instability of atmospheric boundary layers caused by the strong interaction of cold and warm waters of the Bohai Sea is an essential contributor to a cold air snowfall. A snowfall occurring in an instable boundary layer stratification is conceptually termed as a cold air snowfall. (Shi Xiaohui)

2.4 Occurrence mechanism and forecast skill of warm sector heavy rainfall in South China

The west of South China often encounters significant nocturnal-to-morning rainfalls, most of which are generated under the influence of enhanced nocturnal southwesterly low-level jets, while the east of South China is dominated by afternoon rainfall, as a result of surface heating. Features of environmental fields of a warm sector rainstorm are high relative humidity for the whole layer, remarkable wet layer under 500 hPa; CAPE values higher than 1500 J kg^{-1} , the lifting index generally lower than -4°C ; southwesterly airflow in 850–400 hPa with a weak clockwise veering. Various forms of linear convections, and whirl convective rain bands under the background of low vortex are a common structure of warm sector rainstorms, and the meso-scale topography along the southern coastline might play an important role in triggering linear convections. The convective vorticity vector, moist thermal advection parameters, and generalized Q vector divergence correspond well to the warm sector rainstorms, which helps forecast the development of heavy rainfall. (Jiang Zhina)

2.5 “Climate modulation” of the Tibetan Plateau

Summer rain storms in China and East Asia region feature interannual and Interdecadal variations in rainstorm frequency. The heating over the Tibetan Plateau (TP) thermal circulation also significantly impacts the monsoon circulation and the summertime heavy rainfall. The frequency of the summertime heavy rainfall in northern China is significantly correlated with vorticity of water vapor flux in a few “belt” areas. The strong correlation areas include one that starts in the north of the TP and extends to the downstream of the TP. The two “belt” areas with a strong correlation both merge with those three belts of water vapor transport synchronously in the middle and lower reaches of the Yellow River. The westerly jets in the south and north of the TP and the bypassing flow along the south and north edges of the TP have major contributions to the water vapor and vorticity transport that lead to the heavy rainfall. The results from this study suggest that orographic bypassing mechanisms that account for the heavy rainfall in northern China are beneficial to the transport of the middle-lower latitude eddy energy and water vapor to the middle and lower reaches of the Yellow River. The observational and modeling studies demonstrate that the interannual variations in the thermal forcing of TP are positively correlated with the incidence of wintertime haze over central-eastern China. The TP’s warming and cooling anomalies could lead to a “warm shield” and a “cool shield” in the atmosphere over the CEC. The correlation vector over the CEC indicates that the variations of thermal forcing over the TP could give rise to the weakening winter monsoon winds (southwest wind anomalies) induced by changes in Q1 over the TP. Our results also suggest that implications of the large TP topography to the atmosphere environment and climate variation should be taken into account when extreme torrential precipitation events and air pollution mitigation policies are reviewed in China. (Xu Xiangde, Zhao Yang, Wang Yinjun)

3 Numerical weather prediction and key techniques in numerical modeling

3.1 Research on the configuration of model zones and physical parameters

The monthly mean distributions of upper-level and lower-level circulations, upper-level jets and low-

level water vapor transport flux over the East Asia averaged for the recent 10 years (2005–2014) were analyzed by using the ERA-Interim reanalysis data provided by the ECMWF. The analysis focuses on the distribution characteristics of East Asia major trough, Siberian ridge, subtropical high, South Asia high, upper-level jet and the water vapor transport caused by the southwest monsoon and the southeasterly at the southwest of the subtropical high. The reanalysis model zones including central longitude and latitude, zone size, reference longitude, projection factor and resolution were finally identified by covering as much information as possible on the evolution of these distributions. On this basis, the model parameters including model vertical layers, model top, input of underlying surface, dynamic parameters and physical parameter schemes were determined through debugging. (Wang Donghai, Liang Zhaoming, Yin Jinfang)

3.2 A study of cloud microphysics and precipitation over the Tibetan Plateau with radar observations and cloud-resolving model simulations

With the dual-polarization precipitation radar and cloud radar measurements during the Third Tibetan Plateau Atmospheric Scientific Experiment (TIPEX- III), the cloud microphysics and precipitation by the WRF-CAMS (Chinese Academy of Meteorological Sciences) microphysics were investigated through a typical plateau rainfall event on 22 July 2014. The WRF-CAMS simulation reasonably reproduces the spatial distribution of 24 h accumulated precipitation. The model reflectivity is in general agreement with the in-situ radar observations. The raindrop sizes in the convective region are larger than those in the stratiform region as shown by the small intercept of raindrop size distribution in the former. The sensitivity experiments suggest that warm cloud microphysical processes are important even when the clouds are over a shallow liquid water layer. The simulation excluding ice microphysics produces the most significant increase in both cloud water and rain water (~double) during the weak convective period. Increasing droplet condensation leads to area-averaged rain rate, which is closest to the observation, indicating droplet condensation plays a dominant role in a weak convective process. Reducing raindrop evaporation results in an increase in weak rainfall areas along with a warmer sub-cloud layer. Increasing the initial size of cloud droplets causes the rain rate to be reduced by half, an opposite effect to that of increasing droplet condensation. (Gao Wenhua)

3.3 A numerical study of basin-wide circulation over an idealized basin

The characteristics of circulation over a basin region were examined in idealized simulations. A particular focus was put on the variation of the horizontal closed vortex and the vertical circulation. The flow passing over a basin introduces horizontal closed vortexes and reversed wind in the low-middle levels within the basin. Results exhibit the effects of the basin shape, including the basin depth, width of the basin slope and the basin floor, on the vortex and the reversed wind. In the North Hemisphere, the increasing Coriolis forcing favors the enhancement of a positive closed vortex. The diurnal heating source brings the convergence/divergence into the horizontal field. When the heat is strong enough, the closed vortex is replaced by the convergence during the nighttime. The diurnally varying heating also changes the structure of a vertical circulation, with the presence of an anti-clockwise circulation within the basin at the maximum cooling time (Fig. 8). (Qian Tingting)

气候系统与气候变化 Climate System and Climate Change

气候系统与气候变化研究进展

2015年,气候系统(极地气象)研究所在气候预测理论与方法、气候系统模式研发以及极地气候研究方面获得了显著进展。

1 气候预测理论与方法

1.1 夏季亚洲-太平洋涛动的前期因子及其影响机制

利用观测数据和美国国家环境预报中心(NCEP)的第2版气候预测系统模式(CFSv2)探讨了夏季亚洲-太平洋涛动(APO)的前期因子。结果表明,前期冬、春季热带中东太平洋(TCEP)海表温度异常和春季北印度洋(NIO)海平面气压与夏季APO显著相关。前期冬季TCEP海温异常可以持续到春季,通过“大气桥”效应引起春季NIO海平面气压异常,进而引起青藏高原西部的垂直运动异常,改变了那里的春季降水。青藏高原西部春季降水异常又能通过改变土壤湿度存储异常信号并将其维持至夏季,进而导致该地区表面气温的变化,最终影响了夏季APO。CFSv2模式对前期冬、春季TCEP海温和春季NIO海平面气压的预测具有很高的技巧。同时,它也很好地抓住了前期TCEP海温以及NIO海平面气压与夏季APO的物理联系。因此,该模式可以提前数月预测夏季APO(图1)。(刘舸)

1.2 2014/2015年冬季El Niño事件发展停滞的可能原因

2014年El Niño事件的发展在6—8月发生停滞,这与赤道西太平洋西风事件的减弱消亡有关。而西风事件的减弱消亡又与2014年春季MJO信号减弱相联系。MJO信号减弱后,其引起的赤道西-中太平洋海气耦合过程令赤道西太平洋出现东风异常并得以维持,这时异常海表温度和表面西风的Bjerknes正反馈未建立,表现为 $SOI > 0$,因而未形成不稳定海气耦合波,从而抑制了2014年夏季赤道东太平洋的迅速增暖。这是导致2014年El Niño事件发展停滞的重要因素(图2)。(刘伯奇)

1.3 大西洋海温异常对中国冬季霾日数变化的可能影响

在1978—2012年期间,中国冬季霾日数不仅存在明显的年际变化,还存在显著的上升趋势(2.4 d/10a),上升趋势在1995年后(6.6 d/10a)和2000年后(9.9 d/10a)更加明显。大西洋海温和中国冬季霾日数在年际和年代际尺度上存在显著同位相关关系。前期夏季大西洋年代际涛动(AMO)和中国冬季霾日数的相关系数为0.67(年代际),去趋势后为0.47(年际)。AMO增强对应于北极涛动的正位相,不利于冷空气的活动,导致中国冬季霾日数增多。秋季南大西洋海温指数(SAI)与中国冬季平均霾日数的相关系数为0.64,其通过遥相关波列导致中国东部南风异常,使得冷空气活动减弱,污染物不易扩散,导致霾日数增加。AMO和SAI可以作为预测中国冬季霾日数变化的预测因子,其业务预测应用取得了良好效果(图3)。(肖栋)

1.4 中国冬季极端高温和低温天气气候事件

利用中国台站观测的逐日平均地表温度资料,分析了我国1961—2012年冬季12月至2月每个月的

极端高温和低温天气的变化特征及可能的原因。结果表明，近半个世纪我国冬季极端高温天气事件在增多，而极端低温天气事件在减少。相对前一年12月和当年1月，这种现象在2月更加明显。然而，在12月和1月，持续性的极端低温天气事件在总的极端低温天气事件中的概率在增加，而持续性的极端高温天气事件在总的极端高温天气事件中的概率在减少。相对12月和1月而言，2月更容易发生极端高、低温天气事件，且强度最大。1月极端高、低温事件强度最小，而12月发生极端高、低温天气的概率最小。1月和2月的极端高、低温天气事件与西伯利亚高压和东亚大槽异常有密切关系，且这种密切关系在极端高、低温事件发生前5天已见端倪。除了2月的极端高温天气事件与北大西洋和热带中东太平洋表现出显著的正相关关系和12月极端低温天气事件与印度洋海温表现出显著的负相关关系外，海温与冬季其他极端高、低温天气事件的相关关系都不显著。（左志燕）

2 气候系统模式研发

2.1 模式模拟的东亚层云的误差来源

通过敏感性分析，研究了东亚层云在大气环流模式CAM5中的模拟误差。CAM5对东亚地区层云主要的模拟误差表现为：（1）模式对层云出现频率存在低估；（2）模式在四川盆地模拟出了一个虚假的云量低值中心。对于第1个问题，通过进行2组对比试验，考察环流约束后的模式气候与非约束的模式气候间差异。结果显示，通过约束模式的大尺度环流，使其更为接近真实大气状态，可以提高层云的出现频率。主要原因得益于对环流所引导的大气低层湿环境的刻画更为合理。对于第2个问题，通过考察2组不同模式动力框架的模拟结果，发现这一问题敏感于动力框架的选择。在采用谱框架进行模拟时，这一虚假的云量低值中心不再显著，且模式对该地区短波云辐射强迫的模拟更好。这2组试验所得出的共同结论是，改进模式对大尺度背景环境的刻画可以提高层云的模拟性能。（张祎）

2.2 模式模拟的东亚降水特征的次网格敏感性

通过进行2组采用不同类型次网格模型的大气环流模式，即基于传统参数化方案的CAM5和基于次网格显式2D云模型的超级参数化CAM5，研究了东亚地区降水对次网格过程表征的敏感性。结果显示，在采用超级参数化型模式后，模式对对流主导地区的降水特征改善明显。以华南沿海地区为例，该地区的降水主要以午后峰值主导的局地对流降水为主。传统型模式CAM5在该地区的降水气候特征以高频次的弱降水主导，降水的频次高，但强度低；峰值时间以14:00左右为主，与不稳定能量的日变化相位一致。而超级参数化型模式则减少了弱降水的频次，增加了强降水的频次，使得模式中的降水强度普遍增强；峰值时间出现在16:00左右，滞后不稳定能量的峰值约2 h，与观测更为接近。造成这一差异的原因在于，超级参数化型CAM5对于对流由浅对流向深对流的发展过渡阶段刻画更为真实，使得降水发展的持续过程得到描述，不稳定能量得以累积，降水峰值出现时间晚，但峰值时的降水强度增大。对比传统型参数化模式，对这一过渡转化阶段的描述不佳。模式中的午后对流降水更多是对不稳定能量的一种瞬时的调整响应。因此，模式降雨频繁，但是强度较低，气候态表现为降水不足。（张祎）

2.3 不同分辨率气候模式对东亚地区降水模拟能力的评估

利用美国国家大气研究中心（NCAR）CAM5模式在3种水平分辨率（T42、T106和T266）下分别开展长期积分，从气候态分布、季节变化和小时尺度降水强度结构特征等方面分析了青藏高原及以东地区降水模拟对模式水平分辨率的敏感性。研究发现：随着分辨率的提升，模拟的年平均降水空间分布特征显著改善；低分辨率模式无法再现由复杂地形强迫导致的降水分布，如青藏高原南缘

的狭窄雨带，而随着分辨率提升地形周边降水分布更接近于观测形态；从T42到T266，模拟降水量的大（小）偏差区比例明显减少（增加）。3种分辨率模拟均可再现降水季节变化的主要特征，合理给出东亚季风的演变过程。采用一种新方法对降水强度-频次结构进行评估，发现高分辨率模式给出了更真实的降水强度-频次结构特征，显著抑制了模式中虚假的弱降水，且增大了强降水比重。随着分辨率的提升，陡峭地形区和平原地区区域平均降水强度结构的差异更为显著，与真实情况更为接近。（李建）

3 极地气候

3.1 南极冰盖过去50年气温变化的再评估

针对Steig et al., (2009)和Nicolas et al., (2014)对南极气候变化的评价争论，我们对南极大陆上12个观测站近50年的地表温度观测资料进行了详细的分析。我们依据地理位置、建站海拔高度以及气候特征将这12个观测站分为了内陆、沿海和岛屿3个组。并利用近年来被广泛应用的一种新方法，即去趋势的波动分析方法（DFA），对这12个站的地表温度资料进行了长期记忆性分析。分析发现，不同组的温度资料具有不同的长期记忆性。位于岛屿区的地表温度长期记忆性最强，位于沿海地区的次之，而位于内陆地区的几乎没有长期记忆性。值得注意的是，位于内陆地区西南极的伯德站与东南极的其他各站显著不同，呈现出了较为明显的长期气候记忆性。这些结果表明，地表温度序列是否具有长期气候记忆性，主要取决于其与海洋之间相互作用的强弱。

我们进一步评估了这种长期气候记忆性对计算序列趋势显著性的影响，发现当一个序列具有长期记忆性特征时，受序列自相关性的影响，会增大趋势评估的不确定性。对此，我们提出了一些解决方法，并对这12个站的地表温度变化趋势的显著性进行了分析后发现，当将长期记忆性的影响考虑在内后，12个站中只有3个站呈现出了显著的温度变化趋势。相比于传统的趋势评估方法，本工作所给出的结果更客观、合理。因此，Steig et al., (2009)和Nicolas et al., (2014)对南极气候变化的评价，有明显的误差（图4）。（丁明虎）

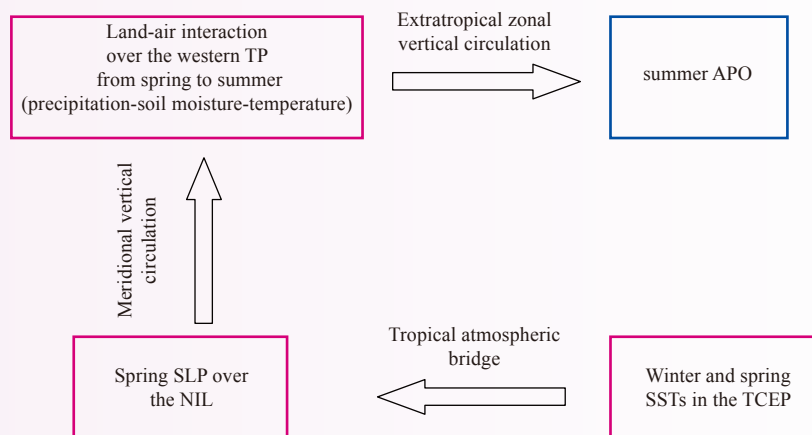


图1 前期热带中东太平洋（TCEP）海温与夏季亚洲-太平洋涛动（APO）的物理链接过程示意

Fig. 1 Schematic diagram summarizing the processes linking the preceding SST in the tropical central-eastern Pacific (TCEP) with summer APO

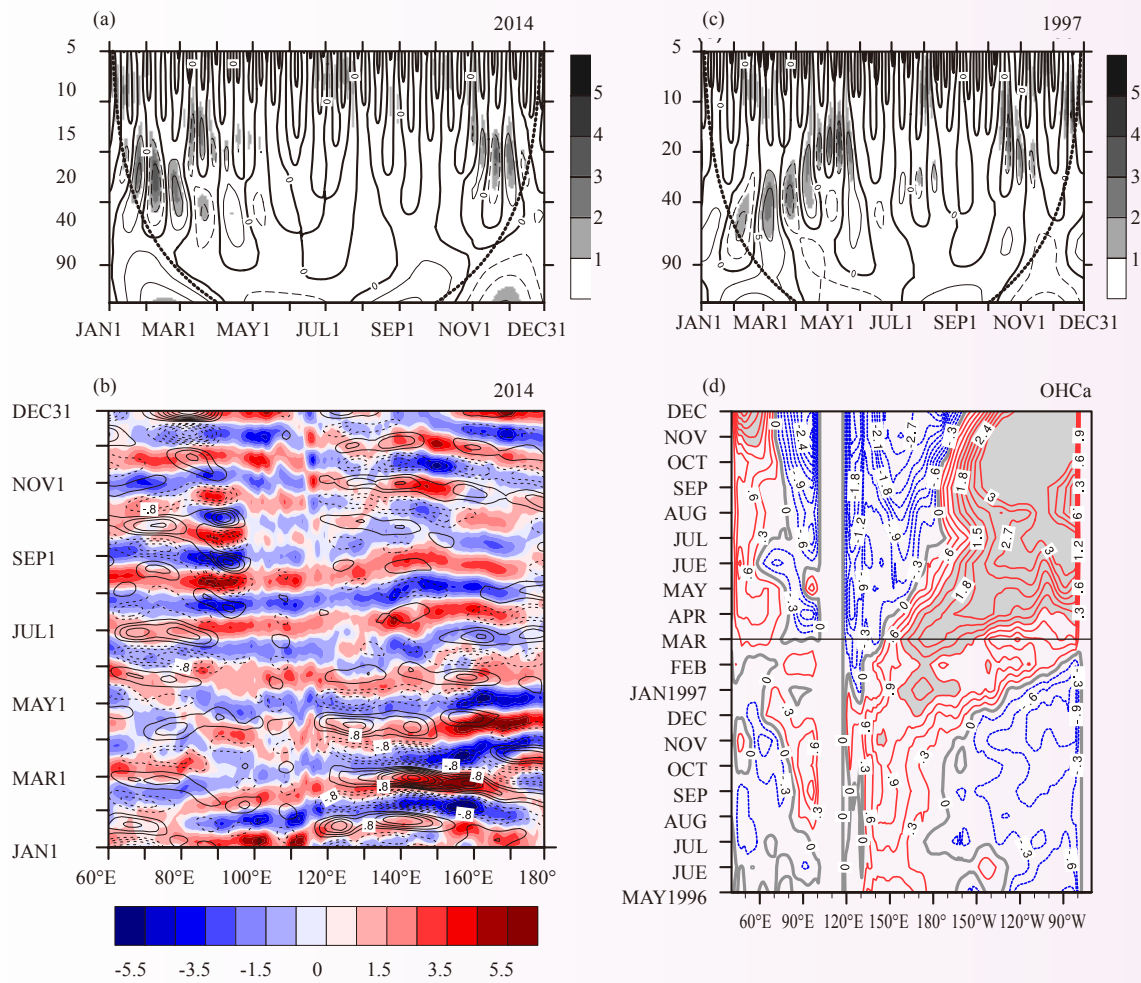


图 2 2014年和1997年赤道西太平洋(3°S~3°N, 120°~150°E)10 m纬向风异常的小波功率谱(阴影表示通过95%置信度水平的周期) (a, c), 2014年30~60天滤波后赤道附近(3°S~3°N平均)GPCP降水异常(阴影, mm/d)和10 m纬向风异常(等值线, m/s)的时间-经度剖面 (b), 1996年5月至1997年12月赤道附近(3°S~3°N平均)上部海洋热含量的时间-经度剖面 (d)

Fig. 2 Wavelet analyses of 10 m zonal wind anomalies over equatorial western Pacific (3°S–3°N, 120°–150°E) in 2014 (a) and 1997 (c), respectively (shadings are for the periods exceeding 95% confidence level); Time-longitudinal crossing section of the 30–60-day filtered anomalies of GPCP rainfall (shading, mm day⁻¹) and 10 m zonal wind (contours, m s⁻¹) near the equator (averaged from 3°S to 3°N) in 2014 (b); The 3°S–3°N averaged time–longitudinal crossing section of upper oceanic heat content from May 1996 to Dec 1997 (d)

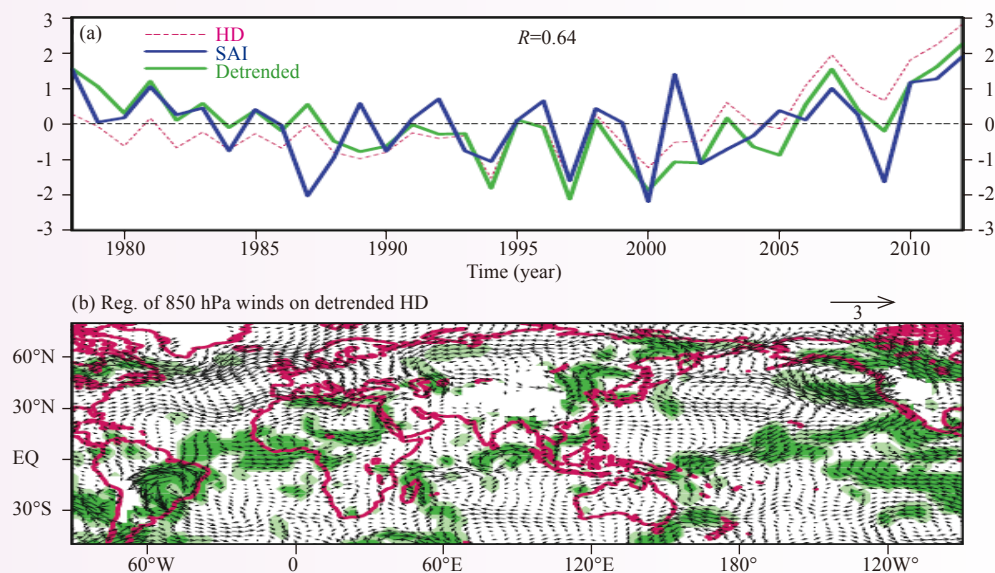


图 3 (a) 标准化霾日数(HD, 红虚线)、去趋势HD(绿色实线)和南大西洋海温指数(SAI)序列(蓝色实线), (b) 去趋势HD回归的850 hPa水平风场(单位: (m/s)/d) (深/浅)绿色覆盖的区域代表通过了95%(90%)置信度水平的检验

Fig. 3 (a) Time series of the normalized HD (dashed red line), detrended HD (solid green line) and SAI (solid blue line) and (b) regression of the horizontal winds in winter at 850 hPa on the detrended HD (unit: $m s^{-1} day^{-1}$). Dark (light) green shadings denote the liner regression coefficients exceeding 95% (90%) confidence level

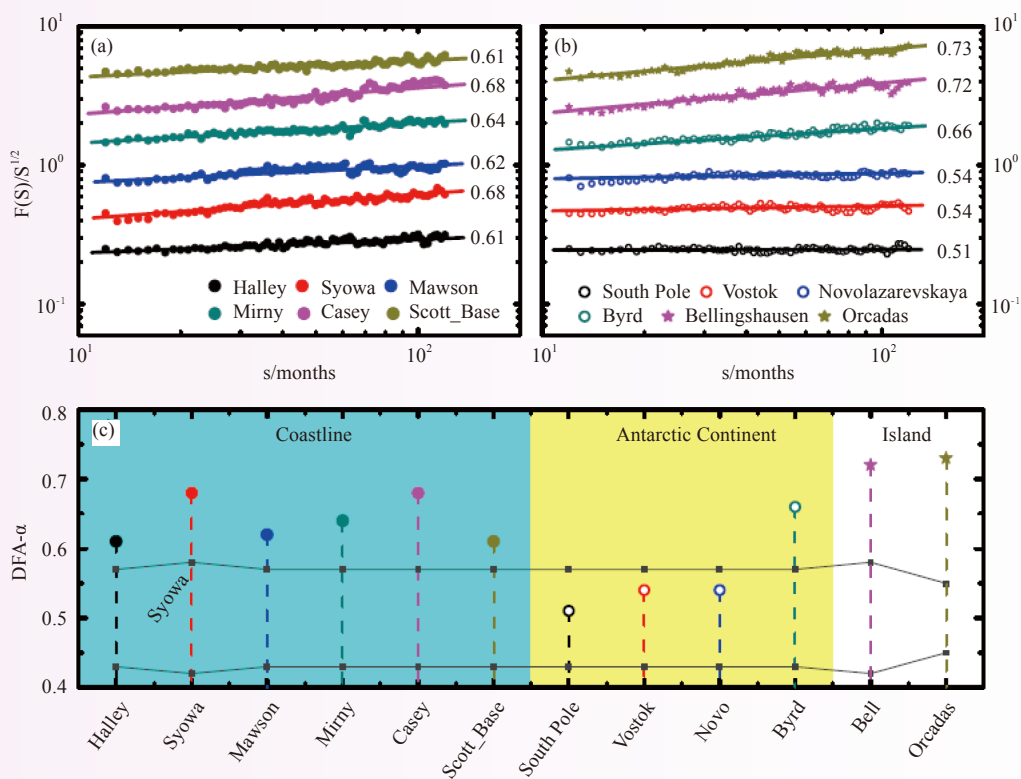


图 4 12个南极气象站地表温度序列的DFA分析结果(a、b)和温度序列中长期记忆性强弱的显著性检验结果(c)
Fig. 4 (a) and (b) DFA-2 results of the 12 monthly records and (c) the corresponding Monte Carlo significance test

Progress in Climate System and Climate Change Research

In 2015, the Institute of Climate System (Polar Meteorology) achieved remarkable improvements in the fields of (1) theory and methodology of climate prediction, (2) development of climate system model, and (3) polar climate.

1 Theory and methodology of climate prediction

1.1 Preceding factors of summer Asian-Pacific Oscillation and the physical mechanism for their potential influences

The authors explored the preceding factors of summertime Asian-Pacific Oscillation (APO) using observations and output from the NCEP Climate Forecast System version 2 (CFSv2). Results show that the winter and spring sea surface temperatures (SSTs) in the tropical central-eastern Pacific (TCEP) and the spring sea level pressure (SLP) over the North Indian Ocean (NIO) are significantly correlated with summer APO. The previous winter TCEP SST anomaly persists until spring and results in SLP anomaly over the NIO in spring through an “atmospheric bridge” effect. The NIO SLP anomaly induces a vertical motion anomaly over the western Tibetan Plateau, which alters spring rainfall in situ. The signal of rainfall anomalies over the western Tibetan Plateau, which resides in underlying soil moisture, maintains itself to the subsequent summer and further modulates local surface air temperature during the following summer and hence the summer APO. The CFSv2 features high skills in predicting the winter and spring TCEP SST and the spring NIO SLP, successfully captures the physic relationships of TCEP SST and NIO SLP with summer APO. Therefore, the CFSv2 is capable of predicting the summer APO teleconnection by several months in advance (Fig. 1). (Liu Ge)

1.2 The possible reason for the suspension of wintertime El Niño event in 2014/2015

The development of 2014 El Niño event was suspended from June to August, which was ascribed to the weakening and diminishing of westerly wind bursts (WWBs) over the tropical western Pacific. It is speculated that the disappearance of WWBs was associated with the damping of MJO in boreal spring 2014. After the attenuating MJO, the induced air-sea coupling process could result in the surface easterly anomalies sustaining over the tropical western Pacific, keeping the Bjerknes positive feedback between warm SSTA and anomalous surface westerly from forming over the tropical Pacific as seen in a negative SOI. Therefore, the unstable air-sea coupling wave was not present to trigger the rapid warming in the tropical eastern Pacific in 2014 summer, leading to the suspension of El Niño development in boreal summer of 2014 (Fig. 2). (Liu Boqi)

1.3 Plausible influence of Atlantic Ocean SST anomalies on winter haze in China

The wintertime haze days (HD) in China showed a significant increase by 2.4 days 10 years⁻¹ during 1978–2012 and an accelerated increase during 1995–2012 (6.6 days 10 years⁻¹) and during 2001–2012 (9.9 days 10 years⁻¹). The Atlantic sea surface temperature exhibits a significant in-phase relationship with haze days at the decadal and interannual time scales. The correlation coefficient between the (detrended) Atlantic multi-decadal oscillation (AMO) and HD over China is (0.47) 0.67. A stronger AMO corresponds to the positive phase of the Arctic oscillation (AO), which implies less cold air activities from North China, being conducive to the occurrence of haze. The Autumn South Atlantic Index (SAI) is related to the HD with a

correlation coefficient of 0.64. A higher SAI results in an abnormal southerly airflow in the troposphere over eastern China through the teleconnection wave chains. Consequently, the weakened cold airflow from north of eastern China, which suppresses the dispersion of pollutants over China, results in above-normal haze days. AMO and SAI, which were employed as the predictors of a haze day over China, performed well in the predication operation (Fig. 3). (Xiao Dong)

1.4 Extreme cold and warm events over China in wintertime

The characteristics of extreme cold and warm events (ECE; EWE) over the whole China in December, January and February were investigated using the observed daily surface air temperature for 1961–2012. Among the three months, both the EWE and ECE in February are most frequent and strongest while least frequent in December and weakest in January. More than 50% of the EWE and ECE in February and less than 40% of the EWE and ECE in January feature persistence (lasting at least 5 days). Generally, the persistent ECE are more frequent than the persistent EWE. The EWE (ECE) in February tend to increase (decrease) in intensity, with a longer (shorter) persistence in 1961–1986 than that in 1987–2012. The persistent feature of the EWE (ECE) in December and January is more (less) obvious in 1961–1986 than that in 1987–2012 although the EWE (ECE) in 1961–1986 is less (more) frequent than that in 1987–2012. (Zuo Zhiyan)

2 Development of climate system model

2.1 Simulations of East Asian stratus clouds: Sources of errors

Via a sensitivity analysis, we studied sources of errors in simulations of East Asian stratus clouds in a general circulation model (CAM5). CAM5 has two major problems: 1) an underestimate of stratus cloud occurrence frequency and 2) a spurious low stratus amount-when-present value center over the Sichuan Basin. The first problem is explored by carrying out two control tests for inter-comparison purpose, in which large-scale circulations in one group are constrained such that they can be closer to the real-state atmosphere, while the other one is not constrained. It is found that the constrained one produces higher occurrence frequency, mainly because of the more realistic low-level moisture environment. For the second problem, an investigation into the results from two different dynamical cores finds that it is sensitive to the choice of dynamical cores. When the spectral core is used, the spurious low-value center disappears, and the model shows more realistic shortwave cloud radiative forcings. A common conclusion drawn from these tests is that simulations of stratus clouds over East Asia are sensitive to the representation of large-scale ambient environment. (Zhang Yi)

2.2 Sensitivity of sub-grid models to simulations of summer precipitation characteristics over East Asia

Two numerical experiments were conducted to study the sensitivity of simulated summer precipitation characteristics to different sub-grid models: (1) CAM5 based on conventional parameterizations and (2) SuperParameterized (SP) CAM5 based on sub-grid 2-dimensional cloud-resolving models. Results show that when using the SP, the model shows more realistic precipitation characteristics over regions that are controlled by convection processes. Take South China as an example, where local late-afternoon convective precipitation dominates over the coastal region. CAM5 produces weak precipitation with high frequency. The peak time, which occurs around 14:00, coincides with that of unstable energy. In contrast, SPCAM5 reduces the frequency of weak precipitation, but increases the frequency of intense precipitation. The peak time occurs around 16:00, later than that of unstable energy. Reasons for these differences are that SPCAM5 more realistically simulates the transition from a shallow to deep convection, during which the evolving process accumulates the unstable energy. The peak time, which occurs later, sees an enhanced precipitation intensity. CAM5, which fails this

transition process, characterizes the afternoon precipitation as responding too quickly to the unstable energy. Thus, CAM5, which rains frequently but weakly, shows less precipitation amount in the sense of climatology. (Zhang Yi)

2.3 Evaluation of a climate model at different horizontal resolutions in simulating precipitation over East Asia

Long-term simulations using version 5.1 of the National Center for Atmospheric Research's Community Atmosphere Model at low (T42), medium (T106), and high (T266) resolutions were carried out to study the impact of horizontal resolution on the model's performance in reproducing the climatological features of precipitation over East Asia. The simulated spatial pattern of annual mean precipitation amount improves significantly with an increased resolution. The low-resolution model is inadequate to reproduce the precipitation closely associated with fine-scale orographic forcing, such as the narrow large-rainfall belt along the southern edge of the Tibetan Plateau. The distribution of rainfall over and around the Tibetan Plateau and high-altitude mountains becomes more realistic at higher resolutions. The proportion of the large-biased (small-biased) areas continuously reduces (increases) when the resolution is changed from T42 to T266. Simulations at all three resolutions can capture the key features of the major seasonal variations of rainfall arising from the onset and advancement of the Asian monsoon. A novel method is used to evaluate the sensitivity of the simulated intensity-frequency structure to the horizontal resolution. The proportion of light rain, which demonstrates a large positive bias in climate models, decreases dramatically at a higher resolution. The intensity-frequency structures averaged over steep-terrain regions and plain areas become more distinctive and realistic as the resolution increases. (Li Jian)

3 Polar Climate

3.1 Analysis on the surface air temperature over Antarctic during the past 50 years

Motivated by the debates between Steig et al., (2009) and Nicolas et al., (2014) on the climate change over Antarctic, we performed a detailed analysis of the surface air temperature over Antarctic observed during the past 50 years. In this study, temperature records of 12 stations in Antarctica island, coastline, and continental areas were analyzed by means of the detrended fluctuation analysis (DFA). After Monte Carlo significance tests, different long-term climate memory (LTM) behaviors are found: temperatures from coastal and island stations are characterized by significant long-term climate memory whereas temperatures over the Antarctic continent behave more like white noise, except for the Byrd station, which is located in the West Antarctica. It is argued that the emergence of LTM may be dominated by the interactions between local weather systems and external slow-varying systems (ocean), and therefore the different LTM behaviors between temperatures over the Byrd station and that over other continental stations can be considered as a reflection of the different climatic environments between the West and East Antarctica.

We further studied the effects of LTM on trend evaluation, and found that if a given time series is characterized by LTM, the uncertainties of the trend evaluation will be enhanced. Therefore, we proposed a new method to better evaluate a trend, with the potential effect of LTM taken into account. For the temperature records at the 12 stations, we found only 3 of them experienced a significant warming trend during the past 50 years. Compared with the traditional trend evaluation method, the new method provides us with more rigorous results. Therefore, the results reported by Steig et al., (2009) and Nicolas et al., (2014) are biased (Fig. 4). (Ding Minghu)

大气探测与雷电防护

Atmospheric Sounding and Lightning Protection

大气探测和雷电研究进展

2015年大气探测与科学试验中心围绕核心任务和优势重点研究方向,基于野外观测试验,将理论和实际应用相结合,在雷达观测技术和雷电活动等方面开展了大量卓有成效的研究工作,取得了丰硕的成果。2015年新申请批准项目8项,包括国家自然科学基金重点项目1项、留学人员科技活动择优资助项目1项、气象行业专项课题1项、中国气象局气象关键集成项目1项、贵州省人工影响天气办公室合作项目1项以及气科院基本科研业务费面上项目3项等;中心的科研成果“雷电临近预警系统的研发和应用”获得2015年气象科学技术进步二等奖;2015年共发表期刊论文34篇,其中SCI(E)收录论文14篇;申请国内发明专利3项、国际发明专利1项、实用新型专利2项;获得软件著作权授权1项;授权专利2项,其中国家发明专利1项、实用新型专利1项。具体成果主要体现在以下几个方面。

1 2015年野外观测试验

2015年,大气探测和科学试验中心在广州组织了广东闪电综合观测试验(GCOELD),在重庆组织了三维(3D)闪电探测试验,在拉萨组织了闪电放电过程观测试验。上述试验均达到了预期目的,获得了丰富的观测资料,推动了闪电探测和分析技术的发展。

1.1 广东闪电综合观测试验(GCOELD)

GCOELD在广州野外雷电试验基地开展,从5月上旬持续到9月上旬,是自2006年以来的第10年外场试验。触发闪电是GCOELD的重要内容,也是开展其他试验的重要手段,2015年共实现触发闪电20次,成功率达到80%,均创历年新高。5月30日成功触发了一次负先导始发的闪电,这是在我国南方首次获得该类型的触发闪电,对闪电放电特征的认识具有重要价值。在该年度的试验中,进一步发展了闪电声、光、电、磁等综合观测手段,完善了多参量并行同步采集技术,提高了数据采集的精度、长度和动态范围,保证了触发闪电和自然闪电放电过程物理参量的高效率和高精度采集。2015年,在持续开展多项雷电防护测试试验的基础上,广州野外雷电试验基地与石化部门合作首次开展了针对DCS仪表系统和UPS电源系统的雷电防护测试,与华为公司合作开展了雷电计数采集器的测试试验,这些合作研究扩展了GCOELD的应用范围和影响力。该年度还扩建了广州高建筑雷电观测站,新观测站大大扩展了室内面积,增强了设备安装和互联能力,显著提高了对广州高建筑物雷电接闪过程的观测水平。此外,作为GCOELD试验的一部分,在广州开展了基于低频电场探测阵列(LFEDA)的闪电观测试验,2015年增加了增城和花都2个子站,使得探测站点数量达到11个。试验获取了大量闪电放电过程的精细观测资料,提高了对广州野外雷电试验基地周边雷暴闪电活动的探测能力(图1~2)。(郑栋,张阳)

1.2 重庆三维(3D)闪电探测试验

2015年重庆三维(3D)闪电探测试验始于3月1日。基于VLF/LF、VHF双频段3D闪电定位网对发生在重庆周边的雷暴闪电活动开展了高精度3D观测试验。根据上一年的站网运行状况,2015年对站点布局做了适当调整并增加了一些外围站点,扩展了站网尺度,扩大了站网的有效探测范围,形成了以

重庆气象局XPZ为中心站，包含14个子站，站网直径达到100 km量级的闪电探测网，探测精度也获得提高。此外，2015年观测试验中对采集软件进行了较大的修改，利用双频段闪电探测仪的独特优势，在软件中引入对VLF和VHF信号进行触发校验的方法，有效抑制了环境噪声可能频繁误触发闪电探测器的的问题（图3）。（郑栋，刘恒毅）

1.3 拉萨闪电放电过程观测试验

拉萨“闪电放电过程观测试验”主要针对“布达拉宫雷电灾害防御基础研究”项目的任务，按照计划实现了布达拉宫附近的雷电放电活动的光信号和电磁信号的高速和连续采集，积累了丰富的观测数据。（郑栋，张阳）

2 高建筑物雷电光学观测试验

2.1 高建筑物雷电连接过程的三维（3D）光学观测和特征分析

对在广州观测到的一次高建筑物雷电（编号F1215）首次回击前的连接过程中先导的三维（3D）发展特征进行了分析。结果表明，在F1215回击前的2 ms内，下行先导的3D发展速率的变化范围为 $(1.3 \sim 6.8) \times 10^5$ m/s（平均值为 2.7×10^5 m/s），对应的二维（2D）速率的变化范围为 $(1.1 \sim 4.9) \times 10^5$ m/s（平均值为 2.1×10^5 m/s）。除了回击前的200 μ s内，下行先导的发展速率随时间无明显的变化趋势。F1215的上行连接先导的3D发展速率变化范围为 $(0.8 \sim 13.7) \times 10^5$ m/s，平均值为 4.5×10^5 m/s。在下行先导的影响下，高建筑物顶部起始的上行先导的发展速率随时间有明显的增加趋势，特别是回击前的1 ms内。下行先导与上行先导3D发展速率的比值随时间逐渐降低，从2.2减小到0.2，说明在回击前上行先导的发展速率会明显超过下行先导的发展速率（图4）。（吕伟涛，马颖）

2.2 一次双极性自然下行地闪的光学特征分析

基于电场变化、高速摄像以及闪电连接过程观测系统的同步观测资料，对观测到的一次双极性自然地闪的先导发展特征及回击光强脉冲波形进行了分析。该次闪电包含正极性首次回击和5次负极性继后回击，所有回击均沿着由首次回击之前的下行正先导开辟的通道进行。首次回击之前的下行正先导发展通道无分叉现象，平均2D发展速度为 2.5×10^6 m/s，在发展过程中其光强出现明显的梯级脉冲变化，在被击中建筑物的顶部观测到了2D长度约为80 m的负极性上行连接先导。各次负极性直窜先导的平均2D发展速度在 $(4.0 \sim 12.4) \times 10^6$ m/s之间；首次回击和各次继后回击的回击速度差别不大，在 $(1.0 \sim 1.3) \times 10^8$ m/s之间，回击光强脉冲的10%~90%上升时间在2.2~3.2 μ s之间，半峰值时间在53.4~81.6 μ s之间。整个闪电过程持续时间约为864 ms，首次正回击和第1次负极性继后回击的间隔时间（大于150 ms）明显大于各次负极性继后回击的间隔时间（13~70 ms），在首次回击和继后回击发生后均存在数次明显的M过程（图5）。（吕伟涛）

3 地基全天空云检测方法

传统的二维（2D）红蓝通道算法广泛应用在全天空云检测方法中，但现有方法对太阳周边区域云检测和天边区域都有较大的误差。通过分析彩色CCD相机的成像原理，提出了一种基于绿色通道的全天空云检测算法。算法首先基于太阳定位算法计算出太阳中心在全天空图像中的坐标，并根据太阳的高辐射特性判断出图像中的太阳是否被云遮挡。再基于彩色全天空图像的绿色通道，通过数学形态学方法模拟出全天空背景亮度，并结合太阳是否被云遮挡的信息对模拟出的背景在太阳区域和天边区域进行亮度调整，通过背景去除就能得到云的初步检测结果，再去掉晴空太阳未被云遮挡时太阳区域的

云检测误差,就能获得高精度的云检测结果。相比传统的2D红蓝通道算法,新的算法仅需利用一维(1D)的绿色通道信息,且在云和天空的过渡区域、太阳区域和天边区域都获得了比传统方法更好的识别效果。(杨俊)

4 初始击穿过程、伴随的闪电放电过程及下部正电荷区

闪电放电的初始击穿过程产生信号在宽带电场中常常表现为双极性脉冲簇的形式。利用在北京和广州观测到的闪电放电电场波形,分析了可探测的双极性脉冲和伴随的闪电放电过程,并进一步探讨了下部正电荷区的作用。此外,检验了一个概念化的放电模型。具体的结果如下:(1)可探测的双极性脉冲在大的纬度范围内一定程度上随着纬度改变,但是在小的纬度范围内其可探测百分比是相似的。(2)类型I、II、III和IV 4种伴随的放电类型被发现。类型I、II和III分别表现为双极性脉冲伴随的反极性云闪、混合闪电以及先导回击。类型IV仅仅为先导回击过程,为探测到双极性脉冲簇。分析认为,这4种放电分别对应大的下部正电荷区、中等下部正电荷区、小的正电荷区以及不可见的正电荷区。(3)类型IV在北京和广州的百分比分别为65.4%和63.3%。其他类型百分比在两地明显不同。在北京类型I和II的百分比更高,可能归因为更大的下部正电荷区。(4)类型I、II和III的脉冲间隔呈增大的趋势。区别于类型III,类型II展现了更长的脉冲回击间隔。对于类型II,在北京双极性脉冲具有更大的脉冲回击幅度比。可以认为,不同类型的放电参数和下部正电荷区直接相关。这些统计分析结果能够用概念的放电模型来解释,该放电模型的合理性也能够一定程度上用该分析结果验证。(张阳)

5 西北太平洋热带气旋闪电活动与气旋强度突变的关系

利用WVLLN全球闪电定位数据、热带气旋(TC)路径和强度数据以及MTSAT-1R卫星提供的TBB云顶亮温数据,以2005—2009年西北太平洋116个热带气旋为研究对象,分析了TC闪电活动与气旋强度变化的关系。结合第0802号超强台风威马逊个例过程,详细研究了不同强度突变过程中不同区域闪电活动的差异及其随时间的演变特征,探讨了利用内核闪电活动对TC强度突变进行指示和预警的可行性。闪电活动易发生在热带低压(10.8~17.1 m/s)和热带风暴(17.2~24.4 m/s)等级阶段,此时观测到有闪电发生的时次最多。随着气旋强度的增强,观测到有闪电发生的时次逐渐减少,这与大西洋研究结论一致。内核闪电密度最大值发生在24 h风速变化为15~25 m/s的增强阶段。气旋所有强度变化过程中(快速增强、一般变化和快速减弱)都有闪电发生。TC内核闪电活动对气旋强度的迅速加强具有一定的指示作用,0~100 km闪电密度在快速增强阶段大于快速减弱阶段,而外雨带区域的闪电密度在不同强度变化过程中的差别较小。因此可以尝试利用内核的闪电活动来预警西北太平洋热带气旋的快速变化。超强台风威马逊(2008)快速增强过程中,内核闪电密度迅速增加。基于卫星观测资料对对流演变特征的分析表明,快速增强过程内核具有最大的云顶高度和最低的云顶亮温,在 $TBB < 200$ K的低亮温区,快速增强累计频次达到100%。内核对流特性在不同强度变化过程中存在的显著差异,一定程度上揭示了闪电活动在快速增强阶段增强的原因(图6)。(张文娟)

6 雷暴中的垂直速度场对起电和电荷分离活动影响的模拟

为了研究垂直运动速度对于起电过程和电荷结构形成的影响,利用三维(3D)起电放电云模式,通过对一个强雷暴单体的模拟,针对垂直速度场中冰相物含量及其携带电荷的分布和演变特征进行了分析。结果显示:(1)在整个雷暴生命史期间,上升速度区($5 \text{ m/s} > \text{垂直气流速度} W \geq 1 \text{ m/s}$)内的冰相物在起电过程中获得的总电荷量最大,霰粒子在该速度区内通过起电获得的总负电荷量峰值可达到

10^{14} nC。(2) 在闪电活动开始之前,冰相物所带的电荷主要来自于上升速度区2 ($W \geq 13$ m/s) 和上升速度区1 (13 m/s $> W \geq 5$ m/s) 内的起电过程。这期间,霰在上述区域内通过起电过程获得的负电荷总量均达到了 10^{13} nC 量级。尽管由于与携带正电荷冰晶混合的缘故,这些区域内表现出的净电荷并不明显,但这些带电冰相物粒子在平流进入其他更有利于重力分离的区域后有利于分层电荷结构的形成,因而对于雷暴初期闪电活动的发生具有重要影响。(3) 准稳定区的垂直速度条件 (1 m/s $> W > -1$ m/s) 最有利于携带异种电荷的冰相物的重力分离,因而明显的净电荷分层往往出现在准稳定区及其相邻区域里。(4) 准稳定区内的冰相物之间也可能发生起电,但主要集中在闪电活动的中期。霰在其中通过起电过程获得的总负电荷量峰值接近 1×10^{14} nC。这源于上升区减弱后,其中的霰粒子进入准稳定区,进而导致与冰晶之间的起电过程。基于这些分析,建立了一个流场中冰相物起电、电荷分离并最终形成电荷分层结构和导致闪电的概念模型,可以解释观测中发现的“闪电洞”现象的行程机制。

垂直速度场对起电和电荷分离过程影响的研究结果补充了雷暴动力条件与闪电活动之间联系的重要一环,指明了准稳定区及其临近区域的垂直速度条件有利于净电荷层的形成,也是闪电激发和传播的主要区域,为未来利用数值模式或更先进的探测设备研究和发展闪电活动预警预报方法提供了参考。(王飞)

7 雷电业务工作和学术交流

7.1 雷电业务工作

进一步完善了全国雷电监测和预警业务平台,对雷电业务相关的业务流程以及软硬件系统和运行环境进行了维护和更新,以保证雷电业务产品数据收集和产品上传的及时有效。雷电监测产品全年、雷电预警产品5月1日至11月1日,每天24 h实时上传到中国气象局网站和中国天气网,及时提供雷电活动服务产品。

雷击森林火灾监测预警服务系统于6月起实时向国家林业局相关部门提供雷电活动服务产品,林业部门通过客户端系统可及时获取相应的预警信息。

完成了2014年全国雷电灾情的数据核查和录入工作,编制《2014年全国雷电灾害汇编》,并完成了《2014年中国气象灾害年鉴》之雷电灾害部分的编制工作,为决策部门的防雷减灾工作提供技术支持。(姚雯,王飞)

7.2 学术交流

于2015年3月分别与成都信息工程大学以及四川省防雷中心开展学术交流活动,在学术交流活动中,科研人员围绕雷电物理、雷电预报预警、雷电防护业务发展等内容做了精彩报告。通过这些交流活动进一步了解了地方业务部门的实际需求,明确了一些当前业务亟需的在科研工作中要解决的问题,从而为接下来的研究工作提出了一些新的思路,扩展了研究的方向。

2015年9月8—9日,在广州从化召开了“2015年雷电科学研讨会暨广东闪电综合观测试验10年总结会议”。来自国内外多所高校、科研业务单位和企业的研究人员参加了此次研讨会。10年来,试验基地建设与发展成绩显著,在人工引雷试验、闪电综合探测、闪电放电过程机理研究、雷电防护试验设计和测试等科研和应用领域取得了丰硕的具有国际影响的成果,逐步形成了以强化气象服务能力、建设气象现代化创新平台为指导方针,以科技支撑和引领雷电防御工作为目标,集试验、业务和科研于一体的雷田野外试验基地。此次10年总结会回顾了广州雷电试验基地建设以来取得成就,加强了在雷电研究方面的学术交流,为未来雷电科学的研究打下了重要基础并对试验基地的发展产生了积极作用。(姚雯)



图 1 2015年GCOELD试验中人工引雷试验场的建设和设备布置情况

Fig. 1 Arrangement of Guangzhou field experiment site for lightning research and testing in 2015



图 2 2015年5月30日17:59:17由负极性先导始发的触发闪电通道特征

Fig. 2 Triggered-lightning initiated with an upward negative leader (20150530/17:59:17)

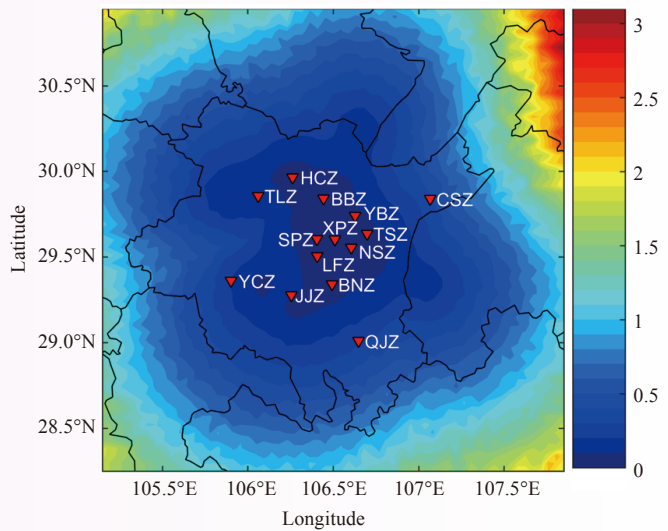
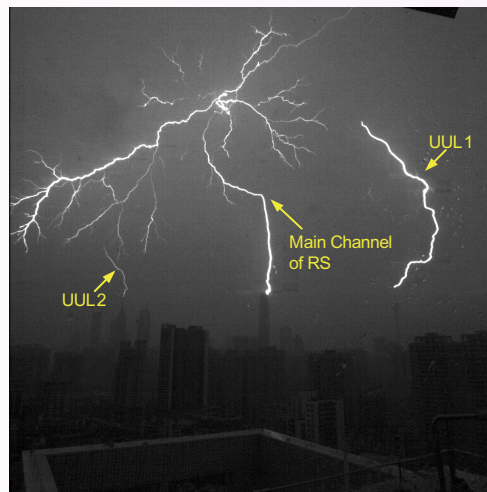
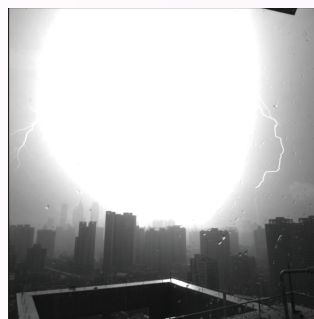


图 3 重庆双频段总闪电探测定位站网布局及其在7 km高度上的定位精度模拟

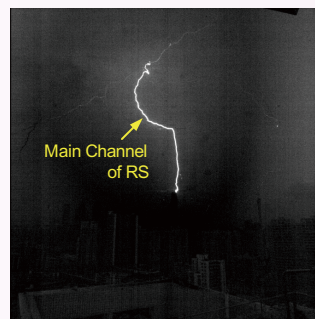
Fig. 3 Arrangement of dual-band total flash lightning location network and its accuracy simulation at the height of 7 km



(a) -0.5 ms



(b) 0.5 ms



(c) 1.5 ms

图4 雷电F1215的高速摄像图片

Fig. 4 The high-speed images of flash F1215

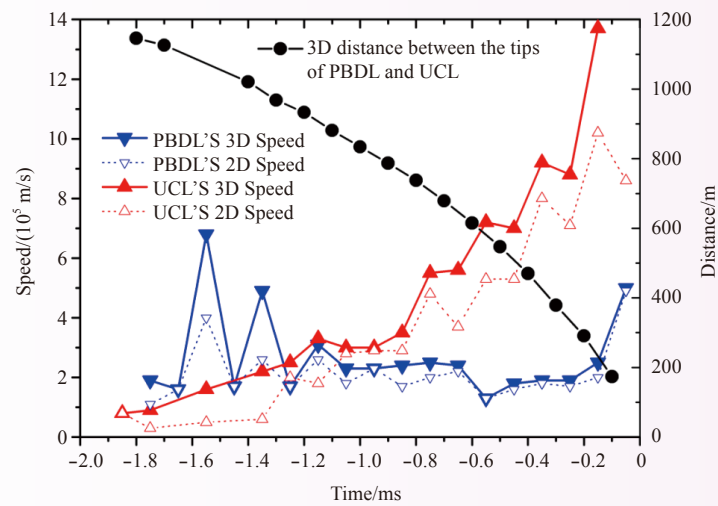


图5 雷电F1215连接过程中下行先导(PBDL)和上行连接先导(UCL)三维(3D)和二维(2D)发展速度随时间的变化

Fig. 5 3D and 2D propagation characteristics of the PBDL and the UCL in F1215 versus time. The solid lines with solid symbols show the 3D characteristics and the dot lines with hollow symbols show the 2D characteristics

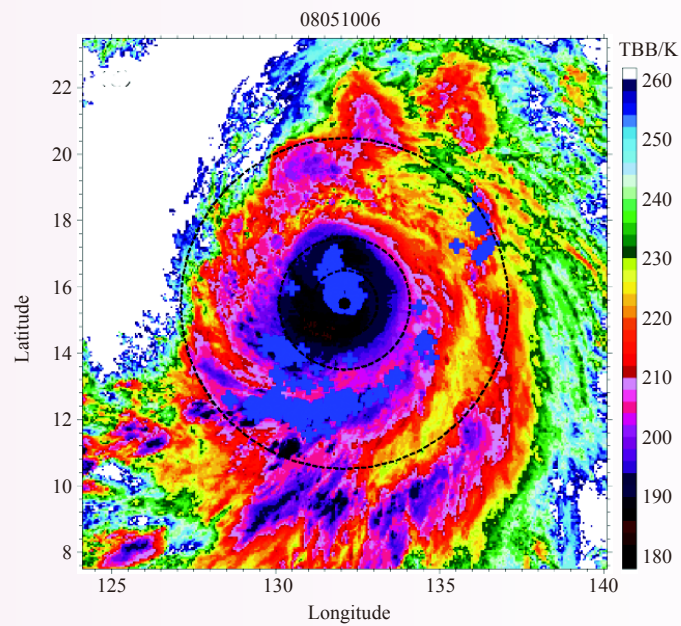


图6 超强台风亚马逊(2008)快速增强阶段的闪电爆发(蓝色十字表示WLLN探测的闪电,3个圆形范围分别为距离台风中心100 km、200 km和500 km)

Fig. 6 Lightning data overlain on minimum TBB for Rammasun (2008) at 06:00 UTC 10 May during RI stages. The blue crosses in each image indicate lightning detected by WLLN. The three rings are at ranges of 100, 200, and 500 km

Progress in Atmospheric Sounding and Lightning Research

Focusing on the central tasks and the key research directions and based on field experiments, the Center of Atmospheric Sounding and Scientific Experiment (CASE) combines theory with practical application and carries out a great deal of productive research work on radar observation and lightning, achieved fruitful results in 2015. Eight new projects were approved, including one key National Natural Science Fund project, one selected Science and Technology Activities for Students Studying Abroad project, one Meteorological Industry project, one CMA-sponsored Key Integration project, one co-sponsored project with the Weather Modification Office in Guizhou, and three Basic Research and Operation oriented projects. The project of “Research on and Application of Lightning Warning and Nowcasting System” won the second prize of 2015 Meteorological Science and Technology Progress; 34 papers were published in 2015 and 14 of them were collected by SCI(E); Three national invention patents, one international invention patent and two practical novelty patents were applied for; One software copyright was authorized; Two patent licenses, one national invention patent and one practical novelty patent, were obtained. The concrete results are shown as follows.

1 Field observations in 2015

In 2015, CASE conducted 3 major experiments: the GCOELD (Guangdong Comprehensive Observation Experiment on Lightning Discharge) in Guangzhou, the Three-dimensional Lightning Detection Experiment in Chongqing and the Observation & Measurement of Lightning Discharge Process in Lhasa. All the experiments were completed well as expected, and abundant observation data were obtained to promote the development of lightning detection and analysis technologies.

1.1 GCOELD-2015

The GCOELD-2015 was conducted from May to September. For artificially triggering lightning experiment is a crucial part of GCOELD, a total of 20 lightning flashes were triggered with a success rate of 80% in 2015. Both the success rate and the total amount of triggered lightning flashes peaked the records since 2006. A positive-polarity lightning initiated with an upward negative leader was first successfully triggered in southern China on May 30, 2015, which is valuable to researches on lightning discharge process. By doing series of experiments in this summer, we further developed the skills in comprehensively detecting the acoustic, optical, electrical and magnetic signals of lightning and improved the technology in parallel synchronization and acquisition. The data quality was raised in sampling length, accuracy and dynamic range, and the high precision and efficiency in acquisition of triggered lightning and natural lightning data were reachable. In 2015, apart from doing some regular lightning protection tests, we also cooperated with SINOPEC to do some specified tests on lightning protection of DCS instrumentation system and UPS power supply system. As an important partner, Huawei technologies tested their flash counters with our help during the experiment. All these partnerships helped expand GCOELD’s application range and presence. At the same year, tall-object observatory in Guangzhou has been rebuilt. The new observatory has a larger internal area with a better environment for instruments’ installation and interconnection compared to the former one. All these reconstruction works helped improve the ability of observing lightning connection process on a tall-object. In addition, as a part of GCOELD, we conducted the lightning activity observation based on the Low-Frequency E-field Detection Array (LFEDA). In order to get more detailed data on lightning discharge sub-processes, two

extra sub-stations were built in Zengchen and Huadu, which will increase the capability to detect thunderstorm activities near the experiment field (Fig.1–2). (Zheng Dong, Zhang Yang)

1.2 3D lightning detection experiment in Chongqing

Three-dimensional Lightning Detection Experiment was conducted in Chongqing since March 2015. The aim of the experiment was to detect and record lightning activities by using VLF/LF and VHF lightning detection network. Based on the network running condition in last year, the locations of some stations were adjusted and a few extra stations were built. Therefore, not only the scale and the detection range of the whole network were expanded, but also its detection accuracy increased. As a result, the lightning detection network (with a center station in Chongqing and 14 sub-stations nearby) reached a diameter of hundreds kilometers. Furthermore, great modifications were made to the acquisition software in this year. Based on the advantages of dual-band lightning detection instrument, trigger check on VLF and VHF signals was added to the software, which effectively reduced the possibility of spurious triggering by environment noise (Fig. 3). (Zheng Dong, Liu Hengyi)

1.3 Observation & measurement of lightning discharge process in Lhasa

The objective of the observation & measurement of lightning discharge process in Lhasa was to meet the task requirement of Lightning Protection Research of the Potala Palace. According to the project plan, we continuously acquired the optical and electromagnetic signals of lightning discharge activities around the Potala Palace with a relatively high speed, which helped to accumulate abundant observation data. (Zheng dong, Zhang Yang)

2 Optical observations in a tall-object

2.1 Three-dimensional optical observation and analysis of the attachment process in tall-object lightning flash

The three-dimensional (3D) propagation characteristics of the leaders during the attachment process prior to the first return stroke of a tall-object lightning flash (numbered F1215) captured in Guangzhou were analyzed. The results show that: The 3D propagation speed of the primary branch of the downward leader (PBDL) of F1215 ranges from 1.3×10^5 to 6.8×10^5 m s⁻¹ (average: 2.7×10^5 m s⁻¹) during the final 2 ms prior to the RS, and the corresponding 2D speed ranges from 1.1×10^5 to 4.9×10^5 m s⁻¹ (average: 2.1×10^5 m s⁻¹). The speed of the PBDL shows no clear changing trend, except for the final 200 μs. The 3D propagation speed of the upward connecting leader (UCL) in F1215 ranges from 0.8×10^5 to 13.7×10^5 m s⁻¹ with an average value of 4.5×10^5 m s⁻¹. The upward leaders, upward connecting leader or unconnected upward leader (initiated from the tall-objects under the influence of the downward leader) tend to increase in speed as the time approaches the return stroke and to increase their speeds sharply during approximately the final 1 ms. The 3D speed ratio between the PBDL and the UCL tends to decrease with time and ranges from approximately 2.2 to 0.2, which means that the upward leader can exhibit a speed significantly exceeding that of the PBDL (Fig. 4). (Lü Weitao, Ma Ying)

2.2 Analysis of the optical characteristics of a natural downward bipolar lightning flash

Using the observation data of the fast and slow electrical antennae, high-speed cameras, and the Lightning Attachment Process Observation Systems (LAPOSs), the optical progression characteristics of the leaders and the optical pulse waveform of the return strokes in a downward bipolar lightning flash were analyzed. This

flash contains one first positive stroke and five subsequent negative strokes. All the six strokes propagated along the same channel established by the first positive return stroke. The leader which preceded the positive return stroke propagated downward without any branches at a two-dimensional (2D) speed of $2.5 \times 10^6 \text{ m s}^{-1}$. An upward connecting leader with a length of about 80 m was observed in response to the downward positive leader. The 10%–90% rise times of the return strokes' optical pulses ranged from 2.2 to 3.2 μs , while the widths from the 10% wave front to the 50% wave tail ranged from 56.5 μs to 83.1 μs , and the half peak widths ranged from 53.4 μs to 81.6 μs . All the return strokes exhibited similar speeds, ranging from 1.0×10^8 to $1.3 \times 10^8 \text{ m s}^{-1}$. Each of the return strokes was followed by a continuing current (CC) stage. The first positive stroke CC lasted more than 150 ms, much longer than all the subsequent negative stroke CC, ranging from 13 ms to 70 ms (Fig. 5). (Lü Weitao)

3 The ground-based whole sky cloud detection method

Traditional two-dimensional red-to-blue band methods have been widely used for cloud detection in total sky images. The brightness distribution in a total sky image is usually non-uniform, because of forward scattering and Mie scattering of aerosols, which results in increased detection errors in the circumsolar and near-horizon regions. By analyzing the imaging principle of cameras, green channel has been selected to replace the 2D red-to-blue band for detecting cloud pixels from partly cloudy total sky images. The proposed algorithm is composed of three main sub-processes: determining whether the sun is obscured by clouds and providing a solar mask, detecting clouds based on a background subtraction adaptive threshold method, and removing the impact of direct sunlight. The first sub-process calculates the circularity of the saturated pixels in the circumsolar region to determine whether the sun is obscured by clouds to create the solar mask. The cloud detection process consists of a morphology opening operation, the adjustment of background information dependent on sun-shadowing, and background subtraction, using AT methods to define the cloud mask. In the third sub-process, the final cloud detection result will be obtained by subtracting the solar mask from the cloud mask. Compared with the 2D red-to-blue band methods, the proposed algorithm used only 1D green channel and obtained better cloud detection results especially in the circumsolar and near-horizon regions. (Yang Jun)

4 Preliminary breakdown, following lightning discharge processes and lower positive charge region

Bipolar pulse trains in wideband electric field records are often attributed to preliminary breakdown (PB) processes. Using electric field waveforms of lightning discharges observed in Beijing and Guangzhou, the detectable PB pulses and the following discharges were analyzed, and the role of lower positive charge region (LPCR) was investigated. Furthermore, a conceptual discharge model was tested. The detailed results are as follows. (1) The percentages of detectable PB pulses are just a function of latitudes and ranges to a certain extent. But the percentages are similar in a small range of latitude. (2) Four discharge types have been identified. Type I, type II, and type III exhibit PB pulses featuring inverted intracloud (IC) discharge, hybrid flash (an IC discharge featuring a negative return stroke (RS)), and leader-RS, respectively. Type IV only exhibits a leader-RS waveform without detectable PB pulses. It is believed that the charge structures of four discharges are characterized with large LPCR, modest LPCR, small LPCR and invisible LPCR, respectively. (3) The discharges of type IV are about 65.4% and 63.3% in Beijing and Guangzhou. And the percentages of other discharge types are obviously different. There are higher percentages for type I and type II in Beijing, which may be attributed to larger scale of LPCR. (4) The values of pulse interval (T_{pi}) rank in increasing

order for type I, type II and type III. Compared with type III, type II exhibits longer pulse-return stroke interval (T_{p-ri}). As for type II, obviously larger amplitude ratio between the maximum peak of PB pulse train and the peak of the first RS (R_{p-rr}) is found in Beijing. It is speculated that the parameters of different discharge types are related to the scale of LPCR. The analysis results are interpreted by a conceptual discharge model and the rationality of the model is also verified by the results to a certain extent. (Zhang Yang)

5 Relationship between lightning activity and tropical cyclone intensity over the Northwest Pacific

Lightning data from the World Wide Lightning Location Network along with tropical cyclone (TC) track and intensity data from the China Meteorological Administration and TBB data from the MTSAT-1R satellite were used to study lightning activity in 116 TCs over the Northwest Pacific from 2005 to 2009, and to investigate the relationship between inner core lightning and TC intensity changes. Super Typhoon Rammasun (2008) was studied to investigate lightning patterns in the Pacific Basin and the implications of using inner core lightning to examine rapid changes in TC intensity. Lightning in TCs over the Northwest Pacific is more likely to occur at tropical depression ($10.8\text{--}17.1\text{ m s}^{-1}$) and tropical storm ($17.2\text{--}24.4\text{ m s}^{-1}$) intensity levels, which is in agreement with past studies of Atlantic hurricanes. The individual time periods with lightning decreased with the enhancement of TC intensity. The greatest lightning density (LD) in the inner core appears in storms undergoing an intensity change of $15\text{--}25\text{ m s}^{-1}$ during the next 24 h. Lightning is observed in all storm intensity change categories: rapid intensification (RI), average intensity change (AIC), and rapid weakening (RW). The differences in LD between RI and RW are largest in the inner core, and the LD for RI cases is larger than for RW cases in the inner core (0–100 km). Lightning activity there, rather than in the outer rainbands, may be a better indicator for RI prediction of Northwest Pacific storms. There was a marked increase in the lightning density of inner core during the RI stage for Super Typhoon Rammasun (2008). Satellite data for this storm show that the RI stage experienced the highest cloud-top height and coldest cloud-top temperatures, with all the minimum black body temperature values being below 200 K in the inner core. The significant differences in the characteristics of convection process within RW, RI and AIC in the inner core, to some extent, revealed the reasons that lightning activity enhanced during the RI stages (Fig. 6). (Zhang Wenjuan)

6 Impact of a vertical velocity field on charging processes and charge separation in a simulated thunderstorm

An isolated thunderstorm was simulated using a 3D cloud model coupled with charging and discharging processes. An analysis of the spatial and temporal characteristics of the content of ice particles and the charges on ice particles in different vertical velocity ranges indicates that: (1) Ice particles obtained the most charges from the charging processes in the updraft region. The maximum magnitude of negative charges on graupel in the updraft region could reach 10^{14} nC . (2) Before the start of lightning activity, charges on ice particles were generated in the charging processes in updraft region 2 and updraft region 1. During this period, the total negative charges on graupel in these two regions all reached a magnitude of 10^{13} nC . Because of the sufficient mix between ice crystals charged with positive charges and graupel with negative, a net charge in these two regions was not evident. After the charged ice particles were transferred into the outer regions, being beneficial for charge separation, a layered charge structure quickly formed. Therefore, the charging processes in updraft region 2 and updraft region 1 were important to the first lightning activity. (3) Charging processes between ice particles in the quasi-steady region also occurred, but primarily during the middle stage of lightning activity.

The peak of negative charges on graupel in the quasi-steady region was close to 1×10^{14} nC. With a decreasing updraft, updraft regions were weakened into a quasi-steady region. Much graupel in the updraft regions was transferred into the quasi-steady region, intensifying the charging processes there. (4) Through a comparison of the contributions of charging processes, the vertical velocity in the quasi-steady region was more conducive to the separation of charges with different polarity, causing the most significantly net charges in the quasi-steady region. The peaks of net positive charges and net negative charges in the quasi-steady region all exceeded or neared 1000 nC, which was much larger than the peaks in other vertical velocity ranges.

Our study represents an important contribution toward an advanced understanding of the relationship between lightning activity and the dynamics of thunderstorms. The results indicate that the vertical velocity in a storm's quasi-steady and adjacent region is beneficial to the formation of a net charge structure, and thus these regions should be mainly where lightning initiates and propagates. Our findings provide a reference for the development of lightning warning or forecasting methods using numerical models and advanced detection equipment. (Wang Fei)

7 Operation of lightning warning and related academic exchanges

7.1 Operation of lightning warning

The lightning monitoring and warning platform was improved to maintain and upgrade the processes, software and hardware of the lightning operation and its running environment so that the data collection of lightning operation products and their uploading are timely and effective. The products are uploaded to the website of CMA and the Weather China in real time, with the monitoring products on an annual basis and the warning products from 1 May to 1 November.

The lightning forest fire monitoring and warning service system started to work from this June. It supplied the relevant departments of the state forestry administration with the lightning activity service products in real time. The warning information could also be obtained from the client of the system.

The verification and recording of lightning disaster data in 2014 were completed. National Lightning Disaster Assembly in 2014 and the lightning disaster section of Chinese Meteorological Disaster Yearbook in 2014 were compiled. The data provided technical support to the decision-making on lightning protection and disaster mitigation. (Yao Wen, Wang Fei)

7.2 Academic exchanges

Two academic exchanges were carried out with the Chengdu University of Information Technology and the Sichuan Lightning Protection Center respectively during March 2015. The researchers made presentations on lightning physics, lightning warning and development of lightning protection service. Through the communications, the actual demands of local operators were learned of and some urgent operation problems that are needed to be solved in research were defined. The exchanges gave us new ideas on the next research work and expanded our research field.

“Decade review meeting of GCOELD” was held in Conghua, Guangzhou, on 8–9 September, 2015. The participants came from universities at home and abroad, scientific institutions, operators, and enterprises. In the past 10 years, GCOELD achieved good progress and development. Fruitful achievements with international influence were obtained. The meeting reviewed the achievements of GCOELD in the last decade, gave a chance to strengthen the academic exchange in lightning research, laid an important foundation for the future study of lightning science, and had a positive effect on the development of GCOELD in the future. (Yao Wen)

大气物理与人工影响天气

Atmospheric Physics and Weather Modification

云物理与人工影响天气研究进展

1 云物理观测研究

1.1 海洋层积云微物理特征的观测研究

利用海洋层积云观测试验数据库中的气象、云粒子和垂直湍流观测资料,分析了海洋层积云穿云过程中云参数的特征及微物理过程。将穿云过程按照降水强度分为晴空、轻度毛毛雨和重度毛毛雨3个类型。结果表明,非降水穿云过程、轻度毛毛雨、重度毛毛雨的云滴数浓度平均值分别为256、247和193;液态含水量分别为0.06、0.15和0.30;滴谱的标准差分别为1.20、1.42和1.98;相对散度分别为0.40、0.34和0.32。对夹卷混合过程的分析表明,海洋层积云中极端非均匀夹卷混合过程占主导,但非均匀夹卷混合并随后抬升过程也占相当比重。分析了非降水、小毛毛雨和大毛毛雨穿云过程的垂直速度标准差与云参数的关系,结果表明在海洋层积云中小毛毛雨时垂直速度的扰动与云参数的关系更加紧密。(段婧)

1.2 华北积层混合云中冰晶形态和增长过程的飞机观测研究

利用北京3架飞机联合云探测试验数据,进一步研究了2009年4月18日和5月1日2次积层混合云中冰晶形态和增长过程。结果表明,飞机在 $0 \sim -16$ °C范围的云层内观测的冰晶形态主要为板状、针柱状、柱帽状、辐枝状和不规则状。在所有研究的云中可识别出多种云形态的混合,但是嵌入对流区有更多凇附程度高的枝状冰晶,层云区含有更多板状冰晶。凇附和聚并过程在粒子拓宽过程中均具有重要作用,而且这些过程在嵌入对流区比层云区更为活跃。4月18日个例中,尽管聚并过程明显,但凇附过程更为显著,而5月1日个例中聚并过程更为显著。随着云中高度的降低,嵌入对流区和层云区均存在粒子谱拓宽的情况,但在4.8 km (-11.6 °C)和4.2 km (-8 °C)层之间的粒子谱拓宽率高于4.2 km (-8 °C)和3.6 km (-5 °C)层之间的粒子拓宽率。另外,由于嵌入对流区具有更为活跃的并合和凇附过程,其粒子谱拓宽速率大于层云区的拓宽率。嵌入对流区中存在的高过冷液态水含量对于促进凇附和并合过程起到关键作用。(朱士超,郭学良,卢广献,等)

1.3 2011—2013年中国冻雨、冻毛毛雨和冻雾的特征分析

研究冰冻天气的特征对于更好地认识冰冻天气,提高此类天气的预警预报能力,从而达到防灾减灾有重要意义。利用2011—2013年间中国民航机场的1 h或0.5 h一次的例行观测和特殊观测资料,分析了冻雨、冻毛毛雨和冻雾天气的时空分布、持续时间和气象条件等特征。研究表明,我国大部分地区均会发生冰冻天气。冻雨和冻毛毛雨的频发区与其持续时间较长区比较一致,而冻雾的少发区,其持续时间也可能较长。我国冰冻天气最容易在冬季(12月至次年2月)发生,在1月出现的比例最高;在凌晨(00:00—07:00)出现频率相对较高,午后(13:00—14:00)出现频率最低。一次冰冻天气的持续时间一般不超过2 h。温度在 $-3 \sim -1$ °C,露点温度在 $-4 \sim -1$ °C,温度露点差在 $0 \sim 1$ °C时冰冻天气发生的频率最大。出现冰冻天气时的风向以东北风和北风为主,而平均风速在 $2.0 \sim 3.9$ m/s时冻雨和冻毛毛雨发生的频率最大。我国冻雨和冻毛毛雨发生时,同时常会有雾或轻雾;冻雾出现时,一

般不会伴随其他天气。(李杰, 郭学良, 周晓宁, 等)

1.4 三维(3D)云场分布诊断方法的研究

统计了2007—2008年Cloudsat云检测产品与ECMWF再分析资料的相对湿度, 得出我国云内外相对湿度判别阈值及其随高度变化, 提出了基于再分析资料的三维(3D)云场分布诊断方法, 应用于实例3D云场诊断, 并与卫星、雷达和地面云降水观测等资料进行了对比分析。得到的主要结论有: Cloudsat云检测mask值大于20的云区位置与Cloudsat给出的ECMWF再分析资料辅助产品的相对湿度高值区有很好的时空对应; 统计分析云内和晴空相对湿度频率分布发现, 不同高度范围的云内相对湿度都呈单峰型分布, 峰值在相对湿度100%附近, 晴空相对湿度受当地大气环境影响, 各地各高度都有差别; 通过相对湿度对云区和晴空的TS评分测试, 得出了诊断云区的相对湿度阈值及其垂直分布; 利用NCEP再分析资料对中国3D云场的分布进行个例诊断应用, 与卫星、雷达和地面云降水观测的对比发现, 云区附近的湿度梯度大, 相对湿度阈值法诊断的云区总体比较稳定; 诊断的云区与上升气流区对应较好, 云区和晴空的分布与卫星Tbb观测大致对应, 云厚即云格点总数与光学厚度和地面降水的分布比较一致; 云场垂直剖面可以清晰地看出其分布同天气系统的关系, 诊断的云区与地面云观测比较一致, 云层密实深厚的区域通常对应着地面降水; 单点的云垂直结构随时间演变与当地的雷达和地面云降水观测都比较一致。总之, 基于再分析资料通过相对湿度阈值法诊断的3D云场及分布, 与云降水和天气系统的发展移动有很好的吻合, 在天气、气候和人工影响天气等方面都有很好的应用前景。(蔡森, 周毓荃, 欧建军, 等)

1.5 北京“7·21”特大暴雨云降水结构及云雨转化特征分析

利用多普勒雷达资料、FY-2E静止卫星和MODIS极轨卫星反演产品, 研究2012年7月21日北京特大暴雨的云降水结构及云雨转化特征。结果表明, 降水过程3阶段的云降水垂直结构不同。(1)在暖区对流降水阶段, 降水以暖雨机制启动, 雨滴在暖区存在深厚的碰并增长过程, 暖雨过程对降水起主要贡献。随着云体的发展, 冷雨过程加剧。T-Re分析表明, $-10\text{ }^{\circ}\text{C}$ 层以下云滴凝结碰并显著, $-10\text{ }^{\circ}\text{C}$ 层以上为深厚的冰相增长带, 云顶以冰相大粒子为主, 云水向雨水转化迅速。(2)在锋面对流降水阶段, 降水系统为高度组织化的“低质心”强降水液态中尺度对流(MCC)系统。回波强度在冰水混合层增长较快, 冻结层是此阶段成雨微物理的关键层。降水粒子在暖云区碰并增长较快, 而蒸发或破碎过程并不显著。(3)在锋后降水阶段, $0\text{ }^{\circ}\text{C}$ 层附近冰晶粒子与云水的碰并增长较为明显。前期降水存在明显的雨滴蒸发过程。随着云体的发展, 暖区云水含量较少, 降水粒子不能有效碰并增长。(周毓荃, 蒋元华, 蔡森)

1.6 1979—2012年夏季黄土高原空中云水资源时空分布

利用欧洲数值预报中心(ECMWF)发布的新一代全球分辨率ERA-Interim再分析数据, 采用经验正交函数 EOF)、小波分析、回归分析等方法, 分析了1979—2012年夏季黄土高原空中云水资源时空分布。结果表明:(1)夏季黄土高原空中云水资源远大于该地区实际年降水量, 具有较大空中云水资源开发利用潜势。(2)空间上云水资源表现为2种模态——西北部、东南部反位相振荡(EOF1)以及中部云水资源偏多西北、东南两端偏少(EOF2), 且具有显著年际变化周期。(3)黄土高原的空中云水资源主要来自东海, 当水汽输送反气旋环流中心偏南(北)时, 影响EOF1(EOF2)空间模态。(4)云水、云冰量峰值分别出现在700 hPa、400 hPa左右, 当700 hPa存在水汽辐合及上升运动时有利于黄土高原空中云水资源开发。(潘留杰, 张宏芳, 周毓荃, 等)

1.7 四川盆地夏季云下气溶胶分布特征飞机观测分析

2009年6月23日利用夏延飞机搭载的云粒子测量系统(PMS)对四川盆地上空的云和气溶胶进行

了2次观测试验。本文利用PMS的PCASP-100X气溶胶探头一天之内连续2架次云下观测数据和“云与地球辐射能量系统(CERES)”的云和辐射资料(CERES SYN1deg-3Hour Ed3A)数据,结合HYSPLIT模式模拟的气团后向轨迹和前向轨迹,分析了四川盆地2次观测的气溶胶粒子数浓度垂直分布、粒子谱分布和来源特征。结果表明,四川盆地城镇的大气气溶胶粒子主要来源于地面向上输送,远距离输送对四川盆地气溶胶粒子的贡献不大,主要是受四川盆地区域内或局地的污染物影响,气溶胶粒子生成后也主要在四川盆地区域内集聚。云和降水、季节、光照、气温、逆温、地表加热等影响着边界层结构,而边界层结构显著影响着气溶胶粒子的垂直分布,夏季白天发展深厚的混合层内气溶胶粒子的垂直混合很强,混合层以上气溶胶粒子浓度迅速递减。观测到的大气气溶胶数浓度量级在 $10^8 \sim 10^9 \text{ m}^{-3}$ 之间,与河北省的大中小城市、北京及周边地区的大气气溶胶浓度量级相同。观测到的云下气溶胶粒子较多的是小粒子,气溶胶粒子浓度随尺度的增大迅速减小。气溶胶粒子的Angstrom波长指数介于1.2~1.4之间,在城市工业气溶胶的特征明显。(王维佳,郭学良,李宏宇,等)

1.8 X波段双偏振雷达对不同坡度地形云探测个例分析

利用X波段双偏振多普勒雷达观测的祁连地区地形云个例资料,对比分析了 3° 、 9° 和 14° 坡度与不同影响气流下形成的地形云特征。结果表明,夏季祁连地区在不同影响气流和不同坡度条件下形成的地形云差异显著,沿坡生成的单体数量、强度及内部动力、微物理过程和优势粒子分布特征均有明显差异,深入研究不同条件下的地形云将有助于科学开展地形云人工增雨作业。(马学谦,陈跃,张国庆,等)

2 云降水物理与人工影响天气数值模拟研究

2.1 北京一次积层混合云系结构和水分收支的数值模拟分析

利用中国气象科学研究院(CAMS)中尺度云分辨模式对2007年10月的一次积层混合云降水过程进行了数值模拟。利用模拟结果结合实测资料,研究了积层混合云系的宏微观结构和降水特征,并分析了云系的水分收支及降水效率。结果表明,积层混合云是导致此次北京降水的主要云型,积层混合云降水分布不均匀,云系中微物理量的水平和垂直分布都不均匀,具有混合相云的云物理结构。冷云降水过程占主导地位,雪的融化对雨水的形成贡献最大。北京区域降水过程的主要水汽源地为黄海海面及蒙古国,2支气流在陕西北部汇合后的西南气流将水汽输送到华北地区,北京区域以外,水汽和水凝物主要从西边界和南边界输送到域内。北京区域降水主要时段内,水物质通量在水平方向上为净流入。对北京区域水汽、水凝物和总水物质的水分收支各项的估算表明,水物质基本达到平衡。北京区域从2007年10月5日20:00至6日14:00,总水成物降水效率、凝结率、凝华率及总水凝物降水效率分别为5.6%、4.77%、4.19%、44.9%。(陶玥,李军霞,党娟,等)

2.2 华北一次积层混合云微物理和降水特征的数值模拟与飞机观测对比研究

为考察云数值模式中的云物理方案和对实例云物理和降水过程的模拟能力,将中尺度数值模式(WRF)模拟的华北地区一次积层混合云的微物理结构特征、降水过程与国家科技支撑计划重点项目环北京地区3架飞机联合云探测试验数据以及雷达、地面降水观测数据进行了深入比较和验证研究。结果表明,WRF模式能够较好地模拟出此次积层混合云的云系演变、雷达回波和降水分布特征。对比结果是:(1)模式模拟的云中液态水浓度(LWC)与飞机观测值具有较好的一致性,在 3°C 层,飞机观测的LWC最大值为 0.8 g/m^3 ,模拟的飞机路径上的LWC最大值为 0.78 g/m^3 ,两者接近;在 -8°C 层,飞机观测LWC最大值为 1.5 g/m^3 ,模拟的飞机路径上的LWC最大值为 1.1 g/m^3 ,模拟值偏小;在 -5°C 层以下,模式能够准确模拟云中水凝物的垂直分布,包括融化层的分布,模拟的水凝物质量浓度与实

测吻合。而对固态水，在 $-6 \sim -10\text{ }^{\circ}\text{C}$ ，由于模式中雪粒子淞附增长过程较大，聚合过程发生的高度偏高，导致模式模拟的固态水凝物质量浓度高于实测值，说明模式在雪粒子增长过程的处理方面有待进一步改进。(2) 在云粒子谱参数方面，在 $-8\text{ }^{\circ}\text{C}$ 层，由于模拟的雪粒子质量浓度偏高，所以模式计算的粒子谱的截距和斜率都小于飞机观测值，模拟偏小；在 $-5\text{ }^{\circ}\text{C}$ 层，两者比较接近；在 $3\text{ }^{\circ}\text{C}$ 层，由于云中小粒子浓度逐渐减小，所以模式计算的斜率接近观测值，但是截距大于观测值，说明模式降水粒子谱参数的描述方案有待改进，模式中谱形参数 μ 不应一直设置为0，而是应该随着高度变化而变化。(朱士超，郭学良)

2.3 霰粒子参数对强对流云降水和催化影响的数值模拟研究

利用三维(3D)对流云AgI催化模式，开展了霰粒子密度和落速参数的敏感性模拟试验，以研究高淞附度时霰粒子参数的选取对催化模拟结果的影响。敏感性试验中对7个霰微物理过程进行了调整。分析发现改变霰落速参数和霰密度，可以引起3 h模拟的总降水量增加4.9%。催化后改变了敏感性试验中霰落速和上升气流的配置，并影响到霰碰并云水和冰晶的过程及霰融化成雨水的过程。在高淞附度云中如果只增加霰密度而没有增加相应的落速系数，将使云中霰含量大幅增加。霰参数也影响了自然云和催化云的降水效率。过量催化使得催化云的降水效率低于自然云。增加霰密度的同时也增加霰落速系数，将使其降水效率高于对照试验，从而影响催化效果。在高淞附度云中采用大密度和较大下落系数，并且利用比数浓度平均落速计算霰粒子比数浓度的下落过程，会使催化效率从25%减少到15%，极大地改变催化效果。所以在高淞附度的暴雨个例中，应当采用高霰密度和相应的高霰落速，否则减雨的催化效果将会被大幅夸大。(楼小凤)

2.4 一次低槽冷锋层状云系结构和过冷水分布特征的模拟研究

利用耦合了CAMS云微物理方案的WRF中尺度模式的模拟结果，结合飞机、卫星、雷达、地面雨量等观测资料，对2012年9月25日山西一次低槽弱冷锋降水层状云系的宏微观结构和过冷水分布特征进行分析，试图研究低槽冷锋层状云系结构特征及过冷水形成的宏微观条件，为人工增雨作业提供依据。模拟的天气形势、降水、云顶温度、雷达回波、水成物的演变与实测基本一致。结果表明：此次降水过程的系统为低槽弱冷锋，且锋面后倾，位于锋前的云系前部为高层冷云，云顶温度 $-40\text{ }^{\circ}\text{C}$ 左右，以冰相粒子组成，没有降水；锋区云系变成高层冷暖混合云，冷区以少量过冷水和大量冰相粒子组成，地面降水最大；处于锋后的云系后部为高层冷云，云顶温度 $-30\text{ }^{\circ}\text{C}$ 左右，不存在过冷水，以较少冰相粒子组成，地面降水较弱。过冷水主要分布在锋面前方低于 $-5\text{ }^{\circ}\text{C}$ 层，高度偏低、含量偏少，过冷水一方面因垂直上升速度供应水汽维持，一方面因冰相粒子的凝华而消耗。过冷水层及其下部上升运动较弱，而其上部上升运动较强，不利于在过冷区长时维持大量液态水，反而促使冰相粒子发展旺盛，此处水汽相对水面不饱和、相对冰晶饱和，大量冰相粒子消耗水汽，不利于过冷水的存在，导致云场仅存在少量过冷水。本次过程中，冰核浓度的增大仅增大冰晶浓度，对雪霰含量及 $0 \sim -5\text{ }^{\circ}\text{C}$ 的过冷水几乎没有影响。(刘涛，孙晶，周毓荃，等)

3 云降水物理室内试验研究

3.1 降温速率对3种类型水滴冻结过程影响的试验研究

大量试验研究表明，水滴的异质冻结既与所含冰核有关又包含一定的随机过程。本研究一方面对已有的试验研究结果进行验证，同时寻找水滴冻结与温度及时间的定量关系，检验随机假设和奇点假设的相互作用。选用雨水、纯净水和瓶装饮用水3种水样，采用中国气象科学研究院的均匀水滴冻结试验装置，对3类水样做了不同的恒定降温速率试验，并对雨水进行了恒温试验。结果表明：随温度

降低降温速率慢的液滴累加冻结比例高于降温速率快的液滴，并且在纯净水和瓶装饮用水中更明显；降温速率越大，平均冻结温度和中值冻结温度越低，不同的是雨水的值跟降温速率成对数关系，而瓶装饮用水的值与降温速率成线性关系（纯净水因为只有2种降温速率，故不能确定是哪一种关系）；不同水样的冻结几率随温度的降低指数增大，而瓶装饮用水冻结几率函数中指数前的系数随降温速率的增大指数减小；恒温阶段，雨水的冻结几率随时间指数衰减，在恒温的前2 min衰减较快，之后减慢，并且水滴冻结在前2 min发生较多，之后变的很少，15 min之后则没有冻结事件发生。该现象可以用随机假设和奇点假设结合起来解释，当温度达到或低于特征温度时，水分子在冻结核上的聚合需要一段时间，所以造成了在恒温阶段出现水滴冻结的现象。水滴冻结是2种假设的共同作用。（万超，石爱丽，周毓荃，等）

4 人工影响天气工程建设及业务工作进展

4.1 全国人工影响天气业务现代化建设三年行动计划

落实《全国人工影响天气业务发展指导意见》，编写完成了《全国人工影响天气业务现代化建设三年行动计划》和《全国人工影响天气业务现代化建设三年行动计划重点任务推进方案》；梳理凝练关键技术和支撑平台，组建了6个由国家级牵头、省级参加的技术团队，负责发展技术方法、形成业务规程、开展应用示范，以带动各省全面推进三年行动计划。组织实施“人工影响天气作业装备弹药全程监控应用示范”项目，充分利用物联网和移动互联技术，推进全国人工影响天气装备弹药的全流程监控以及作业信息的实时采集上报，编制完成《人工影响天气作业信息格式规范》和《人工影响天气装备弹药统一标识技术规范》。组织召开第1届全国人工影响天气中心主任联席会，矫梅燕副局长及有关职能司领导亲临会议作指导。会议分析了发展形势，聚焦人工影响天气业务现代化建设、取得的进展和存在的问题，明确了未来3年人工影响天气的发展方向 and 主要任务。（周毓荃，房文，史月琴，等）

4.2 人工影响天气工程建设

2015年9月29日，第2架新舟60增雨机完成研制交付用户，12月18日，新舟60增雨机在长春龙嘉机场实现首次飞行，第2架增雨机已于12月20日完成交付。完成了第3架（空中国王350）增雨机的采购工作，即将进入建造改装阶段。组织完成了“作业指挥应用软件系统”开发，在东北区域试用。开展版本固化和应用环境规范化工作，遵循气象信息化总体布局和要求，推进在全国各省的推广应用，已先期在宁夏进行试点推广。完成了“信息网络应用系统”“人工增雨效果检验系统”招标采购工作。区域飞机作业保障基地主体建筑已经封顶；完成了79部全球定位系统气象观测（GPS/MET）设备的主体建设工作，56部设备观测资料已经实时上传至东北区域人工影响天气中心及中国气象局。编写培训方案，完成2期“新舟60增雨机云物理探测设备培训班”，全国范围共有百余人次参加培训。举办了3期东北4省区20余名飞机作业人员培训班，初步具备了增雨机作业要求的科研探测能力和增雨作业操作能力。组织开展各区域人工影响天气能力建设可研编修工作，完成西北、中部人工影响天气可研技术审查并报局职能司。组织开展西北、中部区域人工影响天气建设环评、项目用地预审和规划条件、稳评、节能前置工作。（李集明，周毓荃，陈跃，等）

4.3 国家级人工影响天气业务指挥平台

2015年12月17日，国家级人工影响天气业务指挥平台通过减灾司主持的业务验收。其核心业务系统（CPAS-WMC）实现了对卫星、雷达、探空和飞机微物理探测等多源观测信息的实时处理、综合显示和融合处理分析功能，可实现人工影响天气作业条件预报分析、监测预警、作业方案设计、跟踪

指导和作业效果分析等实时业务综合服务。通过平台发布的产品在各省得到了广泛应用，在南京青奥会、北京纪念活动等重大活动保障以及各区域的抗旱中发挥了重要作用。指挥平台实现了面向全国的业务指导、会商指挥、作业监控和信息收集，为省、市、县级建立分级指挥应用树立了标杆，为国家级引领、带动全国人工影响天气业务统一发展提供了有力保障，是人工影响天气在业务化道路上迈出的重要一步。（周毓荃，史月琴，李抗抗，等）

4.4 庐山云雾试验站恢复观测

在我国人工影响天气科研工作的发祥地——庐山，重新启动云雾降水的特种观测试验，搭建了云雾观测平台，选派年轻技术人员轮流值守，开展一期共45天的持续试验观测；实现了庐山外场观测平台远程监控和观测数据每日回传至国家中心；将庐山云雾试验站的历史观测资料进行分类整理，并实现电子化保存；对庐山云雾试验站的建设提出了规划和设想。（郭学良，楼小凤，卢广献，等）

4.5 重大服务保障和日常业务指导

圆满完成北京纪念活动等重大气象服务保障人工消减雨专项服务。成立由3名正研级专家组成的专家组，在军地联合指挥中心负责作业条件分析、作业方案设计和技术把关；在中心本部成立老、中、青相结合的技术组，从作业条件预报、云降水和作业条件监测预警、作业信息收集与效果分析3方面开展工作；装备保障组调配人工影响天气观测设备微波辐射计到河北大厂以支持、保障北京市气象局统一组织的加密观测的要求。组织多次服务保障总结交流，牵头编写完成纪念活动重大气象服务保障技术总结报告。针对北京申办冬奥会，对河南、山东、华北、西南、华南和东北等省和地区出现的干旱开展人工增雨指导服务，采用发专报、联合会商等多种方式开展指导服务。面向全国稳定发布监测和预报等各类产品，收集各类信息，制作各类专报61期。（郭学良，周毓荃，史月琴，等）

4.6 云水资源评估和作业效果检验

开展了云水资源评估结果检验工作，结合吉林、山东、青海和河北等地已有观测资料，对2014年度云水资源监测评估（CWR-MEM）的部分结果进行初步检验。初步探索了各类观测对水汽、云场及云水的检验方案，尝试对CWR-MEM的水汽和云水进行检验。梳理空中云水资源评估的关键技术方法和思路，编写空中CWR-MEM技术指南。优化提炼空中云水资源评估相对较成熟的计算和资料处理技术方法，开展软件化工作，为提供省级应用打下基础。收集、整理、统计和分析了2014年全国各省人工影响天气作业信息，对全国各省地面作业和飞机作业情况进行了详细分析，揭示了全国不同区域的人工增雨作业需求；对人工增雨作业效果统计检验技术方法进行了改进和优化；对播云多普勒雷达识别追踪及检验算法和基于常规雷达探测资料的人工增雨效果物理检验技术方法进行了改进和优化。（蔡森，姚展予，周毓荃）

4.7 人工影响天气装备管理

保障国家级人工影响天气中心现有仪器、装备的稳定运行；编制完成催化剂动静态检测规范；编制高炮火箭功能规格需求书，指导厂商对新型高效冷暖云催化剂WMC-IN-001、002和WMC-CN-001的定型生产。组织编写《人工影响天气专用技术装备使用许可证实施细则》初稿。做好人工影响天气专用技术装备行政许可技术审核各环节工作，受理多项装备研发立项，组织技术方案评审、试验考核，测试、业务试用和列装等工作，及时完成技术报告，提出技术意见上报减灾司。做好全国人工影响天气装备的年检和安全检查工作。组织上海物管处和各省（区、市）气象局建立人工影响天气安全管理制度，定期组织人工影响天气业务安全检查，形成报告上报减灾司。组织相关部门召开炮弹、火箭弹安全工作会议等多次安全生产会议，梳理人工影响天气安全风险隐患。组织做好全国人工影响天气装备2015年的出厂验收、故障等情况的总结。（房文，党娟，方春刚，等）

Advances in Cloud Physics and Weather Modification

1 Observational studies on cloud physics

1.1 Observations of cloud microphysical properties for marine stratocumulus clouds

Cloud microphysical data obtained from G-1 aircraft flights over southeastern Pacific during the Variability of the American Monsoon Systems Ocean-Cloud-Atmosphere-Land Study Regional Experiment field campaign were analyzed for parameter characteristics and microphysical processes of cloud. The horizontal flights were classified by three phases including no drizzle, light drizzle and heavy drizzle. The number concentration, liquid water content, relative dispersion and standard deviation of cloud droplets were calculated. The results show that inhomogeneous mixing was the main process of entrainment and mixing. The relationship of vertical velocity and cloud parameters was analyzed and the results show that the vertical velocity perturbation was in a closer relationship with cloud parameters. (Duan Jing)

1.2 Ice crystal habits and growth processes in stratiform clouds with embedded convection as examined through aircraft observation in North China

Ice crystal habits and growth processes in two cases of stratiform clouds with embedded convection were investigated using data observed simultaneously from three aircrafts on April 18, 2009 and May 1, 2009 as part of the Beijing Cloud Experiment (BCE). The results show that the majority of ice crystal habits found in the two cases at temperatures between 0 °C and -16 °C were plate-like, needle-column, capped-column, dendrite and irregular. A mixture of several ice crystal habits was identified in all of the clouds studied. However, the ice crystals recorded in the embedded convection regions contained more dendrites to be heavier in riming, and the ice crystals identified in the stratiform clouds contained more hexagonal plate crystals. Both riming and aggregation processes played central roles in the broadening of particle size distributions (PSDs), and these processes were more active in embedded convection regions than in stratiform ones. However, riming was more prevalent than aggregation in the April 18 case, though aggregates were evident. In contrast, the May 1 case featured a more dominant aggregation process, which involved riming. With the decrease in height, PSDs broadened in both embedded convection and stratiform regions, but the broadening rates between 4.8 km (-11.6 °C) and 4.2 km (-8 °C) were larger than those between 4.2 km (-8 °C) and 3.6 km (-5 °C). In addition, the broadening rates of PSDs in the embedded convection regions were larger than those in the stratiform clouds, as the aggregation and riming processes of ice particles in embedded convection regions were active. High supercooled water content is critical to enhancing riming and aggregation processes in embedded convection regions. (Zhu Shichao, Guo Xueliang, Lu Guangxian, et al.)

1.3 Characteristics of freezing rain, freezing drizzle, and freezing fog in China from 2011 to 2013

Studying the characteristics of freezing weather in China ultimately helps understand freezing weather more comprehensively. It also contributes to warning and forecasting capabilities for freezing weather, and thus disaster reduction. By using data from hourly or half hourly routine and special observations from civil aviation airports in China for the period 2011–2013, the characteristics of temporal and spatial distribution, duration and synoptic conditions of freezing weather events were analyzed. It is found that the freezing weather events

during the study period occurred in most regions of China. The high-frequency region for freezing rain or freezing drizzle events corresponded well to that of high intensity. In the low-frequency region for freezing fog, events tended to last longer. Freezing weather usually occurred in the winter season (December to February), and mostly in January. Events occurred frequently in the early morning (from 00:00 to 07:00 local time (LT)) and infrequently in the afternoon (from 13:00 to 14:00 LT). The duration of each freezing precipitation event was usually less than 2 h. Most freezing weather events occurred when temperatures were $-3\text{ }^{\circ}\text{C}$ to $-1\text{ }^{\circ}\text{C}$ and dew point was $-4\text{ }^{\circ}\text{C}$ to $-1\text{ }^{\circ}\text{C}$. The highest frequency of freezing weather events occurred when the dew point drop was $0\text{ }^{\circ}\text{C}$ to $1\text{ }^{\circ}\text{C}$. The dominant winds were northeasterly or northerly when freezing precipitation occurred, and the wind speed was usually $2.0\text{--}3.9\text{ m s}^{-1}$. Most freezing rain and freezing drizzle were mixed with fog, whereas freezing fog was not mixed with other precipitation. (Li Jie, Guo Xueliang, Zhou Xiaoning, et al.)

1.4 Study on diagnosing three dimensional cloud region

Cloud mask and relative humidity (RH) provided by Cloudsat products from 2007 to 2008 were statistically analyzed to get RH threshold between cloud and clear sky and its variation with height. A diagnosis method was proposed, based on reanalysis data, to be applied to the three dimensional cloud field diagnosis of a real case. Diagnostic cloud field was compared to satellite, radar and other cloud precipitation observations. Main results are as follows. The cloud region where cloud mask is bigger than 20 has a good spatial and temporal correspondence to the high value relative humidity region, which is given by ECWMF-AUX products. A statistical analysis of the RH frequency distribution within and outside cloud indicates that, distribution of RH in cloud at different height ranges shows a single peak type, the peak of which is near a RH value of 100%. Local atmospheric environment affects the RH distribution outside cloud, which leads to RH distribution varying in different regions and different heights. RH threshold and its vertical distribution used for cloud diagnosis were analyzed with threat score (TS), a method that was applied to a three dimensional cloud diagnosis case study based on NCEP reanalysis data. The diagnosed cloud field was compared to satellite, radar and cloud precipitation observation on ground. It is found that, RH gradient is very big around the cloud region and diagnosed cloud area by RH threshold method is relatively stable. The diagnosed cloud area has a good correspondence to the updraft region. The cloud and clear sky distribution corresponds to the satellite Tbb observations overall. The diagnosed cloud depth, or added cloud layers distribution, is consistent with optical thickness and precipitation on ground. The cloud vertical profile reveals the relationship between cloud vertical structure and weather system clearly. The diagnosed cloud distribution corresponds to cloud observations on ground very well. Precipitation on ground usually can be observed at a deeply-developed cloud area. The evolving cloud vertical structure evolution at a single point over time is well consistent with local radar and surface cloud and precipitation observations. In summary, the diagnosed three-dimensional cloud field and its distribution by relative humidity threshold from the reanalysis data, which are in good agreement with the development and movement of cloud precipitation and weather systems, can be well applied to weather, climate and weather modification research. (Cai Miao, Zhou Yuquan, Ou Jianjun, et al.)

1.5 Analysis of the characteristics and transformation of cloud and precipitation of an extreme torrential rain in Beijing on 21 July 2012

Using the data of Doppler radar, the cloud parameter products retrieved by FY-2E geostationary satellite and MODIS Polar-orbiting satellite, this paper analyzed the structure and transformation of cloud and precipitation of an extreme torrential rain in Beijing on 21 July 2012. It concludes that this process can be divided into three stages with different vertical structure. (1) The first stage, named warm area convective

precipitation, shows that precipitation starts with a warm rain process, in which rain drops grow quickly with significant coagulation in the warm cloud, is important for precipitation. T-Re analysis shows cloud droplets grow quickly below $-10\text{ }^{\circ}\text{C}$ due to significant condensation-coagulation, while there is a deep zone of mixed phases above $-10\text{ }^{\circ}\text{C}$, where the top of cloud is dominated by ice particles. There exists a good positive relationship between thickness, intensity and precipitation, which helps cloud water convert to rainfall quickly. (2) In the second stage, called front convective precipitation, the highly organized low centroid liquid MCC system is the main precipitation system of high rainfall intensity. The cold cloud echo increases quickly at mixing cloud, which is the key area to a microphysical rain forming process. The echo increases to the maximum value from $0\text{ }^{\circ}\text{C}$ level to below 1.5 km, and basically maintains a continued down movement, which reflects rain drops with significant coagulation in the warm cloud, but breaking or evaporation is not obvious. (3) In the final stage (after 22:00), called backward front precipitation, the initial echo at $0\text{ }^{\circ}\text{C}$ level, which increases quickly, shows ice particles coagulate with cloud water by an accretion process. The echo profile shows there exists obvious evaporation at the early precipitation. With the cloud development, the echo basically maintains itself, which shows cloud water is less in the warm cloud, and rain drops can not grow with significant coagulation. (Zhou Yuquan, Jiang Yuanhua, Cai Miao)

1.6 Spatial-temporal distribution of summer cloud water resources over the Loess Plateau from 1979 to 2012

Spatial and temporal distribution features of cloud water resources over the Loess Plateau in summer from 1979 to 2012 were analyzed by using ERA-Interim dataset issued by European Centre for Medium Range Weather Forecasts (ECMWF). Results are as follows: (1) Cloud water resources far outnumber than the actual amounts of precipitation in summer, leaving a great potential for their exploitation. (2) The distribution of cloud water resources is in two main modes: firstly, anti-phase oscillation appears between the northwest and the southeast (EOF1); Secondly, cloud water resources are abundant in the center of the Loess Plateau, while they are not in the northwest and the southeast regions (EOF2). The associated time series of EOF1 and EOF2 also feature a significant inter-annual cycle. (3) The cloud water resources over the Loess Plateau come from the East China Sea. So when the center of the water vapor transporting an anti-cyclonic circulation is southerly (northerly), the spatial mode EOF1 (EOF2) is influenced. (4) The amount of cloud water and cloud ice reach the peak value at about 700 hPa and 400 hPa, respectively. Therefore, cloud water resources are advisably exploited at a time that water vapor converges and moves upward at 700 hPa. (Pan Liujie, Zhang Hongfang, Zhou Yuquan, et al.)

1.7 Airborne observation based analysis of aerosols beneath the summer clouds over Sichuan Basin

With the purpose of studying the clouds and aerosols over Sichuan Basin, two observation experiments were performed with the PMS probes mounted on a Cheyenne III A aircraft on June 23, 2009. The observation data via PCASP-100X probe of the PMS from two flights beneath the clouds in one day were analyzed as well as the CERES SYN1deg-3Hour Ed3A data in the same day. In addition, the backward and forward trajectories during flying courses were studied with the NOAA HYSPLIT model. By doing so, the vertical distribution, size spectrum distribution and source characteristics of the observed aerosols over Sichuan Basin are addressed in this paper. The results show that: the atmospheric aerosols over the cities and towns in Sichuan Basin are mainly from the ground surface, and the long-distance transportation contributes little to the volume of aerosol particles over Sichuan Basin, i.e., the aerosols over Sichuan Basin are attributed mostly to the regional or local pollutants.

Afterwards, the aerosol particles concentrate over Sichuan Basin. The boundary layer structure is influenced by clouds, precipitation, seasons, sunshine, temperature, thermal inversion, and surface heating. In the meantime, the vertical distribution of aerosol particles is influenced greatly by the boundary layer structure. In summer, the aerosol particles heavily and vertically mix in the deep mixing layer during daytime, while the aerosol particles over the mixing layer decrease sharply. Also, the concentration magnitude of the observed atmospheric aerosol particles over the cities and towns in Sichuan Basin is between 10^8 m^{-3} and 10^9 m^{-3} , which is the same as that of the atmospheric aerosol particles over cities in Hebei Province, Beijing and its surrounding areas. The majority of the observed aerosol particles beneath the clouds are small ones. The concentration of the aerosol particles declines along with the increasing size. Additionally, the Angstrom exponents of the aerosol particles are between 1.2 and 1.4, which obviously characterizes the urban-industry aerosol. (Wang Weijia, Guo Xueliang, Li Hongyu, et al.)

1.8 Analysis of topographic cloud on different slopes as observed by X-band dual-polarized radar

Based on the topographic cloud cases over Qilian Mountain as observed by an X-band dual-polarized Doppler weather radar, the characteristics of different topographic clouds on 3° , 9° and 14° terrain slopes and different weather systems were analyzed. The results show that the topographic clouds over Qilian Mountain in summer were significantly different under different terrain slopes and airflow of weather system conditions. These differences appeared in number, intensity, internal dynamics, microphysical process and dominant particle distribution of cloud cells. Therefore, the further research on topographic clouds with different conditions would help to scientifically produce artificial rainfall from topographic clouds. (Ma Xueqian, Chen Yue, Zhang Guoqing, et al.)

2 Cloud physics and artificial seeding simulation research

2.1 A numerical study on precipitation process and moisture budget of stratiform and embedded convective cloud over Beijing area

In this study, the precipitation process of stratiform and embedded convective cloud during 5–6 October 2007 in the Beijing area was simulated using the Chinese Academy of Meteorological Sciences mesoscale cloud model. Based on observation data, the characteristics of the macro- and micro-structures of the cloud system and precipitation were analyzed. The moisture budget and precipitation efficiency of the cloud system were also analyzed. The results show that the stratiform and embedded convective cloud was the main precipitation cloud system in this Beijing-precipitation process. The precipitation distribution of the stratiform and embedded convective cloud was not uniform. In addition, the microphysical variables in the cloud system were not uniform in the horizontal or vertical directions. The stratiform and embedded convective cloud over the Beijing area was characterized with the microphysical structure of a mixed phase cloud. The melting of snow was the main microphysical process contributing to raindrop formation. The main source region of water vapor for this precipitation process in the Beijing area was the Yellow Sea and Mongolia. Two air flows merged in the north of the Shaanxi Province to form a southwest airflow that transported water vapor to North China. Outside the Beijing area, water vapor and hydrometeor were mainly transported to the region from the western and southern boundaries. In the main precipitation period in the Beijing area, the flux of the total water substance in the horizontal direction was the net inflow. The estimation of the water budget of the water vapor, hydrometeor, and total water substance shows that the water substance was generally balanced. The precipitation efficiency, condensation rate, deposition rate, and hydrometeor precipitation efficiency were 5.6%,

4.77%, 4.19%, and 44.9%, respectively, in the Beijing area from 20:00 BJT (Beijing time) 5 October to 14:00 BJT 6 October 2007. (Tao Yue, Li Junxia, Dang Juan, et al.)

2.2 A comparison of WRF-model-simulated cloud microphysics and precipitation in stratiform clouds with embedded convection in North China with aircraft measurements

To verify the cloud microphysical scheme and to simulate cloud microphysics and precipitation, the authors used the Weather Research and Forecasting (WRF) model to simulate their characteristics in stratiform clouds with embedded convection for April 18, 2009, and then compared the results with data obtained during the Beijing Cloud Experiment (BCE). The results indicate that the distributions of the cloud system, radar echo, and precipitations as simulated by the WRF model are in good agreement with our observations. The simulated liquid water content (LWC) is consistent with aircraft measurements, and the maximum LWCs at the $-8\text{ }^{\circ}\text{C}$ and $3\text{ }^{\circ}\text{C}$ layers as observed by the aircraft are 1.5 g m^{-3} and 0.8 g m^{-3} , and those simulated by the model are 1.1 g m^{-3} and 0.78 g m^{-3} , respectively. Vertical distributions below the $-5\text{ }^{\circ}\text{C}$ layer (most cloud water is LWC) were properly simulated, with the melting layer included. The ice water content (IWC) simulated by the model was higher than that observed in the range of -6 to $-10\text{ }^{\circ}\text{C}$ layer because the simulated riming process was excessive at this layer, and the aggregation process occurred in a higher layer. As such, modifications are required for cold simulation processes. At the $-8\text{ }^{\circ}\text{C}$ layer, both the intercept and slope of the particle size distributions (PSDs) simulated by the model were lower than those of the observations due to the simulated snow mass concentrations being higher than observed. At the $-5\text{ }^{\circ}\text{C}$ layer, both the simulated intercept and slope were consistent with observations. At the $3\text{ }^{\circ}\text{C}$ layer, the simulated slope was consistent with observations, but the simulated intercept was higher than the observed value due to the decreasing concentration of small particles in the cloud, which suggests that the spectrum-shape parameter could change with the cloud height. (Zhu Shichao, Guo Xueliang)

2.3 Numerical simulation based study of the impacts of graupel parameters on strong convective rainfall and seeding effects

By using a three-dimensional convective cloud model with the AgI seeding scheme, sensitivity simulations were conducted with various graupel densities and fall velocities. These parameters influence seven microphysical processes of graupel particles. Numerical simulations show that these parameters affect rainfall amount as much as 4.9%. The relationship between graupel fall velocities and wind updrafts is modified after seeding, and the values of collection of cloud water by graupel, collection of ice by graupel, and melting of graupel to rain water are influenced. When only graupel density is increased, graupel mixing ratios are increased significantly. Graupel density and fall speed parameters also change the rainfall efficiency of both seeding and natural clouds. Increasing the graupel density along with the fall velocity parameter results in relatively high rainfall efficiency, with the seeding effects being only 15% rather than 25% as noted in the control seeding simulation. Therefore, in the simulation of the rime density of convective clouds, both the graupel density and fall velocity parameters should be increased; Otherwise, the seeding effect will be significantly exaggerated. (Lou Xiaofeng)

2.4 A Simulation based study on trough cold front cloud structure and the characteristic of supercooled water distribution

An analysis focused on precipitation cloud structure and the characteristic of supercooled water distribution was made of a weak trough cold front process in Shanxi on September 25, 2012. Combined with observation data, including aircraft detection, satellite and radar remote sensing, ground precipitation, WRF mesoscale model coupled with WRF-CAMS cloud microphysical scheme was used. The attempt to study the

low trough layered structure of a cold front through the clouds and the formation of macro- and micro- cold conditions was to provide the basis for artificial rainfall. The simulated weather situation, precipitation, cloud top temperature, radar echo and the evolving water were basically consistent with the observation data. Main results are as follows: The precipitation process system was a weak trough cold front and frontal tilt backward. The cloud top temperature of the top cold cloud, 200 km outside the front of the cold front, was about $-40\text{ }^{\circ}\text{C}$, composed of ice-phase particles and without precipitation. Within 200 km in front of the cold front, cloud was mixed into a high-level cloud, with the cold zone having a small amount of cold water and a lot of ice-phase particles, and surface precipitation reaching maximum. The cloud system behind the cold front was high-rise cold clouds, with the temperature in the cloud top being about $-30\text{ }^{\circ}\text{C}$, and no super-cooled water being found. Being composed of less ice phase particles, the system was weak in surface precipitation. Supercooled water existed below $-5\text{ }^{\circ}\text{C}$ layer, the content of which was low, and the distribution of which was related to the development of vertical velocity and ice phase particles. The vertical motion of supercooled water and its lower layer was weak while the upper area was of a strong vertical motion. This was not conducive to the maintenance of a large amount of supercooled liquid water at the top. On the contrary, the development of strong ice phase particles was promoted and excessive consumption of supercooled water ice phase particles was not conducive to the continued existence of supercooled water, resulting in the presence of only a little supercooled water in the clouds. (Liu Tao, Sun Jing, Zhou Yuquan, et al.)

3 Experimental studies of clouds and precipitation

3.1 Experimental study of the impact of cooling rate on the freezing process of three kinds of water drops

A large number of the previous experimental studies have indicated that heterogeneous freezing is caused by nucleus contained in drops and stochastic processes both. In this research, experiments were designed to verify the previous experiment results. On the other hand, a quantitative relationship of the freezing phenomenon of water drops with temperature and time was also studied. Besides, the interaction of the stochastic hypothesis with the singular hypothesis was also examined. The constant cooling rate experiments for rain water, pure water and bottled water, and the constant temperature experiment for rain water only, were conducted using a freezing experimental device of uniform drops designed by the Chinese Academy of Meteorological Sciences. From the results, it is seen that while the temperature decreases, the accumulative freezing fraction in the slow cooling rate experiment is larger than that in the fast cooling rate experiment in general. This phenomenon is more obvious for pure water and bottled water. The faster cooling rate corresponds to the lower average freezing temperature and median freezing temperature. However, the relationship between freezing temperature and cooling rate in rain water is logarithmic while their relationship is linear in bottled water (there are only two rates of cooling in pure water experiment, so it is not certain of their relationship). The probability of freezing increases exponentially with the decreasing temperature in each water sample, and in the probability of freezing function, the exponential coefficient decreases exponentially with the increasing cooling rate in bottled water; during the constant temperature period, the probability of freezing decays exponentially with time in rain water. The decay is faster in the first two minutes and slower later. No freezing event occurs after 15 minutes. This phenomenon can be explained by combining the stochastic hypothesis and singular hypothesis as follows: When the temperature of drops reaches or is lower than the characteristic temperature, water molecules need a period of time to aggregate on freezing nucleus, which leads to the freezing of drops in constant temperature period. Freezing of drops is caused by a combined

effect of the two hypotheses. (Wan Chao, Shi Aili, Zhou Yuquan, et al.)

4 Weather modification capacity-building and operation

4.1 Three-year action plan of the national weather modification operational modernization program

In 2015, CMA Weather Modification Center (WMC) implemented the “National Weather Modification Operation Guidance” and finished writing “Three-year Action Plan for the National Weather Modification Operational Modernization Program” and “The Scheme for Issues on ‘Three-year Action Plan for the National Weather Modification Operational Modernization Program’”; reviewed the key technologies and the supporting platform; set up six technical teams consisting of employees from both national and provincial centers to develop technical methods, prepare operational procedures, and launch demonstration initiatives for deployment to facilitate the implementation of the three-year action plan at provincial level.

CMA WMC also implemented the project of “Application Oriented Demonstration of the Process-wide Monitoring of Equipment and Ammunition for Weather Modification Operations” by making full use of the Internet of Things (IoT) and mobile Internet technology to promote the process-wide monitoring and the real-time collection and reporting of information on weather modification operations; to document “Weather Modification Operations Information Format Specification” and “Unified Technical Specifications for Identification of Weather Modification Operation Equipment and Ammunition”.

CMA WMC held the first national directors joint meeting for weather modification. Ms Jiao Meiyuan, Deputy Administrator of CMA, and directors-general from relevant departments in CMA attended the meeting. The meeting analyzed the development trend, focusing on the weather modification operational modernization development; discussed the current progress and problems, pointing out a clear development direction and main tasks for the next three years in this connection. (Zhou Yuquan, Fang Wen, Shi Yueqing, et al.)

4.2 Progress with weather modification projects

The first Modem Ark 60 (MA60) artificial precipitation aircraft was delivered to the user on September 29, 2015. And on December 18, MA60 artificial precipitation aircraft made a successful test flight in Changchun airport. On December 20, the second artificial precipitation machine was delivered. By the end of 2015, the third artificial precipitation machine (King Air 350), which was finished with the procurement process, was to be made and retrofitted.

CMA WMC completed the development of “Application Software System for Operation Control”, which went through a trial test in the northeast region. WMC also carried out the solidification of the software version and the standardization of its application, which followed the overall meteorological information planning and requirements. Besides, WMC promoted its deployment and application at provincial level, with Ningxia as a pilot site.

CMA WMC accomplished the bidding processes for projects of “Information Network Application System” and “Weather Modification Effect Inspection System”. The main building of the regional aircraft operation supporting base has been capped. The construction of the major parts of 79 GPS weather observation (GPS/MET) systems has been completed. Real-time observation data from 56 devices have been uploaded to the Weather Modification Center in Northeast Region and China Meteorological Administration.

CMA WMC completed the preparation of a training scheme; finished two training programs on MA60 Artificial Precipitation Cloud Physics Machine Detection Equipment with more than one hundred participants from across the country; organized three courses for more than 20 aircraft operating personnel from four

northeastern provinces to provide them with the ability for basic scientific research and operation for artificial precipitation.

CMA WMC carried out the preparation of project feasibility studies on regional weather modification centers' capacity-building and finished the technical review of the reports for northwestern and central regions, which were submitted to CMA head office. CMA WMC also helped to implement the environment assessment, preliminary review, project planning, stability assessment, and energy-saving for weather modification projects in these two regions. (Li Jiming, Zhou Yuquan, Chen Yue, et al.)

4.3 National weather modification operational command platform

The National Weather Modification Operational Command Platform hosted by Disaster Mitigation Department, CMA went through the project acceptance on December 17, 2015. Its core operation system (CPAS-WMC) includes the functions as follows: The ability for real-time information processing, integrated display and fusion analysis of multi-sources coming from satellite, radar, aircraft and micro-physical sounding; the function of real-time integrated operational service for forecast analysis, monitoring, operation scheme design, operation tracking guidance and operation effect analysis. Products published by the platform have been widely applied at provincial level, and played an important role in major events, for example Nanjing Youth Olympic Games, Beijing Commemorative activities and drought-relief efforts in related regions all over the country.

The command platform achieved the function of operational guidance, video conferencing and consultation, operation monitoring and information gathering at the national level, setting the benchmark for its replication at provincial, municipal and county levels. It also provided a strong guarantee for the development of a unified national weather modification service, hence an important step toward the operational running. (Zhou Yuquan, Shi Yueqing, Li Kangkang, et al.)

4.4 Resumed observation at Lushan Station for cloud and fog experiment

Fog, cloud and precipitation observation at Lushan Station, which is one of the original places for weather modification research in China, was resumed. The fog and cloud observation platform at the station was built, where several young researchers and technicians carried out continuous observation for 45 days. A remote monitoring system for the platform was constructed to allow observation data to be sent to the national center every day. The historical observation data at Lushan Station were classified and digitalized to facilitate their storage. The redevelopment plan on the Lushan Station was proposed. (Guo Xueliang, Lou Xiaofeng, Lu Guangxian, et al.)

4.5 Major service supports and daily work guidance

The supports included are as below: Providing the special support to artificial rain reduction in meteorological service of major celebrations such as Beijing Commemorative activities; establishing a technical team consisting of three senior experts who are responsible for the operation condition analysis, operation design and technical checks in joint military-civilian command center; setting up a group of young and old engineers stationed in the center headquarters, which is in charge of operation conditions forecast, precipitation monitoring, early warning of operation conditions, the operation effect information collection and analysis; deploying microwave radiometer to Hebei for the purpose of intensive observations organized by Beijing Meteorological Bureau; organizing several service support workshops; finishing the technical report on major meteorological service support.

CMA WMC offered the guidance services on artificial rainfall enhancement for Henan, Shandong, North China, Southwest and South China to deal with drought in the ways of bulletins and consultation, and to help

Beijing's bid for the Winter Olympics. There were 61 bulletins covering the thorough information. (Guo Xueliang, Zhou Yuquan, Shi Yueqing, et al.)

4.6 Cloud and water resources assessment and verification

CMA WMC carried out the verification of cloud and water resources assessment. By combining the existing observation data from provinces of Jilin, Shandong, Qinghai, Hebei and others, some results of the 2014 annual CWR-MEM program evaluation have gone through a preliminary verification. We explored preliminarily the verification scheme for the observation of water vapor, cloud water and cloud fields, trying to test the differences between water vapor and cloud water in CWR-MEM. Besides, our team also reviewed the key technical ways and ideas on cloud and water resources assessment, and wrote the technical manual on "Guidelines for Cloud and Water Resources Monitoring and Assessment (CWR-MEM)". Last, we successfully optimized the cloud and water resources assessment computing methods and data processing techniques on a software basis to facilitate the provincial application.

We also accomplished the following tasks: By collecting, counting, analyzing the national weather modification operations in 2014, altogether with a detailed analysis of national ground operations and aircraft operations, the demand of artificial rainfall enhancement operations in different regions of the country was revealed. The effects of technical methods for artificial rainfall were verified and improved. The technical methods for cloud seeding Doppler radar tracking and recognition algorithm and the physical verification methodology for the effect of artificial precipitation based on conventional radar data have also been improved and optimized. (Cai Miao, Yao Zhanyu, Zhou Yuquan)

4.7 Weather modification equipment management

The jobs include keeping the existing equipment in national center under stable operation; completing the standard file on the cloud-seeding agent static and dynamic testing; writing the specifications on antiaircraft rockets; offering guidance for products of new efficient cold and warm cloud-seeding agents.

The progress is as follows: Finished the first version of "Implementation Details on Weather Modification Using Special Technical Equipment"; accomplished the evaluation; approved the research projects; organized the assessment, testing/evaluation, trial operations, and adoption; wrote the technical report; submitted the report to CMA Disaster Reduction Department.

The additional progress is: Finished the annual inspection and security check of the national weather modification operational equipment; established the security management system for weather modification operations conducted by Shanghai Property Management Department and meteorological bureaus of provincial level; carried out regular safety inspection of weather modification operations, made and submitted a report to CMA Disaster Reduction Department; organized the meetings on artillery and rockets; reviewed the weather modification security risks; made a 2015 annual countrywide summary of weather modification equipment in terms of factory acceptance and failure conditions. (Fang Wen, Dangjuan, Fang Chungang, et al.)

生态环境与农业气象 Ecological Environment and Agrometeorology

生态与农业气象研究进展

1 农业气候资源与农业气象灾害预报预警

1.1 重大农业气象灾害立体监测与动态评估技术

通过对西南玉米和水稻干旱、南方双季稻低温、黄淮海小麦干热风不同灾害的立体监测与动态评估技术的研究，提出上述不同农业气象灾害的致灾气象指标和灾害分级指标体系，研发了可在气象业务中应用的基于地面观测、卫星遥感和作物模式相结合的不同灾害的立体监测技术和动态评估的技术方法。该项目所研究解决的农业气象灾害监测与评估中的关键技术是针对我国农业生产模式和灾害对象，具有明显的地域性和现实性等特点，同时也是针对气象和农业部门的业务需求和决策服务的需求而展开的，因此本项目的实施，可以比较显著地提高我国农业气象灾害的监测和评估能力。(赵艳霞)

1.2 省级冬小麦精细化土壤墒情和灌溉预报系统

研究了遥感地表蒸散亏缺指数反演方法，结合人工和自动观测土壤湿度资料，采用神经网络法，获取了可靠、高分辨率的土壤水分初始场。对前期估算的 a 、 b 系数进行检验，并与FAO推荐值($a = 0.25$ 、 $b = 0.5$)作对比，发现绝大多数站各月实际 a 、 b 系数的均方根误差比FAO小。研究建立了冬小麦根系最大根长模型，构建了适合我国北方冬小麦区的 a 、 b 系数、冬小麦作物系数、土壤分层蒸散系数、土壤水分胁迫系数，完善了3个省级冬小麦精细化土壤墒情和灌溉预报系统，并在2015年冬小麦生长季继续开展业务化中试、区域验证和准业务化应用，预报精度达80%以上。(毛飞)

1.3 南方双季稻低温灾害的动态预警技术

基于近50年南方双季稻低温灾害发生趋势与风险地理分区，建立了双季稻第1次低温灾害等级预测，早稻未来10天、晚稻未来5天的低温灾害等级动态预警模型。按双季稻I区(高风险区)、II区(增加趋势区)、III区(低风险和减少趋势区)，分粳稻、籼稻分别建立了基于大气环流特征量的双季稻历年第1次低温灾害发生等级预测模型，平均外延预测基本一致正确率均在83%以上；基于Fisher判别分析的早稻未来10天、晚稻未来5天的低温灾害等级逐日滚动预警模型，平均外延预测基本一致正确率在80%以上。实现了双季稻低温灾害发生趋势、风险地理分区与灾害发生等级预测预警的有机结合，提升了预测预警的区域针对性。(霍治国)

1.4 南方地区农业洪涝灾害综合风险评估模型

基于单站洪涝等级原型指标的过程降水量临界值增减得到101~151个洪涝指标，分别构建洪涝指数并与农业洪涝实际受灾程度进行吻合性分析，建立了长江中下游、西南地区11个分省农业洪涝等级指标；发展了基于灾害风险逆过程分析的灾害等级指标临界阈值厘定方法，建立了西南一季稻、湖南早稻洪涝、江淮夏玉米涝渍等级指标；编制了区域农业、水稻洪涝、夏玉米涝渍时空分布图。基于受灾面积、受灾人口、直接经济损失比重等相对灾情指标，构建了南方洪涝灾害综合相对灾情指数及

其风险估算模型,该模型较好地反映了12个省份每年受灾的差异情况。解决了基于降水过程的农业、水稻洪涝、夏玉米涝渍等级阈值确定、分省指标可比性等关键技术问题,为灾害实时监测预警评估的业务发展提供了指标支撑(图1~2)。(霍治国)

1.5 海南冬季瓜菜气象灾害综合风险区划

构建了基于湿涝指数的海南冬季瓜菜(西瓜、辣椒、豇豆、丝瓜)苗期湿涝、过程积寒的瓜菜冬季寒害、干旱指数的瓜菜冬季及春季干旱等级评价指标;综合瓜菜气象灾害致灾因子危险性、孕灾环境敏感性、承灾体易损性和防灾减灾能力,编制了瓜菜苗期湿涝、冬季干旱风险以及综合风险区划图。解决了瓜菜气象灾害致灾、孕灾、灾损、防灾能力指数的分灾种构建与量化、多灾种综合权重厘定等关键技术问题,为因地制宜地指导瓜菜减灾避灾和生产优化布局提供了科技支撑(图3)。(霍治国)

1.6 玉米对干旱过程响应的生理机制

初步分析了夏玉米水分胁迫试验数据中不同水分状况对夏玉米叶绿素和光合参数的影响。结果表明,轻度稳定干旱和重度稳定干旱均显著降低了玉米叶片的叶绿素相对含量(SPAD)。但在灌浆后期,轻度稳定干旱处理的玉米叶片SPAD没有再降低,且有增加的趋势,而严重稳定干旱处理则一直呈下降趋势,这或许说明了玉米叶片对干旱的适应性响应:当干旱强度较轻时,表现出了适应的一面,而当干旱达到一定严重程度时,则适应性降低。2种稳定干旱和2种持续干旱处理下,净光饱和光合速率(Asat)均显著下降,明显抑制了叶片的净固碳速率。玉米叶片在光适应下,光系统II的光化学效率在干旱处理初期未见下降,且出现了一定的适应性响应,但严重干旱处理的叶片则没有表现出这种适应性响应。(周莉)

1.7 黄淮海平原冬小麦-夏玉米轮作系统耗水特征

以黄淮海2011—2012年MODIS遥感影像、气象数据、田间观测资料和地面调查数据为主要数据源,估算了冬小麦和夏玉米实际蒸散量,揭示了周年内作物耗水时空分异特征,明确了黄淮海地区作物用水结构特征。结果表明,2011—2012年夏玉米耗水量的97.21%来源于降水,河北南部、河南中、北部地区灌溉量占玉米总耗水量的10%左右。73.3%的冬小麦耗水量来源于灌溉,其中河南、河北冬小麦灌溉量占总耗水量的80%以上。(杨建莹)

1.8 不同水分胁迫对冬小麦生长发育的影响

在中国气象局固城生态与农业气象试验站(以下简称固城站),开展了连续2年(2013—2014年度和2014—2015年度)的土壤水分胁迫野外观测试验,以研究不同水分胁迫条件对冬小麦生长发育的影响。研究表明,冬小麦全生育期供水越少,冬小麦的结构参数(植株密度和株高)和功能参数(叶面积指数和生物量)与对照的回归系数越小,整体表现为重度干旱<中度干旱<轻度干旱,说明干旱程度对冬小麦的生长发育影响较大。不同水分胁迫条件下,冬小麦全生育期的实际蒸散量和发育期长度也表现出较大的差异,即随着干旱程度的加重,冬小麦的实际蒸散量表现为明显的下降趋势,全发育期长度则由于干旱逼熟而呈现明显的缩短趋势(图4)。(王培娟)

1.9 华北地区冬小麦作物系数

利用固城站冬小麦生长期内的气象和涡度相关数据,分别计算了冬小麦生长期内的潜在蒸散(ET_0)和实际蒸散(ET_a),在此基础上计算了冬小麦生长期内各关键发育阶段和逐旬作物系数(K_c)。结果表明,冬小麦作物系数呈明显的“双峰型”曲线特征,与FAO推荐的“三点四段”式作物系数相比,能够更精细地刻画冬小麦不同发育阶段的需水规律。此外,利用冬小麦“双峰型”和FAO推荐的作物系数,结合2011—2012年度固城冬小麦生长期内潜在蒸散数据,分别计算了冬小麦实际蒸散量,

并利用逐日和各发育阶段潜热通量数据进行验证。结果表明,利用“双峰型”作物系数计算的 ET_0 在2种时间尺度上的线性回归系数均较FAO方法更接近1,在逐日和各发育阶段分别是1.150和1.243,较FAO方法分别低0.106和0.111。(王培娟)

1.10 夏玉米苗期干旱敏感指标及其临界值

研究发现夏玉米的茎含水率、叶含水率、蒸腾速率、光合速率、气孔导度和叶面积指数(LAI)对苗期干旱最为敏感,其受旱临界点的土壤湿度阈值分别为74.7%、65.6%、62.0%、61.5%、59.1%和46.8%,反映了夏玉米苗期各干旱指标敏感程度。建立了基于遥感信息(植被指数NDVI和地表温度)和常规气象观测(气温)的夏玉米土壤水分反演关系,该反演关系可以很好地给出夏玉米不同深度土壤相对湿度。通过比较高光谱遥感植被指数对玉米冠层含水量的反演与估算能力,指出叶绿素类指数 Cl_{green} (green chlorophyll index)对冠层含水量变异的响应最敏感,进而初步构建了适用于宽幅变异冠层含水量的普适性高光谱遥感估算方法(图5)。(周广胜)

2 农业对气候变化的响应与适应

2.1 黄淮海地区玉米品种对气候变化的适应性

研究选用RegCM4模式在RCP4.5和RCP8.5情景下生成的气候数据,与APSIM模型结合,量化了气候变化对玉米产量的负面影响。此外,玉米产量很大程度上取决于籽粒数。而籽粒数对于开花阶段高温等环境胁迫的影响非常敏感。为了适应未来不断升高的温度,增加籽粒耐热性可能是未来适宜的品种特性。为此,我们将原有品种籽粒耐高温的能力从38℃提高到40℃作为耐高温品种。结果表明,耐高温品种的应用较传统品种相比,产量增加大约4%。(赵艳霞,张祎)

2.2 大气CO₂浓度升高和增温对作物需水量变化影响机理

经过3年试验研究,基本探明了增温和CO₂浓度增加影响小麦需水量变化的途径和机理:(1)增温增加了小麦的日耗水量,但增温缩短小麦生育期长度从而减少全生育期耗水量。增温对小麦需水量的影响是日耗水量增加和全生育期日数减少共同平衡的结果。(2)CO₂浓度升高增加了叶片尤其是旗叶含水量和干物质,同时,CO₂浓度升高有增加小麦生育期日数的趋势,最终增加了小麦生育期需水量。试验观测结果表明,每增温1℃,小麦日均需水量增加12%,全生育期需水量增加10%~15%。CO₂浓度倍增,小麦需水量增加25.6%。然而,增温和CO₂浓度升高共同影响小麦需水量的综合结果还不确定,需要进一步深入研究。(俄有浩)

2.3 湿地(稻田和芦苇)土壤冻融对CO₂排放过程的响应机制

通过冻融对水稻和芦苇湿地生态系统碳交换的观测分析,发现土壤冻融日循环能激发水稻农田和芦苇湿地土壤CO₂的排放,冻融期土壤CO₂排放量占各类型生态系统CO₂年排放总量的比例分别为14.1%和12.5%,在年排放总量估算中不容忽视。由于冻融导致的土壤CO₂排放增量,对于研究中的水稻农田和芦苇湿地分别占各类型生态系统CO₂年排放总量的4.01%和4.46%,日冻融循环导致的土壤CO₂排放增量与5~10cm土壤温度正相关($R^2 = 0.57$)(图6)。(周莉)

2.4 北方一熟区主要旱地作物与气象要素的相关性

基于APSIM模型对春小麦和春玉米生长发育及产量形成过程进行了模拟。APSIM模型对内蒙古地区春小麦、春玉米生育期模拟结果和实测数据相关关系较好。春小麦开花期日序与平均温度呈极显著相关,与土壤温度呈显著相关,与降水、太阳辐射和潜在蒸散量不相关;成熟期日序与平均温度呈极

显著相关，与土壤温度呈极显著相关，与潜在蒸散量呈显著相关；同时与降水和太阳辐射不相关。春玉米开花期日序与气象因子都不相关；成熟期日序与平均温度呈极显著相关，与风呈极显著相关，与土壤温度呈极显著相关，与相对湿度呈显著相关；同时与降水、太阳辐射和潜在蒸散不相关。（赵俊芳）

2.5 气候变化对东北玉米产量影响的不确定性

研究利用3套气候模式数据代表气候输出的不确定性，分别驱动2个作物模型代表模型结构不确定性，以辽宁省庄河农气站为例，对气候变化不确定性进行了评价。多模式集合模拟表明，相对于1971—2000年基准时段，未来2021—2050年玉米减产约13%，减产概率为80%。集合产量方差分析显示量化了未来气候变化下来自气候模式不确定性大于作物模型结构不确定性对集合产量不确定性的影响。气候模式降到站点尺度的偏差对最终产量不确定性有明显影响。研究进一步考虑由8个全球气候模式和3个排放情景组成的24个气候模式数据代表气候输出不确定性，与各包含100组参数的2个统计模型代表的作物模型内部参数不确定性相结合，以辽宁省本溪、吉林省长岭、黑龙江省海伦农气站为研究地点进行了评价。集合结果显示未来气候变化下玉米产量降低不足5%。此外，方差分析结果显示未来气候变化下气候模式不确定性远大于作物模型参数不确定性对集合产量不确定性的影响。（张祎）

2.6 增温与CO₂浓度升高对冬小麦的协同影响

继续开展冬小麦生长季CO₂浓度升高和增温控制处理试验，全生育期CO₂浓度变化范围为 $(603 \pm 55) \times 10^{-6}$ ，昼夜增温幅度分别为 1.6 ± 0.6 °C和 3.9 ± 0.5 °C。复合处理推迟播种12天。试验结果表明，当日平均气温升高2.8 °C， 600×10^{-6} CO₂浓度不能弥补增温对冬小麦生长与产量的不利影响。复合处理对冬小麦产量的影响机制在于增温使冬小麦冬后发育期大幅提前，冬后生育期温度不但没有升高反而降低，同时，冬后生育期接收太阳辐射量减少，这样消弱和部分抵消了CO₂浓度升高的施肥效应。另外发育期大幅提前增加了冬小麦遭遇晚霜冻或抽穗期低温威胁的几率，这是造成冬小麦穗粒数下降和减产的主要原因。（谭凯炎）

2.7 小麦物候对气候变暖的非线性响应特征

利用物候和气象观测数据首先分析了全国小麦物候期与前期温度的总体关系，结果表明，春小麦播种、出苗和分蘖期与前期温度呈非线性关系，但从拔节开始则基本呈线性关系，而冬小麦的情况与此正好相反。考察了不同地区间的差异后看出，陕甘宁和新疆地区春小麦成熟期随前期温度变化为“凹”型曲线，而其余各地两者的关系均呈线性相关。最后探讨了小麦不同发育时段持续天数对前期平均气温变化的响应特征，结果发现，春小麦出苗到乳熟、出苗到成熟的持续天数随前期温度升高而线性减少，冬小麦出苗到分蘖、出苗到停止生长和出苗到返青期的持续时间与前期温度线性相关，而出苗到拔节、出苗到抽穗、出苗到乳熟和出苗到成熟各阶段的持续天数与前期温度变化呈“凸”型曲线相关。（马玉平）

2.8 气候变化对东北农业气候资源的影响

利用东北地区（黑龙江、吉林、辽宁、内蒙古东四盟）1961—2010年91个气象站观测资料与区域气候模式模拟的1951—2009年格点气象资料，分析了主要气候要素、农业气候资源的时空变化趋势。气候变化背景下，2010—2099年东北地区气候资源变化显著，温度升高，降水稍有减少。气候向变暖、变干方向发展，这会对农业生产产生一定的影响。气候变化的结果使得东北地区的农业热量资源更加充足，表现为 ≥ 10 °C初日提前，初霜日推迟，可能生育期逐渐延长，使得可利用的农业热量资源更加丰富。积温的增加会将原有种植区域扩大，使得晚熟品种的农作物种植更加广泛以及不能种植农作物区域减小。如东北春玉米生长所需最低积温为2100 °C·d，到2090年代，黑龙江省春玉米不可种植地带由1950年代小兴安岭以北大部分区域缩减到只有漠河区域，但降水量减少可能对农业生产产生不利

影响。(郭建平)

2.9 中国极端高温和低温天数的变化趋势及其突变

中国已开展的极端气温研究多以发生概率10%作为极端气温的相对阈值，而对人类健康或者生物影响较大的发生概率更低（5%或者1%）的极端气温事件研究较少。利用全国591个站点1960—2010年逐日最高、最低气温数据，采用相对阈值法和Mann-Kendall非参数突变检验法和滑动 t 检验法，分析了中国极端高温（TX95p）和极端低温（TN05p）、异常高温（TX99p）和异常低温（TN01p）频数的时间变化趋势。研究得出：1960—2010年除了华中大部分地区及其周边区域极端高温和异常高温频数呈减少趋势外，其他地区极端高温和异常高温频数呈增加趋势，但不同区域的增加趋势不同；全国绝大多数站点极端低温和异常低温出现的频数呈减少趋势。极端低温突变时间点大都在80年代前后，极端高温突变时间在90年代和2000年前后；异常高温突变时间大都在80年代左右，异常低温突变时间大都在80年代和90年代前后。从近51年的频数变化趋势上看，极端低温、异常低温频数减少趋势的幅度大于极端高温、异常高温频数增加趋势的幅度，农业面临极端高温的风险呈增加趋势（图7）。（房世波）

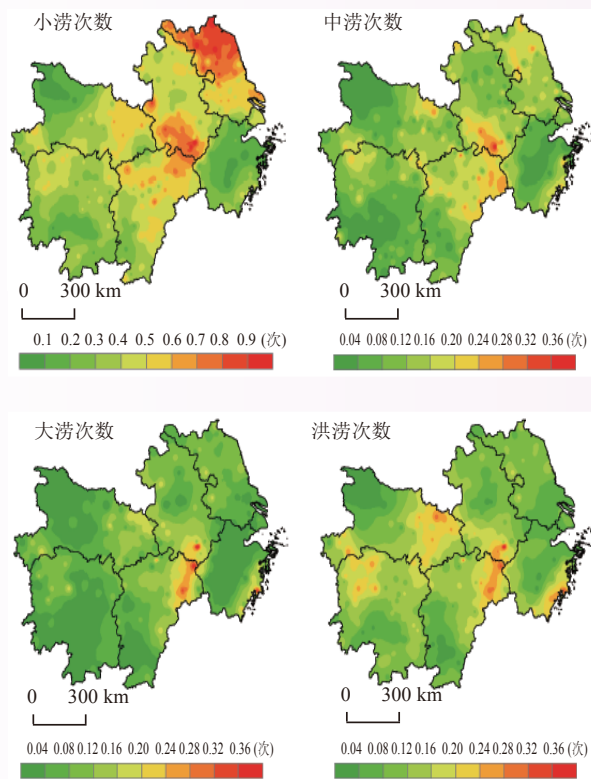


图1 1961—2010年长江中下游地区各等级农业洪涝次数、洪涝指数的平均分布

Fig.1 Average distribution of agricultural flood frequency and flood-index by grade in the middle and lower reaches of the Yangtze River from 1961 to 2010

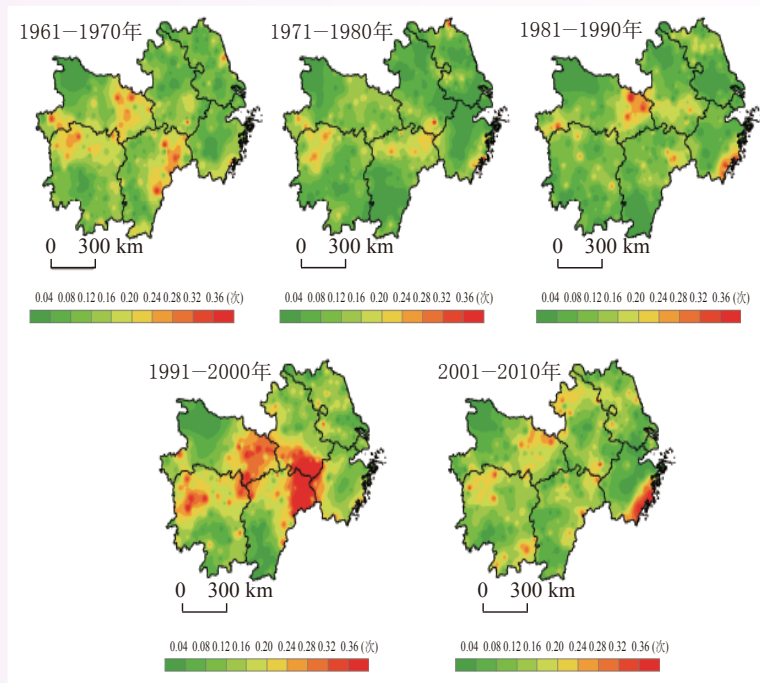


图 2 1961—2010年长江中下游地区洪涝指数的年代际分布

Fig. 2 Decadal distribution of flood-index in the middle and lower reaches of the Yangtze River from 1961 to 2010

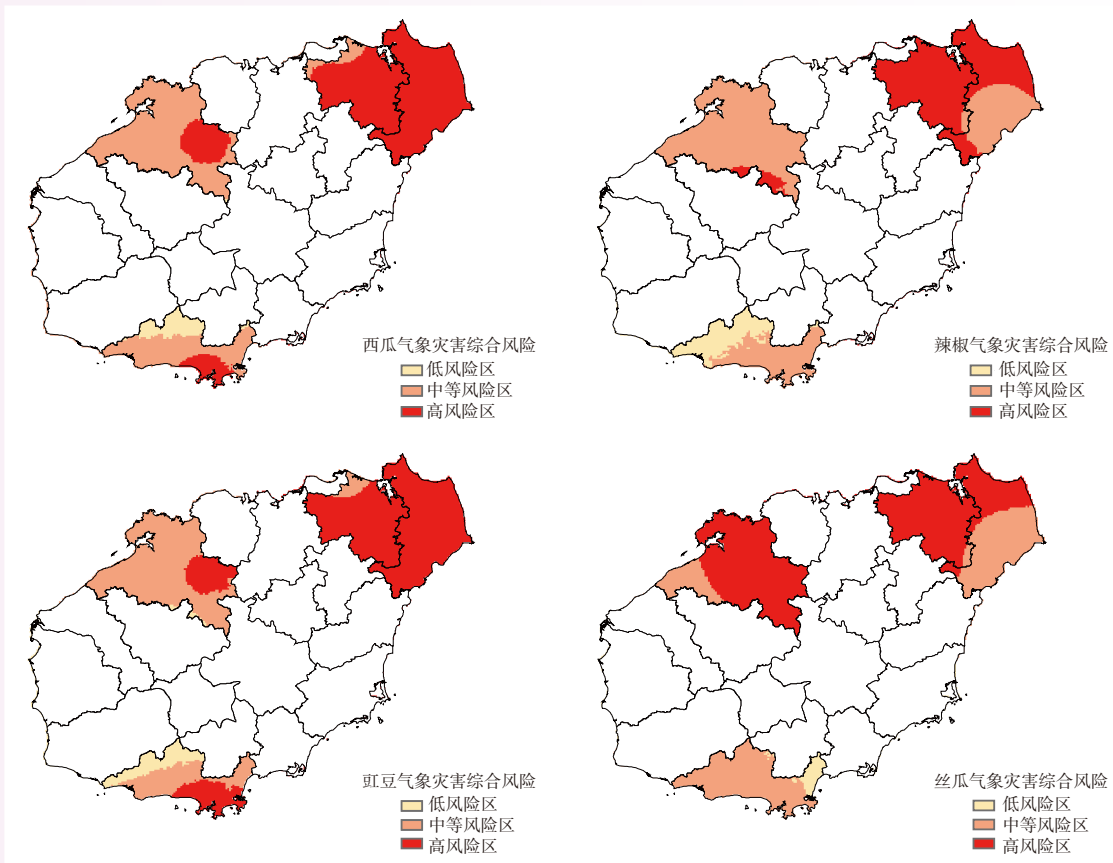


图 3 海南冬季瓜菜气象灾害综合风险区划

Fig. 3 Integrated risk mapping of winter melons and vegetables prone meteorological disasters in Hainan

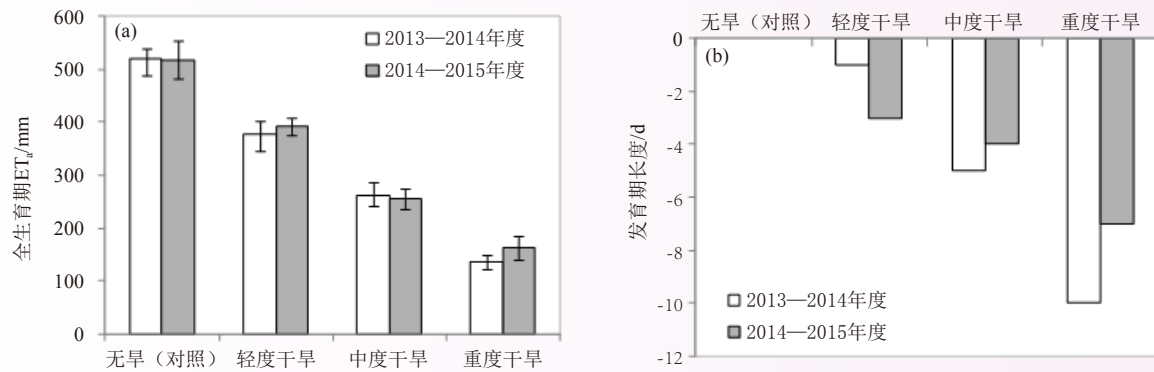


图 4 不同水分处理条件下冬小麦全生育期实际蒸散量(ET_a) (a)和发育期长度 (b)与对照的差异

Fig. 4 Differences of winter wheat in actual evapotranspiration (a) and growth length (b) as compared with CK under different soil water stresses

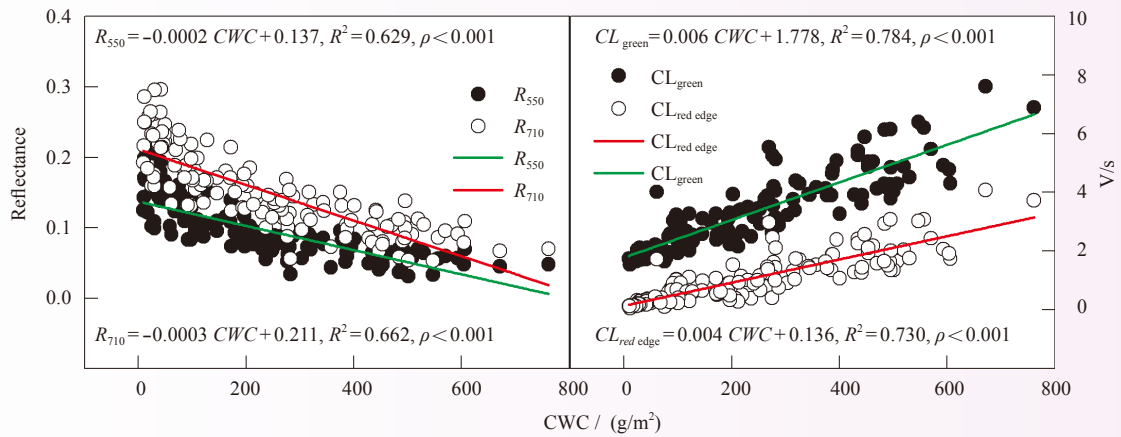


图 5 玉米冠层含水量(CWC)与冠层反射率(R_{550} 和 R_{710})和高光谱遥感植被指数 (CI_{green} 和 $CI_{red\ edge}$)间的相关关系

Fig. 5 Correlation between CWC and reflectance (R_{550} and R_{710}) and hyperspectral indices (CI_{green} and $CI_{red\ edge}$)

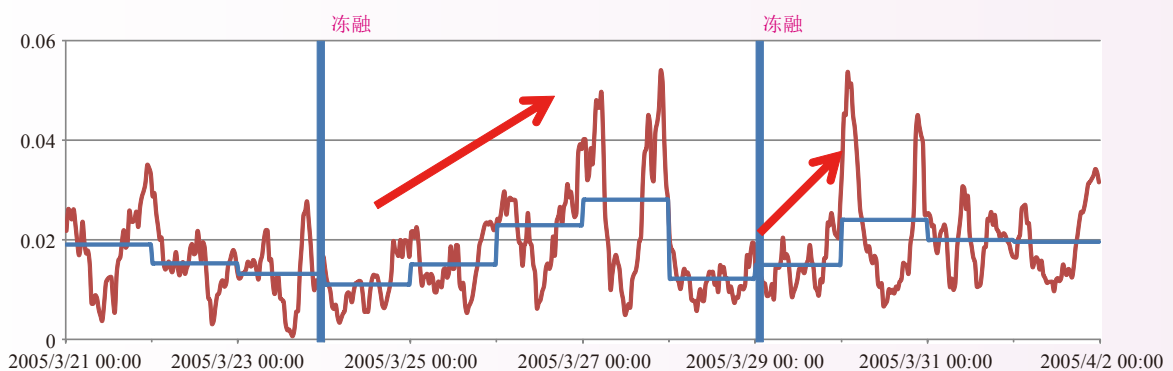


图 6 冻融前后的土壤CO₂排放速率

Fig. 6 Soil CO₂ emission during freeze-thaw cycles

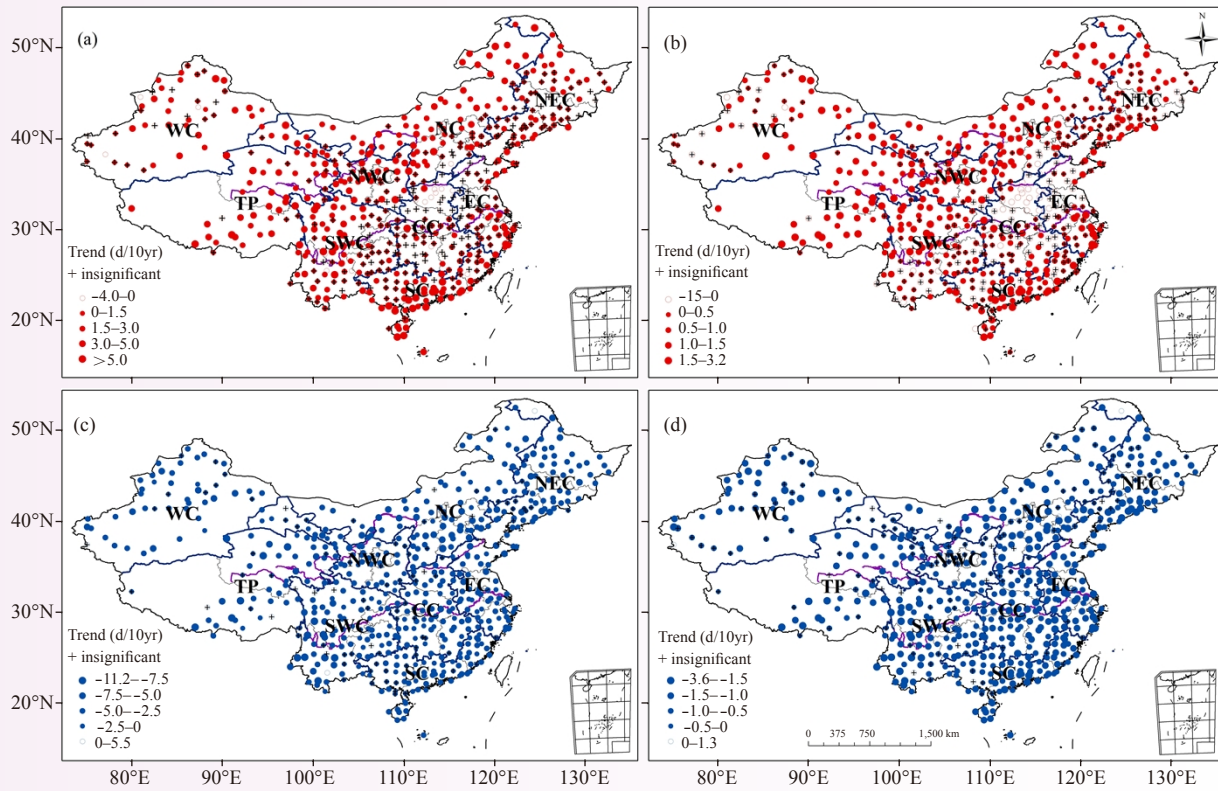


图 7 1960—2010年中国极端高温频次TX95p (a)、异常高温频次TX99p (b)、极端低温频次TN05p (c)和异常低温频次TN01p (d)的年际变化趋势 (d/10a)

Fig. 7 Spatial distribution of extreme temperature indices in China during 1960–2010: (a) Trends of TX95p; (b) Trends of TX99p; (c) Trends of TN05p; (d) Trends of TN01p. The black symbol ‘+’ shows the stations whose trends were insignificant at the significance level of 0.05. The unfilled symbol ‘.’ represents an increased frequency in TX95p and TX99p and a decreased frequency in TN05p and TN01p

Progress in Ecology and Agrometeorology Research

1 Agroclimatic resources and agrometeorological disasters forecasting and early warning

1.1 Techniques of the 3D monitoring and the dynamic assessment of key agrometeorological disasters

To study the 3D monitoring and the dynamic assessment of the dry-hot wind for winter wheat in Huanghuaihai areas, cold damage for double cropping rice in southern China and agricultural drought in Southwest China, we established meteorological indicators and a grading system for the above agrometeorological disasters, and developed the 3D monitoring and the dynamic assessment techniques which are based on ground observation, remote sensing and crop models and are applied to meteorological operation. The key monitoring and assessment techniques, which are totally tailored to Chinese agricultural production and disasters, are highly regional and practical, taking into account the operational and service needs of the meteorological and agricultural sectors. The implementation of the research findings can significantly improve the monitoring and assessment of agrometeorological disasters in China. (Zhao Yanxia)

1.2 Highly-resolved winter wheat soil moisture and irrigation forecasting systems at provincial level

Based on the study of remote sensing inversion of evapotranspiration deficit indices, using the manually and automatically observed soil moisture data together with neural networks, the initial soil moisture fields of high resolution and reliability were obtained. The estimated a and b coefficients were tested and compared with the recommended values of FAO ($a = 0.25$, $b = 0.5$). The results show that the mean square root error of each month with the estimated a and b coefficients in most stations is smaller than that of FAO. The winter wheat maximum root length model was structured. The a and b coefficients, crop coefficient, evapotranspiration coefficient of soil stratification, soil water stress coefficient for winter wheat areas in northern China were established. Three provincial highly-resolved soil moisture and irrigation forecasting systems for winter wheat were improved to be as accurate as more than 80%, which were operationally piloted, regionally verified and quasi-operationally applied in 2015. (Mao Fei)

1.3 Technique on low temperature warning for cropping rice in southern China

Based on the low temperature disaster trend and the geographical partition of risk for double cropping rice in southern China in nearly 50 years, the grade-based low temperature disaster prediction for double cropping rice has been introduced, in which the models of the next 10 days early-season rice and the next 5 days late-season rice were developed respectively. The mapping of double cropping rice region I (high risk), region II (increasing risk), region III (low and reducing risk) is applicable to japonica and indica, where the low temperature forecasting models for double cropping rice were built based on atmospheric circulation characteristics, the average accuracy of which is above 83%. Based on the models for the next 10 days early-season rice and the next 5 days late-season rice as discriminated by Fisher's analysis, the average extension accuracy is above 80%. The technique, which is a good combination of the occurrence trend, the geographical partition of risk and the grade warning for a low temperature event, enhances regional relevance of early warning for double cropping rice. (Huo Zhiguo)

1.4 Model for integrated risk assessment of agricultural floods in southern China

Grade-based agricultural flood indicators for 11 provinces in the middle and lower reaches of the Yangtze River and Southwest China were constructed in this study. Flood indexes were developed, with their agreement with the actual flood severity analyzed based on 101–151 flood indicators derived from single station process precipitation thresholds as prototype indicators. A severity-based inverse process analysis method was developed, including the grade-based indicators for single season rice flood in Southwest China, early rice flood in Hunan Province, and summer maize waterlogging in Jianghuai region. The spatial and temporal distribution of regional agriculture, rice flooding, summer maize waterlogging was mapped. Based on such relative severity indicators as the affected acreage, the affected population and the proportion of direct economic losses, a composite index of relative severity and its risk estimation model were developed for southern China to reflect discrepancy in damage in 12 provinces every year. This model, which also addresses such key technical problems as the precipitation process based agriculture, rice flood, determination of grade threshold for summer maize waterlogging and comparability of indicators by province, provides index-based support to the real-time disaster monitoring, warning and assessment (Fig.1–2). (Huo Zhiguo)

1.5 Integrated risk regionalization of meteorological disasters to winter melon and vegetables in Hainan

The grade based evaluation indicators were constructed based on waterlogging indexes of winter melon and vegetables (watermelon, pepper, bean, towel gourd) prone wet/logging disaster at seedling stage in Hainan, based on process chilling injury of winter vegetable prone winter chilling disaster, and drought indexes of melon and vegetable prone drought disaster in spring and winter. The comprehensive risk zoning maps were established to address comprehensive vegetable prone meteorological disasters, an instrument that covers disaster risk factors, disaster pregnant environment sensitivity, disaster bearing vulnerability and capacity of disaster prevention and mitigation. Key technical problems on hazard construction and quantification and multi-hazard weighting determination were solved as a contribution to the development of the indexes in this connection (Fig.3). (Huo Zhiguo)

1.6 The mechanism underlying the physiological responses of summer maize to drought

The effects of water stress on leaf chlorophyll content and photosynthetic capacity parameters were examined generally for summer maize exposed to different drought treatments. The results show that both moderate steady drought and severe steady drought led to significant declines in relative chlorophyll content (SPAD value). However, during the late grain-filling period, moderate steady drought did not decrease the SPAD, instead even slightly increased it, while the severe steady drought always caused reductions. It possibly indicates the adaptability of maize leaves to drought: the adaptive response appears as the plant is subjected to moderate drought, but disappears as to enough severe drought. The net light-saturated photosynthetic rate (A_{sat}) decreased under the two steady and the two continued drought treatments, indicating the inhibition of net carbon fixation rate in the maize leaves. The actual photochemical efficiency of photosystem II (PSII) in light-adapted leaves did not decrease at the early stage of the drought treatment, indicating the adaptive response to a certain degree. However, under the severe drought condition, the adaptive response may disappear. (Zhou Li)

1.7 The water consumption of winter wheat and summer maize in rotation in Huanghuaihai Plain

Water consumption by winter wheat and summer maize from 2011 to 2012 in Huanghuaihai Plain was estimated with integrated remote sensing, meteorological data, field information and ground truth. Afterwards, tempo-spatial characteristics of crop water consumption and its structure were studied. Precipitation accounted

for 97.21% of summer maize water consumption in 2011. Irrigation in southern part of Hebei Province and mid and northern parts of Henan Province in summer maize growing season accounted for approximately 10% of the total summer maize water consumption. Irrigation accounted for 73.3% of total winter wheat water consumption. Irrigation was identified as the dominate water source in Hebei and Henan provinces, with irrigation accounting for more than 80% of the winter wheat water consumption from 2011 to 2012. (Yang Jianying)

1.8 The impact of different water stresses on winter wheat growth and development

Field experiments of soil water stresses during two growth-year of winter wheat (2013–2014 and 2014–2015) were carried out at Gucheng station. The impacts of different soil water stresses on the growth condition of winter wheat were studied. The results show that the regression coefficients of structural parameters (planting density and height) and functional parameters (leaf area index and biomass) with CK corresponded to the water supplies in number. Generally, the regression coefficient was minimum under the severe drought, maximum under slight drought, and medium under moderate drought, which showed the impacts of drought on the growth condition of winter wheat. Meanwhile, the actual evapotranspiration and growth length of winter wheat during the whole growth period under different soil water stresses were also different. With the severity of drought, the actual evapotranspiration showed an obvious decrease, and the growth length was shorter due to the forced maturity caused by drought (Fig. 4). (Wang Peijuan)

1.9 The crop coefficients of winter wheat in North China

The crop coefficients (K_c) of winter wheat was calculated as the ratio of daily actual evapotranspiration (ET_a) and reference evapotranspiration (ET_0) during the entire phenological period at Gucheng station. ET_0 was estimated using daily meteorological data based on the FAO Penman-Monteith method, while ET_a was collected from the processed eddy covariance data. The K_c of winter wheat exhibited the bimodal feature at both ten-day and phenological scales, which indicates the distinct physiological characteristics of overwintering crops. Compared with the conventional FAO-56 method, the proposed stage-wise K_c of winter wheat captured the water requirement in different phenological stages in detail. Meanwhile, the accuracy of K_c using the proposed stage-wise method and the FAO method was evaluated by validating their respective estimation of ET_a . The validation against latent heat flux measurements shows that the stage-wise method outperformed the FAO method at both daily and phenological scales. The linear regression coefficients by the stage-wise method were 1.150 at daily scale and 1.243 at phenological stage scale respectively, both of which were closer to the unity than those by the FAO method. (Wang Peijuan)

1.10 Drought-sensitive indicators and thresholds of summer maize in the seeding stage

The drought-sensitive indicators of summer maize in the seeding stage include stem moisture content (SMC), leaf moisture content (LMC), transpiration rate (Tr), net photosynthetic rate (Pn), stomatal conductance (Gs), and leaf area index (LAI). The soil water thresholds of SMC, LMC, Tr, Pn, Gs and LAI in terms of relative soil water content at the depth of 0–30 cm (RSH) are 74.7%, 65.6%, 62.0%, 61.5%, 59.1% and 46.8% respectively. They reflect the sensitivity of the drought-sensitive indicators of summer maize in the seeding stage. Based on the energy balance equation on the soil and the water deficit index (WDI), together with the hypothesis that WDI depends linearly on soil relative humidity, the soil moisture is estimated in terms of the remote sensing data (the normalized difference vegetation index (NDVI) and surface temperature (T_s)) and the ground observation (air temperature T_a). The model is validated based on the data from the drought process experiment on summer maize (*Zea mays* L.) in response to different irrigation treatments carried out during 2014 at Gucheng Eco-agrometeorological experimental station (39°08'N, 115°40'E) of China

Meteorological Administration. The estimation accuracy of 0–10 cm surface soil moisture is the highest ($R^2 = 0.90$). The correlation of the estimated and measured soil relative humidity in deeper soil layers (up to 50 cm) passes the significance test at the level of 0.0001 with the RMAEs less than 15% and the PRMSEs less than 20%. The Cl_{green} (green chlorophyll index) is found to be most sensitive to canopy water content (CWC) of summer maize. Thus, the universal hyperspectral RS (remote sensing)-based CWC model is constructed for the wide variation of CWC in terms of Cl_{green} (Fig. 5). (Zhou Guangsheng)

2 Response and adaptation of agriculture to climate change

2.1 The adaptability of maize varieties in Huanghuaihai region to climate change

The outputs of RegCM4 under RCP4.5 and RCP8.5 scenarios and APSIM model were used to assess the negative effects of climate warming on maize yield. Meanwhile, final maize yield is strongly associated with grain number, which is very sensitive to high temperature especially in the period of flowering. Introducing a variety with improved high-temperature tolerance of grains might be an efficient strategy to adapt to climate warming. Therefore, we assumed a heat tolerant variety that has a maximum grain number development temperature tolerance of 40 °C rather than 38 °C for a similar current variety. The results indicate that by using heat tolerant variety, maize yield could increase averagely by 4%. (Zhao Yanxia, Zhan Yi)

2.2 The impact mechanism of increases in atmospheric CO₂ concentration and air temperature on change in crop water requirement

After exploratory efforts in the past three years by field and laboratory experiments, the impact mechanism and its pathway on change in wheat water requirement were almost ascertained. That is to say that, firstly, the elevated air temperature increased the wheat water requirement in each day, and then increased the wheat water requirement in whole growth seasons, but it shortened the wheat growth period from sowing to maturing. Therefore, the wheat water requirement was balanced by the increased water requirement in each day and shortened growth days. Secondly, the elevated atmospheric CO₂ concentration increased the wheat dry matter and the water contents in leaves especially in flag leaves. In addition, the elevated atmospheric CO₂ concentration tended to prolong the wheat growth period especially during milk period. Finally, the elevated atmospheric CO₂ concentration increased the wheat water requirement. Our experiment results show that the wheat water requirement increased 12% in each day and increased 10%–15% averagely in growth period when air temperature was elevated by 1 °C. The doubled atmospheric CO₂ concentration increased wheat water requirement averagely by 25.6% during growth period. However, the combined impact of increases in atmospheric CO₂ concentration and air temperature on change in wheat water requirement, which is not yet to be determined, needs further exploration. (E Youhao)

2.3 Soil CO₂ emission from wetland during freeze-thaw cycles

Using the eddy covariance method, measurements of CO₂ emission were made over paddy rice and reed marsh ecosystems in the Liaohe Delta. The results show that the amount of soil CO₂ emission from paddy rice and reed marsh during the freeze-thaw period on an annual basis contributes to annual CO₂ emissions by 14.1% and 12.5% respectively. This amount is not to be ignored in the assessment of ecosystem carbon budget. The increment of soil CO₂ emission from paddy rice and reed marsh, resulting from the freeze-thaw cycle, contributes to annual CO₂ emissions by 4.01% and 4.46% respectively. And this increment is positively correlated with the soil temperature (5–10 cm) ($R^2 = 0.57$) (Fig. 6). (Zhou Li)

2.4 Correlation between major crops and meteorological factors in the one ripe areas in northern China

The growth and yield formation of spring wheat and spring maize based on APSIM model were simulated. The validated APSIM model had better adaptability in Inner Mongolia. There was a good correlation between the measured data of spring wheat and spring maize and the simulation results from APSIM model in Inner Mongolia. The DOY (day of the year) of flowering of spring wheat was very significantly correlated with average temperature, and was significantly correlated with soil temperature. However, it was not correlated with precipitation, solar radiation or potential evapotranspiration. As for the DOY of maturity, it was very significantly correlated with average temperature and soil temperature. And it was significantly correlated with potential evapotranspiration. However, it was not correlated with precipitation or solar radiation. The DOY of flowering of spring maize was not related to meteorological factors. The DOY of maturity of spring maize was strongly related to average temperature, wind and soil temperature. At the same time, the DOY of maturity of spring maize was significantly correlated with relative humidity. However, it was irrelevant to the precipitation, solar radiation or potential evapotranspiration. (Zhao Junfang)

2.5 The uncertainty of the impact of climate change on maize yield in Northeast China

This work analyzed the uncertainties in maize yield predictions using three climate projections to represent the climate output uncertainty, and two different crop models to represent the structural uncertainty, taking the Zhuanghe agrometeorological station as an example. The multi-model ensemble simulation indicated a yield reduction of 13% with 80% probability during 2021–2050 relative to 1971–2000. The variance based decomposition of the yield projection shows that climate change uncertainty generally has a larger impact on projection than the crop model uncertainty does. Downscaled climate projections have a significant bias that can introduce significant uncertainties in yield projections. Furthermore, we employed 24 climate projections consisting of the combinations of 8 GCMs and 3 emission scenarios representing the climate output uncertainty, and 2 crop statistical models with 100 sets of parameters in each model representing parameter uncertainty within the crop models, to evaluate the impact of climate change on maize yield at three locations (Benxi, Changling, and Hailun). The multi-model ensemble simulation shows that the maize yield reduction will be less than 5% in future climate periods relative to the baseline. The variance based decomposition indicates that the uncertainty from climate projections was much larger than that contributed by crop model parameters. (Zhang Yi)

2.6 The synergistic impacts of elevated temperature and enriched CO₂ concentration on winter wheat

An experiment under winter wheat was conducted using the combined technologies of open top chamber (OTC) and infrared radiator heaters at the Gucheng Ecological and Agro-meteorological Experimental Station of the Chinese Academy of Meteorological Sciences in 2015, in which the level of CO₂ concentration in treatment chambers was maintained at $(603 \pm 55) \times 10^{-6}$, while the temperature increases in treatment chambers compared to control were manipulated at $1.6 \pm 0.6^{\circ}\text{C}$ and $3.9 \pm 0.5^{\circ}\text{C}$ in day and night respectively. Results indicate that CO₂ concentration of 600×10^{-6} fails to compensate the adverse effects of an average daily temperature increase of 2.8°C on the growth of winter wheat. With a daily temperature increase of 2.8°C during the entire growing period of winter wheat in North China, the crop developmental stage after over-wintering is advanced significantly compared to that under the ambient conditions, which causes both daily mean temperature and the amount of solar radiation to decrease significantly during the post-winter period, increasing the risk of frost damage and low temperature stress at late growth stages. (Tan Kaiyan)

2.7 The nonlinear response of winter wheat phenology to climate warming

The relationship between wheat phenology and early temperature in China was firstly analyzed by using

the phenological and meteorological observation data. The results show that sowing, emergence and tillering stages of spring wheat are in a nonlinear relation with the early temperature, which begins to be linear from the jointing stage. However, winter wheat is just the opposite. The differences between the different regions were then investigated to show that the mature stage of spring wheat changes with temperature in a concave curve in Shanxi, Gansu, Ningxia and Xinjiang while the relation is linear in other regions. The response of the duration of different developmental stages of wheat to the early average temperature was finally discussed. The duration of emergence to milk and to maturity of spring wheat linearly decreases along with the rising early temperature. The duration of tillering, stopping growth and turning green from emergence stage is linearly correlated with the early average temperature while the duration of jointing, heading, milk and maturity from emergence stage is correlated with the early average temperature in a convex curve. (Ma Yuping)

2.8 Impacts of climate change on agroclimatic resources in northeast region

The temporal and spatial trends of the main climatic elements and agroclimatic resources were analyzed by using the data of 91 weather stations in northeast region (Heilongjiang, Jilin, Liaoning, Four Leagues in Inner Mongolia) from 1961 to 2010 and regional climate model simulations from 1951 to 2099. Under climate change, the changing climatic resources in northeast region from 2010 to 2099 are significant. The temperature will rise and the rainfall will slightly reduce. The warming and drying climate will have some impacts on agricultural production. Climate change will result in more agricultural heat resources in northeast region, as indicated by the advance of the early date of $\geq 10\text{ }^{\circ}\text{C}$, the delay of the first frost date, and the possible growth period extension. The increment of accumulated temperature will expand the available planting space, so that the late-maturing crop varieties can be planted more widely, and the areas where crops are not grown be reduced. For example, the minimum accumulated temperature of spring corn in northeast is $2100\text{ }^{\circ}\text{C}\cdot\text{d}$. The areas where spring maize is not planted in Heilongjiang Province from 1950s to 2090s will be reduced to Mohe. But the reduced precipitation may cause adverse effects on agricultural production. (Guo Jianping)

2.9 Changing and abrupt extreme temperature in mainland China from 1960 to 2010

Studies based on the 10th (90th) percentiles as thresholds have been made to assess moderate extremes in China and the globe. However, there has been notably little research on the occurrences of high extremes of warm days (TX95p and TX99p) and cold nights (TN05p and TN01p) based on the 95th or 99th (5th or 1st) percentiles, which have more direct impacts on the society and the ecosystem. The study demonstrate that (1) the frequencies of TX95p and TX99p increased, on average, by 1.80 d/10yr and 0.62 d/10yr, respectively, at all stations in mainland China. The TX95p and TX99p increased significantly in 50.42% and 58.21% of the stations, while the TN05p and TN01p decreased significantly in 83.76% and 76.48% of the stations, respectively. The frequencies of TN05p and TN01p decreased, on average, by 3.18 d/10yr and 1.01 d/10yr, respectively, at all stations. (2) All regions of China, except for Central China, exhibited an increasing trend in TX95p and TX99p, but the vast majority of mainland China showed a decreasing trend in TN05p and TN01p. (3) The TX95p and TX99p trends transformed in the 1990s or 2000s, but the trends of TN05p and TN01p underwent an abrupt change in the late 1970s and early 1980s. After the abrupt change, the trend of warm and hot days increased more rapidly than before in most regions, which indicates the greater risk of heatwaves in the future, while the trend of cold and freezing nights is not as large as before (Fig. 7). (Fang Shibo)

大气成分与大气化学 Atmospheric Composition and Atmosphere Chemistry

大气成分和大气化学研究进展

1 大气成分及相关特性变化的观测研究

1.1 中国地区地基气溶胶光学-辐射特性的时空分布与变化

详细研究了中国地区地基的、高精度、覆盖广泛的月均气溶胶光学厚度 (AOD) 分布及近十年来的年际变化。研究发现: 中国地区气溶胶 AOD 高值区主要分布在人为活动密集的中东部地区, 年均值 >0.60 ; 气溶胶粒径大小“自北向南”依次降低, 与北方受沙尘气溶胶而南方受二次气溶胶影响有关。远源地区气溶胶载荷略低于全球平均; 在沙尘源区和黄土高原气溶胶为全球平均的 $1.7 \sim 2.1$ 倍, 而在中国东部郊区及城市区域气溶胶为全球平均的 $2.7 \sim 3.7$ 倍。中国地区 AOD 自 2009 年来呈显著增加态势, 主要原因可能与环境气象条件的改变有关。(车慧正)

1.2 大气中气态污染物在矿物气溶胶表面耦合相互作用的实验室模拟

矿物气溶胶表面非均相反应由于可以改变气溶胶理化性质以及大气痕量气体平衡而成为大气化学的研究热点。然而目前关于痕量气体在矿物气溶胶表面的共同吸附研究却很有限。本研究中采用原位漫反射红外光谱研究了大气中 SO_2 和 HCOOH 在 CaO 表面的耦合相互作用。通过分析红外光谱以及获取动力学曲线发现, SO_2 和 HCOOH 在 CaO 颗粒物表面非均相反应相互抑制, 同时通入 2 种气体时表面产物甲酸盐和亚硫酸盐都减少。通过分步实验发现, SO_2 和 HCOOH 在 CaO 表面的耦合相互作用主要分为 2 个方面。 SO_2 共同存在时可供吸附的反应活性位点变少从而抑制 HCOOH 在颗粒物表面反应, 导致产物甲酸盐生成量减少。另一方面对于 SO_2 在 CaO 表面的非均相反应而言, HCOOH 会阻止 SO_2 在颗粒物表面的非均相反应, 使得表面生成亚硫酸盐减少。(吴玲燕)

1.3 瓦里关全球本底站地面臭氧变化特征与变化趋势

臭氧本底浓度的长期变化趋势信息对于环境与气候变化的评估至关重要。然而, 目前已有的本底站地面臭氧长期观测数据与趋势分析结果多数来源于欧洲与北美地区, 在我国和其他发展中国家仍缺乏类似的研究。本文分析了瓦里关全球大气观测本底站过去 20 年 (1994—2013 年) 的地面臭氧观测数据, 探讨了其日变化与季节变化规律、长期变化趋势和时间变化的周期性。为了得到可靠的长期趋势结果, 分别采用线性回归、季节性 Mann-Kendall 趋势检验和 Hilbert-Huang Transform (HHT) 分析对数据进行了趋势分析。结果显示, 山谷风对瓦里关地面臭氧的日变化起着决定性作用, 导致臭氧白天低夜间高。地面水平风向与垂直风向具有显著的随季节变化的日变化规律, 该特征被用于定义随季节变化的白天与夜间时段。地面臭氧无论在白天 ($(2.4 \pm 1.6) \times 10^{-9}/10\text{a}$) 还是夜间 ($(2.8 \pm 1.7) \times 10^{-9}/10\text{a}$) 都出现显著增长趋势。最大夜间增长率出现在秋季 ($(2.9 \pm 1.1) \times 10^{-9}/10\text{a}$), 春季其次 ($(2.4 \pm 1.2) \times 10^{-9}/10\text{a}$), 而夏季 ($(2.2 \pm 2.0) \times 10^{-9}/10\text{a}$) 和冬季 ($(1.3 \pm 1.0) \times 10^{-9}/10\text{a}$) 则增长略慢。HHT 波谱分析得到了 4 个具有不同臭氧增长速率的阶段, 最快的增长出现在 2000 年 5 月和 2010 年 10 月。此外, HHT 分析结果指示出瓦里关的地面臭氧时间序列中存在 2~4 年、7 年与 11 年的周期。(徐婉筠)

1.4 含铝矿物气溶胶对间二甲苯/ NO_x 光氧化体系中SOA生成的影响

间二甲苯是人为源VOC中具有较高SOA生成潜势的VOC物种。本研究采用烟雾箱模拟试验研究了含铝矿物气溶胶(拟薄水铝石和氧化铝)对间二甲苯/ NO_x 光反应体系中SOA生成过程的影响。研究发现,在30℃、50%相对湿度条件下,含铝气溶胶的存在将导致SOA产率的提高以及体系中 O_3 浓度的增加。 O_3 的光解是OH自由基的重要来源,而OH自由基是间二甲苯氧化的重要氧化剂,其浓度的提高将有助于SOA产率的增长。此外,含铝气溶胶可影响光氧化产物的凝结过程进而影响到SOA的最终粒径。当低浓度含铝气溶胶存在时,SVOC_s将优先凝结在气溶胶颗粒表面,从而导致粒径的增长。当高浓度含铝气溶胶存在时,凝结在每个种子颗粒表面的SVOC_s量减少,从而导致最终SOA粒径的减小。(刘畅)

1.5 我国PM₁₀、PM_{2.5}和PM₁的时空变化特征

利用我国24个站点2006—2014年的颗粒物浓度观测数据,分析了我国PM₁₀、PM_{2.5}和PM₁的时空变化特征。颗粒物浓度最高的站点是华北地区的郑州、固城和关中平原的西安,在郑州PM₁₀、PM_{2.5}和PM₁的平均浓度分别为131.7、84.8和71.0 μg/m³,其次是中国的东北和华南地区。达到我国PM₁₀和PM_{2.5}空气质量的站点分别仅有14个和7个,且主要是偏远地区的站点。由于我国北方地区粗颗粒的矿物气溶胶组分多,PM_{2.5}在PM₁₀中所占的比例从北方至南方呈现明显上升趋势。在接近沙尘暴源区的站点比例小于50%,而在长江流域地区该比例为80%~90%。PM₁在PM_{2.5}中所占的比例在大多数站点都超过了80%。多数站点颗粒物浓度冬季最高、夏季最低,春季受沙尘气溶胶影响明显。华北地区PM_{2.5}浓度呈下降趋势,西安在2011年到达峰值,其后下降趋势明显;东北地区部分站点有上升趋势;长江中下游站点的长期变化趋势不显著,华南地区总体呈下降趋势。大部分站点2014年平均浓度较2013年显著下降,可能显示了2013年9月“大气污染防治行动计划”出台后的减排效果。气象因素对短期内日变化的影响明显,风速和浓度负相关,相对湿度和浓度正相关(降水例外)。气象因素和排放因素都对颗粒物浓度长期(年度)变化有重要影响(图1)。(王亚强)

1.6 北京上甸子大气本底站CO₂浓度的源汇区域代表性研究

为研究单个站点CO₂观测浓度的源汇区域代表性及所在区域的CO₂通量特征,利用大气反转模式FLEXPART模拟确定影响上甸子站观测浓度的气团主要来源,利用Carbon Tracker模式反演CO₂浓度和通量的时空分布,并通过数值迭代方法和相关性分析方法获取最优印痕函数阈值,得到影响测站CO₂浓度的源汇区域范围。其次,将在线观测CO₂浓度筛分为本底和非本底浓度,利用FLEXPART模式追踪测站本底和非本底源区,研究发现,本底和非本底源汇区域明显不同并随季节变化。在印痕函数大于一定阈值的潜在源区内,本底和非本底区域净通量变化趋势差异明显,而且在各通量分支中本底区域化石燃料通量较小、生物圈通量较大,非本底区域化石燃料通量较大、生物圈通量较小。通过反演模式能够定量得到影响测站观测浓度的源汇区域及区域通量特征。(程已阳)

1.7 北京市夏季大气过氧乙酰基硝酸酯(PAN)的污染水平、变化特征及源汇研究

大气过氧乙酰基硝酸酯(PAN)是大气中光化学污染重要的指示剂,在大气化学中具有重要的作用且对人体和植物产生负面影响。本研究采用GC-ECD方法对北京市夏季大气PAN和同系物过氧丙酰基硝酸酯(PPN)开展连续观测研究,发现PAN和PPN的平均浓度水平为 $(2.61 \pm 2.57) \times 10^{-9}$ 和 $(0.52 \pm 0.38) \times 10^{-9}$,最大值高达 12.50×10^{-9} 和 2.16×10^{-9} 。两者均具有明显的日变化特征且有较好的正相关关系($R=0.85$, $p < 0.01$)。基于近似稳态方程方法,对大气PAN的二代前体物含氧挥发性有机物(OVOC_s)如乙醛、丙酮、丁二酮、甲基乙烯酮(MVK)、甲基丙烯醛(MACR)以及甲基丙醛酮(MGLY)光化学生成潜势进行了估算,研究发现,乙醛对2010年夏季PAN的贡献最大,

约59.7%，丙酮次之（图2~3）。（张根）

1.8 青藏高原偏远站点当雄地面臭氧2年观测结果

本研究于2009年9月至2011年8月在地处青藏高原念青唐古拉山南部河谷地带的当雄站（30.48°N, 91.10°E, 海拔4187 m）开展了地面臭氧（O₃）和一氧化碳（CO）的观测。结果表明，O₃平均混合比为 38.5×10^{-9} ，月均值介于 $29.1 \times 10^{-9} \sim 51.4 \times 10^{-9}$ ，峰值出现于5月。O₃日变化形式表现为，最低值和最高值分别出现于清晨和下午，近中午至近傍晚期间出现高值平台，基本与地面风速的日变化相似。地面O₃混合比与当雄及周边对流层O₃柱含量显著相关，也与念青唐古拉山北侧观测的地面O₃变化趋势接近，表明当雄地面O₃观测值有较好的区域代表性。下午时段风速增强时地表空气呈高O₃、低CO和低相对湿度（RH）的自由大气特征。多数月份存在O₃-CO和O₃-RH负相关关系，表明自由对流层影响显著。轨迹分析表明，站点以南的气团含较低O₃和较高的CO和湿度，来自西部扇区的气团则相反（图4）。（徐晓斌）

1.9 华北平原夜间对流天气对地面O₃混合比抬升效应

2013年6—9月，在河北农村固城站观测到多次夜间对流性天气过程伴随地面O₃混合比快速抬升的过程，并引起次日清晨到中午O₃混合比升高。大多数对流过程中，O₃混合比在半小时内升高至 $60 \times 10^{-9} \sim 80 \times 10^{-9}$ ，同时NO_x等反应性气体混合比下降， θ_{se} 值降低，说明下沉气流将高空气团带到地面，造成了O₃混合比的升高。通过再分析资料得到下沉气团基本来源于对流层中下层，这一结论与当地进行的一次飞机观测结果吻合。多数对流过程中固城站和北京城区地面O₃混合比和 θ_{se} 值有相同的变化趋势和程度。根据观测结果，推测华北地区在夏季和初秋时对流层中下层存在O₃高值区，混合比为 $60 \times 10^{-9} \sim 80 \times 10^{-9}$ 。对流性天气对地面O₃抬升的影响区域与对流系统的影响范围有关，可达到中尺度范围。华北地区光化学污染严重，对流性天气引起的地面O₃混合比抬升程度比较强，其对环境的影响值得关注。（徐晓斌）

1.10 2013年夏季华北乡村站点固城大气氨变化特征

利用2013年6—8月河北省定兴县固城站的NH₃连续高时间分辨率观测数据，分析了NH₃体积分数水平、变化特征和影响因素。2013年夏季固城NH₃小时平均体积分数变化范围是 $(0.9 \sim 862.9) \times 10^{-9}$ ，平均体积分数为 $(43.9 \pm 65.9) \times 10^{-9}$ 。观测期间PM_{2.5}中NH₄⁺平均质量浓度为 $19.77 \pm 33.24 \text{ g/m}^3$ 。2013年夏季固城NH₃和NH₄⁺质量浓度之间有良好的相关性，且浓度明显高于华北地区城市站点，说明由于农业施肥等活动的影响导致固城大气NH₃和NH₄⁺质量浓度水平显著提高。NH₃体积分数在夏季有明显的日变化且呈现出单峰的特征。2013年夏季固城硫氧化率（SOR）和氨转化率（NHR）较高，说明SO₂和NH₃分别转化为SO₄²⁻和NH₄⁺的速率较大。华北地区应加大对由农业活动造成的NH₃排放的控制力度，以降低区域二次气溶胶污染。（孟昭阳）

1.11 长三角地区雾-霾期间亚微米气溶胶特性及其对能见度的影响

2013年1月严重雾-霾期间，在长三角地区临安大气本底站开展了气溶胶粒径、化学组分和光学特性的观测。结果表明，雾-霾期间颗粒物数谱分布的峰值出现在80~100 nm。PM₁质量浓度占PM₁₀约84%。根据相对湿度和能见度，将天气类型分为雾、霾和晴天，并且利用Mie模型估算了在不同类型天气条件下PM₁和PM₁₀在干状态下的光学性质。在晴天的情况下，PM₁对环境大气消光贡献约85%，在霾的条件下，贡献约为58%，在雾的条件下，贡献约为41%。干状态下PM₁对大气消光贡献的变化取决于不同的相对湿度。以1月14—17日的重雾-霾日为例，在颗粒物不断累积导致雾-霾发生的时段中，气溶胶化学组分主要以硝酸盐和有机物为主，与大气中的二次气溶胶生成和

气团区域输送有关。该研究也发现在长三角地区雾-霾情况下,硝酸盐比硫酸盐的贡献大,这一点不同于华北地区,主要是和2个地区不同的产业结构有关。(沈小静)

1.12 利用多源卫星气溶胶云数据首次发现的中国东部地区明显的气溶胶第1间接效应

气溶胶间接效应存在一个临界(饱和)值,在AOD达0.4~0.5之间。重度污染情况下(AOD>0.5),中国东部陆地上空云的CDR随AOD变化的规律变得离散,可能是气溶胶粒子过饱和反应的综合。为了一定程度消除气象条件影响,分别计算了夏季和冬季的ACI。在夏季,重度污染情况(AOD>0.5)混合状态下CDR随着AOD增加而增大的趋势非常明显,其中一个可能的解释是在气溶胶粒子过饱和后,对流和上升运动条件下,气溶胶粒子的进一步增加会使得云滴之间开始争夺水汽,并最终导致云滴变大。冬季,重度污染(AOD>0.5)混合状态下,CDR随AOD增加而增大的趋势不显著,这与冬季大气静稳缺少上升运动有关,气溶胶粒子过饱和后,云滴可能随着气溶胶粒子的继续增加而减小、增大或者不变。达到过饱和之后出现的与气溶胶第1间接效应相反的结果,可能与夏季的气象条件适宜于云滴增大的天气条件有一定的关系。而这一部分研究仍需要进一步的试验来证明。其中一个可能的解释是,气溶胶粒子过饱和后,在对流和上升运动条件下,气溶胶粒子的进一步增加会使得云滴之间开始争夺水汽,并最终导致大云滴越大,小云滴被蒸发。(郭建平)

1.13 全球沙尘和烟尘气溶胶在垂直方向概率分布规律

在气溶胶-云-降水-辐射相互作用研究领域,气溶胶层的垂直分布特征及其与云层在垂直方向上的相对位置对于准确理解气溶胶辐射效应(直接效应)、微物理效应(间接效应)以及他们之间复杂的竞争机制具有非常重要的意义。本项目利用长时间序列(2006—2013年)全球范围内的卫星激光雷达传感器CALIOP提供的垂直特征掩膜(VFM)和气溶胶消光系数产品,根据气溶胶垂直方向发生概率和气溶胶光学厚度(AOD)垂直分布概率,分别定义了2种气溶胶垂直分布概率最大似然高度:MPH_OF和MPH_AOD。全球6个气溶胶浓度较高的区域为热带大西洋地区的撒哈拉气团影响区(SAL)、西非的季风区(WAM)、南大西洋区(SAO)、南亚区(SEA)、中国南海、亚马孙热带雨林区(AMZ)和西北太平洋区(NWP),这些区域的气溶胶和云的垂直分布特征的准确厘定对于研究大气污染远距离输送、气溶胶云相互作用、天气气候模式参数化等都具有重要科学价值。对上述6个区域气溶胶云垂直分布的逐月分析发现:在SAL区存在明显的季节性的沙尘输送现象;在WAM和NWP2个区则存在明显的沙尘和烟尘气溶胶,两者分布高度不一致,且该区域的所有气溶胶的源地均是东北亚;在SAO区,由撒哈拉南部森林大火或其他生物质燃烧产生的烟尘输送到该区域,绝大多数均存在于层积云之上,一定程度上证实了该区域之所以成为国际上研究云上气溶胶辐射强迫效应的理想场所。同理,在SAO、SEA和AMZ等区域,烟尘气溶胶也较易发生在层云之上。经过进一步的垂直概率计算分析发现:由于气溶胶主要分布在近地面,基于气溶胶发生概率计算得到的MPH_OF分布高度往往高于基于AOD概率计算得到的MPH_AOD。气溶胶在离地面较高的区域有较大的发生概率,而AOD大值区主要集中在近地面,这是因为绝大多数气溶胶排放源区分布在地面或近地面,而当气溶胶垂直向上输送到一定高度后,其浓度将会大大稀释。(郭建平)

1.14 长三角地区相对湿度对气溶胶散射系数影响研究

气溶胶的散射能力及辐射强迫与相对湿度密切相关。为了更好地了解气溶胶吸湿增长对气溶胶散射系数、辐射强迫的影响,2013年春季在长三角地区临安区域本底站利用加湿浊度仪系统对相对湿度40%~90%范围内气溶胶的吸湿增长因子进行了测量。还同步进行了气溶胶数谱分布和亚微米气溶胶化学成分的观测。临安区域本底站气溶胶吸湿增长观测结果显示,在85%的相对湿度下,气溶胶散射系数的吸湿增长因子的变化范围在1.29~1.86。相对湿度从40%升高到85%,气溶胶散

射系数平均增长了 $(58 \pm 12)\%$ ，后向散射系数平均增长了 $(25 \pm 7)\%$ ，后向散射比平均减少了 $(21 \pm 4)\%$ 。另外，由化学成分对气溶胶吸湿增长的影响分析可以看出，化学组分是影响气溶胶吸湿增长能力的决定性因素。总体而言，吸湿增长因子随着有机气溶胶所占比例增大而减小，随无机离子所占比例增大而增大，其中，硝酸盐百分比与相对湿度（85%）呈强烈正相关，并与吸湿增长曲线密切相关，硝酸盐含量越高，吸湿增长曲线曲率越小。气溶胶的吸湿增长还使得气溶胶的直接辐射强迫增加约47%（图5）。（孙俊英）

1.15 北京大气颗粒物中糖类化合物的成分及来源

采用高效阴离子交换色谱-脉冲安培检测（HPAEC-PAD）分析方法，对北京城区PM_{2.5}和PM₁₀中糖类化合物进行定量分析。在北京大气气溶胶中共检出14种糖类化合物，分为脱水糖、糖和糖醇三大类。脱水糖包括左旋葡聚糖、甘露聚糖半乳聚糖。糖包括葡萄糖、果糖和海藻糖。糖醇包括阿拉伯糖醇、甘露糖醇、丙三醇、苏糖醇、2-甲基丁四醇（2-甲基苏糖醇和2-甲基赤藓糖醇）、木糖醇和肌醇。脱水糖来源于生物质燃烧，秋冬季节的浓度水平明显高于春夏；糖和糖醇来源于生物源排放，冬季浓度水平明显低于其他季节。PMF源解析模型的结果表明，北京大气气溶胶中糖类化合物的来源主要可以分为6类，包括生物质燃烧、异戊二烯SOA、土壤悬浮、真菌孢子、花粉及丙三醇富集源。（梁林林）

2 大气成分模式的发展应用及大气成分的影响研究

2.1 环境气象精细化监测预报与评估

自主研发改进了气溶胶/化学数值模拟系统（CUACE/Chem），特别是发展了其中多组分气溶胶通过辐射与气象条件的双向反馈机制、气溶胶与云-降水相互作用的化学物理过程，实现了气溶胶-CCN-云-辐射-降水一体化、双向耦合的数值模拟。参加了4项重大活动气象保障、7项减排效果评估工作、20多次环境气象会商。包括：2014年APCE期间环境气象预报及减排评估，2015年冬奥会申办期间环境气象预报分析，抗战胜利70周年庆典活动环境气象预报服务，2014年全国及主要区域减排效果评估等。其中APEC会议期间大气污染物减排效果评估得到总书记、总理、副总理的批示。协调国家局和区域中心的雾霾监测和预报业务，已经向北京市气象局移植了CUACE中长期预报版，支持10~30天的雾霾预报。同时也与广东省气象局协调，移植CUACE的GRAPES版本。在CUACE精细化和套网格版本开发与应用方面，开发了CUACE离线套网格运行方案，实现了任意分辨率网格设置及数据匹配技术：编写了由粗网格预报场计算细网格模式侧边界的接口模块，使CUACE模式可以离线进行任意网格配置、任意嵌套区域的多重套网格运行。使得CUACE可以满足低、中、高不同分辨率的需求，最低分辨率可达1~3 km。（刘洪利）

2.2 事故物质的大气迁移转化规律研究

“事故物质的大气迁移转化规律”课题的研究目标是建立一个描述危险化学品在大气中迁移转化过程的“事故物质-多尺度气象输送耦合模式系统”。课题完成了城市气象/示踪试验、城市大气污染物车载移动观测试验和室内环境下示踪物扩散试验，获得了有效的观测资料，发展了观测试验方法；利用CFD模式研究了边界层过程对污染物输送和扩散的影响，实现了中尺度模式WRF和街区尺度模式Fluent的单向耦合，并提出相应的事故预警方法。（马建中）

2.3 雾-霾天气污染输送及气溶胶与边界层相互作用

基于高分辨率全国15 km环境气象预报模式GRAPES_CUACE3.5D 雾霾/能见度预报系统模拟研

究了边界层与 $PM_{2.5}$ 的相互作用机制以及河北输送对北京的贡献。得到如下结论:(1)气溶胶直接辐射效应极大减弱了边界层的湍流扩散作用,导致边界层更加稳定,对霾污染为正反馈,气溶胶直接辐射同时加大了边界层风速,减弱了副热带高压,有利于霾的消散,呈现负反馈。二者的综合效应,气溶胶直接辐射效应使得更多 $PM_{2.5}$ 积聚在近地面,加重了霾污染程度,但对霾的持续时间基本没有影响。(2)北京地区 $PM_{2.5}$ 浓度和其以南地区的南风具有很好的相关性。地面到800 hPa高度是京津冀污染物输送的主要高度,900 hPa高度附近是污染物输送最为重要的高度。在京津冀严重霾天气发生时,北京和河北之间 $PM_{2.5}$ 的输送是相互的,在不同的时间北京既可以是 $PM_{2.5}$ 的源也可以是汇。对2013年12月6—7日严重霾天气的模拟研究显示,在此次霾污事件发生的大部分时间,北京是向周边地区净输出 $PM_{2.5}$;但是河北南部污染物的输送对北京地区 $PM_{2.5}$ 极大值的贡献达到55%,超过了本地污染源。(王宏)

2.4 综合减排黑碳及其协同排放的气溶胶对气溶胶净冷却效应的影响

采用气溶胶-气候在线耦合模式BCC_AGCM2.0.1_CUACE/Aero,以及给定的海表温度和海冰量,结合典型浓度路径(RCPs)情景的气溶胶排放量,估算了消除黑碳及其协同排放物种的某些排放源对气溶胶辐射效应的影响。研究发现,如果根据RCP2.6情景,仅将黑碳排放量减少到2100年的预估水平,则大气层顶全球年平均气溶胶净冷却效应将比2000年水平增强 0.12 W/m^2 。这将有利于减缓全球变暖。然而,如果同时减排黑碳及其协同排放物种(二氧化硫和有机碳),气溶胶负的直接和间接辐射效应均会减弱。如果根据RCP2.6、RCP4.5和RCP8.5情景,以不同方式将所有这些气溶胶排放量减少到2100年的预估水平,大气层顶全球年平均气溶胶冷却效应将比2000年水平减弱 $1.7\sim 2.0\text{ W/m}^2$ 。由于尚没有只去除黑碳而不影响其协同排放物种的有效方式,因此该研究表明,减排黑碳可能会导致未来地球气候系统不被预期地变暖。(王志立)

2.5 四流辐射传输算法对气溶胶直接辐射效应和强迫的影响

利用包含了二流和四流辐射方案的气溶胶-气候耦合模式的研究表明,目前气候模式普遍使用的二流辐射传输算法明显过低估计了气溶胶的短波直接辐射效应和加热率。在当前条件下,对于全天(晴空)情况,四流算法分别增强了大气顶、大气中和地表的全球年平均气溶胶短波直接辐射效应超过8%(14%)、15%(18%)和12%(15%)。四流算法造成大气顶除了北极、青藏高原、阿拉伯和撒哈拉之外的区域气溶胶直接辐射效应的差别为负值,大气中的差别为正值,地表的差别为负值,最大差别超过 4.0 W/m^2 。四流算法造成气溶胶短波加热率的增加一般超过10%,有些区域甚至超过100%。研究结果还表明,二流算法也过低估计了人为气溶胶的直接辐射强迫。明显的过低估计出现在北半球中纬度区域,晴空条件下最大过低估计接近 0.6 W/m^2 。该研究表明,为了减小气候模式估算气溶胶直接辐射效应的不确定性,很有必要采用多流的辐射传输算法。(王志立)

2.6 基于集合最优插值方法的黑碳气溶胶源强反演订正研究

利用统计资料、排放因子等数据构建的自下而上的黑碳气溶胶(BC)源强清单具有很大不确定性。针对这一问题,研究探讨利用集合最优插值方法对黑碳气溶胶源强进行反演订正。依据气溶胶源强时空分布特点,开发了基于傅里叶变换方法的二维随机扰动产生模块;并根据黑碳气溶胶源排放特征,将原来只考虑空间相关的扰动方案更新完善为同时考虑时间、空间相关的新方案,使集合样本更合理地包含观测资料。针对有限样本给背景误差协方差矩阵带来虚假信息问题,采用对背景误差协方差中的每个元素乘一个随距离衰减的相关函数的方案,有效剔除虚假相关,使源强订正更为准确。利用化学天气数值模式CUACE的模拟结果,结合地面观测资料对2008年各月黑碳源强进行了反演,订正前全国BC排放总量为1449.6 Gg,订正后为2539.3 Gg,不确定性由 $[-80\%, 227\%]$,

减少为[-58%, 102%], 我们还详细估算了订正前后各省份源强总量及变化。使用订正过的源强清单进行模拟对比, 发现其结果与观测更为接近, 月平均误差从-74.34% 减少到-37.20%, 日平均的均方根误差 (RMSE) 也减少了近30%。研究表明, 集合同化方法能减少气溶胶源强的不确定性, 是提高气溶胶模拟准确率的一个有效手段。(汪萍)

2.7 GRAPES-CUACE大气化学伴随模式的构建及应用

完成CUACE气溶胶化学模块的切线性和伴随模式的编写、组装和测试, 完成GRAPES与CUACE之间接口程序伴随代码的编写、测试, 完成GRAPES-Meso中和和化学物种输送过程有关代码的提取、伴随构建及测试。可利用伴随方法反向追踪某污染事件的重点源区(即敏感系数较大源区)及重点排污时段(即积分步上敏感系数较大时段)。利用伴随方法确定的关键污染源区与行政区划不重合, 对前者实施减排效率更高, 目标时刻前17~18 h内的源排放对目标函数的影响显著高于其之前源排放的影响。实施大气污染管控措施时, 可利用伴随模式反向追踪关键源区及源排放时段, 突破行政区划局限确定减排区域, 有效选择减排时段, 提高减排效率(图6)。(安兴琴)

2.8 2013年1月华北地区重霾污染过程SO₂和NO_x的CMAQ源同化模拟研究

以2006年中国地区的INTEX-B排放清单为基础, 采用CMAQ模式污染源同化方法, 反演更新了2013年1月重霾污染过程华北地区的SO₂和NO_x排放源。应用WRF-CMAQ模式以及2006年INTEX-B初始排放源和2013年1月改进的排放源, 分别模拟了2013年1月9—15日和28—31日2次持续重霾污染过程的SO₂和NO₂浓度, 并与华北地区47个环境监测站点实测值进行对比, 重点分析了基于初始源和同化反演源的模拟效果及其改进原因。本文亦采用2012年清华大学编制的东亚地区MEIC排放清单评估了SO₂和NO_x同化反演源的合理性。分析结果表明:(1) CMAQ模式污染源同化方法可适用于重霾污染过程, 即采用同化反演源模拟的SO₂、NO₂浓度时空变化特征与实测值较一致, 而且可反映SO₂、NO_x排放源强的动态变化特征。(2) 基于同化反演源的SO₂、NO₂浓度模拟效果明显优于2006年INTEX-B排放源, 其时间变化趋势与实测值较一致, 而且可模拟重霾污染过程SO₂、NO₂浓度的峰值。(3) 采用反演源模拟的SO₂、NO₂浓度空间区分布特征与实测值较一致, 而且可较好反映重污染区的极值分布特征。(4) 经污染源同化改进后SO₂、NO₂模拟浓度与实测值的相关系数有所提高, 误差明显减小; SO₂的改进效果略优于NO₂, 这与污染源对2种污染物浓度的影响差异有关。(5) 初始源中SO₂、NO_x排放源的空间分布和强度与2012年清华大学编制的排放源强差异较大, 而同化反演源的空间分布和强度均接近于实际调查源, 可反演得到重点地区的高污染源分布特征。本文研究结果将为改进重霾污染过程的空气质量预报、减小自下而上建立的排放源清单不确定性、评估SO₂、NO_x等排放源的影响效应以及不同气象条件下区域排放源的动态调控等提供新技术途径和研究思路。(程兴宏)

2.9 基于CMAQ模式和自适应偏最小二乘回归法的中国地区PM_{2.5}浓度动力-统计预报方法研究

采用CMAQ模式和自适应偏最小二乘回归法相结合的动力-统计预报方法对2014年1—12月全国252个环境监测站的PM_{2.5}浓度逐时预报值进行了滚动订正, 分析了订正前后PM_{2.5}浓度的时空变化特征, 重点研究该方法在中国不同地区不同季节的适用性。结果表明:(1) CMAQ模式预报的PM_{2.5}浓度年平均和秋冬季季节平均偏差表现为非均匀空间分布特征, 即辽宁、山东部分地区、川渝地区以及华中、华东、华南大部分地区预报偏高, 京津冀和西部大部分地区预报偏低; 订正后PM_{2.5}浓度与实测值的空间分布较一致, 上述偏高和偏低地区的PM_{2.5}浓度预报误差显著减小。秋冬季PM_{2.5}浓度预报和订正偏差均大于年平均。(2) 全国区域平均PM_{2.5}浓度实测值存在明显的季节变化特征, 1—3和11—12月较大, 其他月份较小; PM_{2.5}浓度预报误差较大, 多数时刻预报偏低, 尤其是1—3和

11—12月偏低较明显。订正后 $PM_{2.5}$ 浓度与实测值较接近，而且时间变化趋势较一致，秋冬季 $PM_{2.5}$ 浓度预报和订正偏差亦明显大于春夏季。(3)秋冬季4个重点污染区域中京津冀地区 $PM_{2.5}$ 实测浓度的区域平均值较大，川渝地区次之，长三角和珠三角较小；珠三角地区 $PM_{2.5}$ 浓度预报和订正效果较好，川渝和长三角地区次之，京津冀地区相对较差；经滚动订正后，全年和秋冬季时段 $PM_{2.5}$ 浓度订正值与实测值的相关系数均显著增加，误差显著减小，尤其是秋冬季订正效果较好。(4)川渝地区的订正改进幅度最大，长三角和京津冀地区次之，珠三角地区较小。(5)本文方法均适用于非污染日和污染日全国范围的 $PM_{2.5}$ 预报浓度订正，两种天气过程 $PM_{2.5}$ 浓度的订正效果均较好；该方法对于改进京津冀地区污染日的 $PM_{2.5}$ 浓度预报更有效，其他3个地区非污染日的订正改进效果优于污染日。本文研究结果可为改进空气质量预报、重霾污染天气预警和防治提供新技术途径和科学依据。(程兴宏)

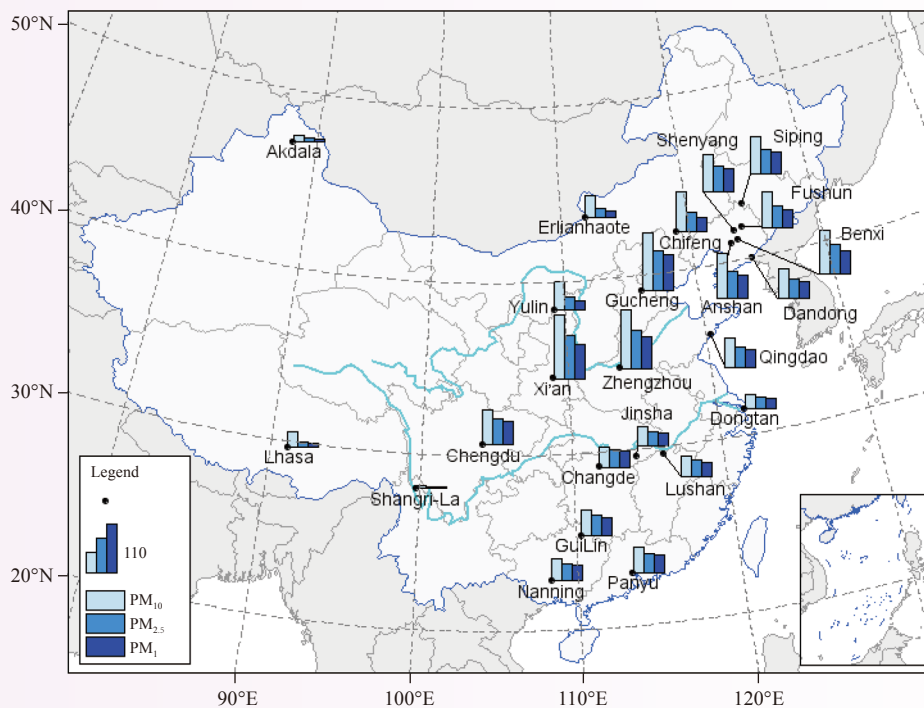


图 1 各站点 PM_{10} 、 $PM_{2.5}$ 和 PM_1 平均浓度分布

Fig. 1 Concentrations of PM_{10} , $PM_{2.5}$ and PM_1 in China

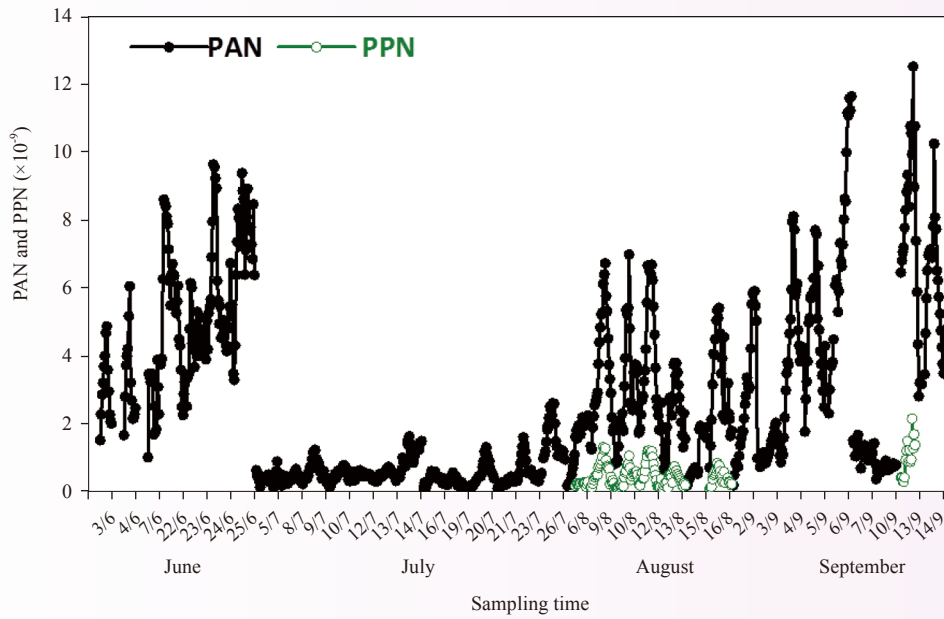


图 2 北京市夏季大气过氧乙酰基硝酸酯 (PAN) 和过氧丙酰基硝酸酯 (PPN) 的时间序列
Fig. 2 Time series of ambient PAN and PPN in Beijing during Jun.–Sep. 2010

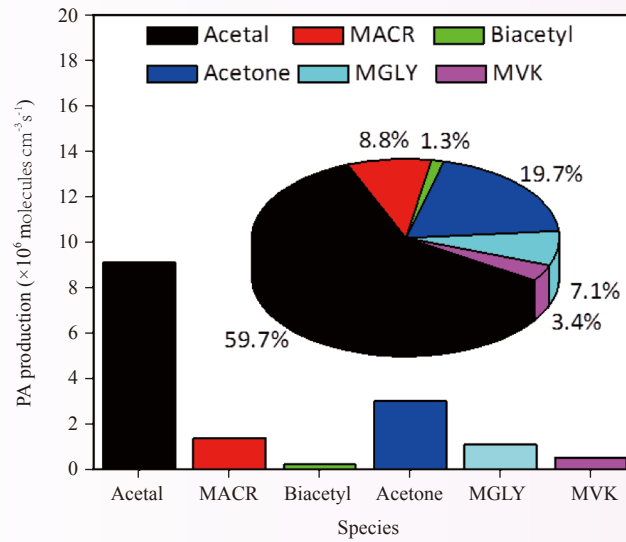


图 3 北京市夏季大气含氧挥发性有机物 (OVOC_s) 对过氧乙酰基自由基 (PA) 的产生效率及贡献
Fig. 3 The PA production rate for each source and the respective contributions

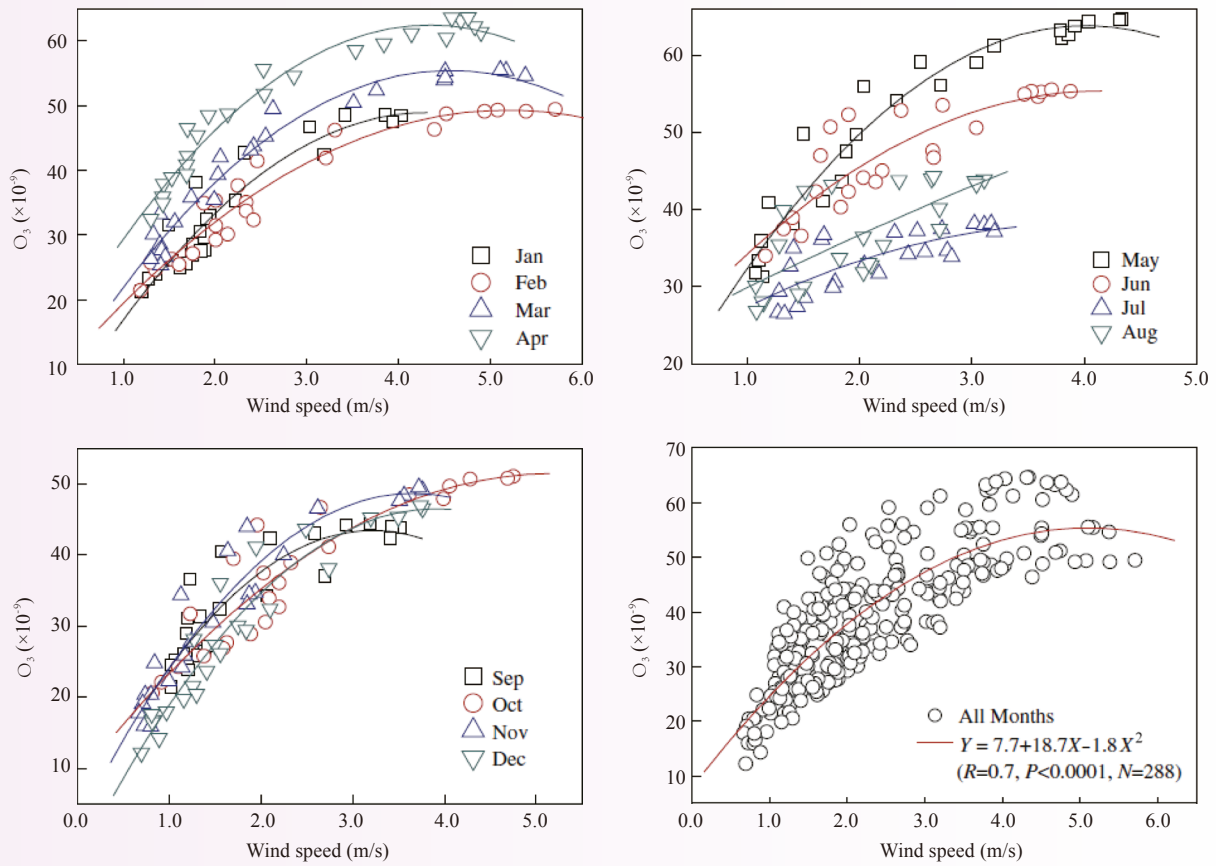


图 4 当雄不同时刻地面 O_3 与风速平均值在各月及全年的关系（曲线为拟合得到的抛物线，均统计显著（ $p<0.0001$ ））
 Fig. 4 Monthly/yearly relationships between surface O_3 and wind speed averaged for different times of day at Dangxiong. The curves are fitted parabolic relationships and they are all statistically significant at a level of $p<0.0001$.

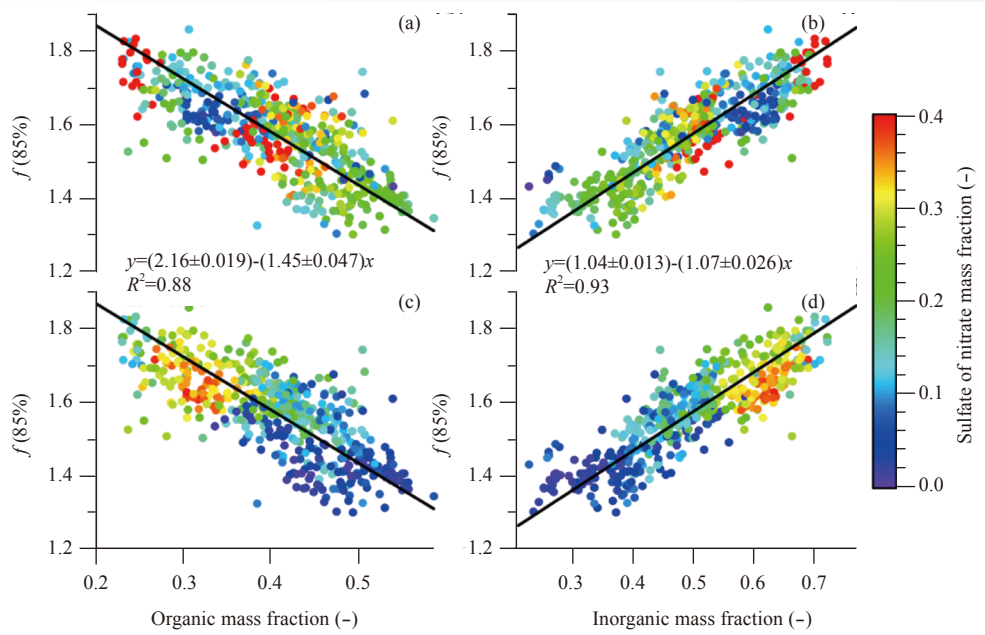


图 5 散射吸湿增长因子(85%, 550 nm)与气溶胶有机物、无机物质量分数的关系 (a, b为数据点颜色是硫酸盐的质量分数; c, d为数据点颜色是硝酸盐的质量分数, 黑色实线是拟合直线)

Fig. 5 Scattering enhancement factor $f(85\%, 550 \text{ nm})$ vs. organic mass fraction and inorganic mass fraction determined from AMS and MAAP: (a, b) $f(85\%, 550 \text{ nm})$ vs. organic mass and inorganic mass fraction colored by sulfate mass fraction; (c, d) $f(85\%, 550 \text{ nm})$ vs. organic mass fraction and inorganic mass fraction colored by nitrate mass fraction. The solid black line represents a bivariate linear regression including the uncertainty of $f(85\%, 550 \text{ nm})$ and the standard deviation of chemical composition

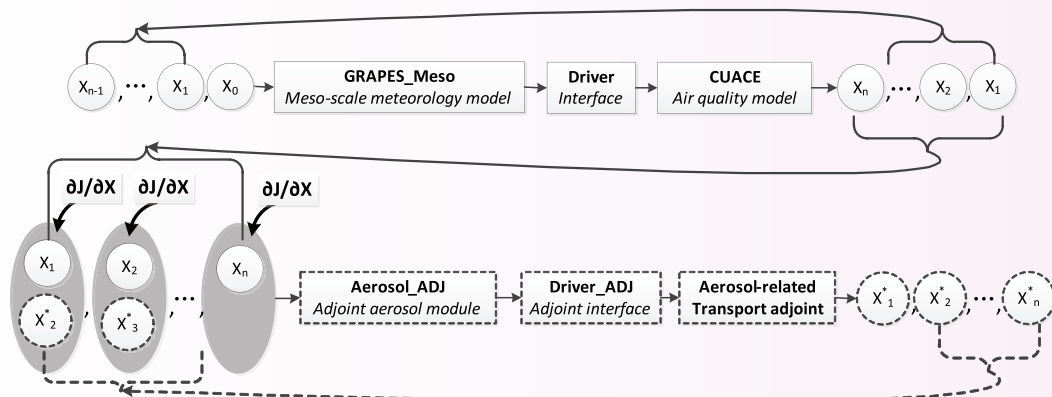


图 6 GRAPES-CUACE大气化学模式及 CUACE-ADJ伴随模式流程

Fig. 6 Framework of GRAPES-CUACE, CUACE-ADJ and the flowchart of parameter transmission

Progress in Atmospheric Composition and Atmospheric Chemistry Research

1 Observational studies of atmospheric composition and related properties

1.1 Long-term measurements of aerosol optical properties for China

Ground-based, quality assured, monthly mean AODs and their yearly variations were presented over a large area of China. Large AODs (>0.60) mainly occur in central and eastern China where heavy industrial and other anthropogenic emissions lead to high aerosol loadings. Aerosol particles generally decrease in size when moving from north to south, which is due to the effect of sand-dust events on northern China region and the effect of secondary aerosols on southern China region. The AOD level at remote sites is a little bit lower than the global average, while that at rural desert and Loess Plateau stations is about a factor of 1.7–2.1 higher and that at rural sites in eastern China and urban sites a factor of 2.7–3.7 higher. The annual variations in the AODs at CARSNET long-term (2002 to 2013) observation sites show an increase from 2009 to 2013, which could be affected by changes in meteorological elements as well as variations in emissions. (Che Huizheng)

1.2 Synergistic effect between SO_2 and HCOOH on the surface of CaO

Due to the altered properties of particles and the budget of trace gases, heterogeneous reactions on mineral aerosols become an important subject in the atmospheric chemistry. However, synergistic effects between trace gases on the surface of mineral aerosol are largely uncertain. In this project, the synergistic effect between SO_2 and HCOOH on the surface of CaO was studied using in situ Diffusion Reflectance Infrared Fourier Spectroscopy (DRIFTS). From an analysis of the spectral features and kinetic curves, it is found that the heterogeneous reactions of SO_2 and HCOOH on the surface of CaO blocked each other. In addition, the formate and sulfite decreased when SO_2 and HCOOH were introduced into the reaction chamber simultaneously. Synergistic effect between SO_2 and HCOOH on the surface of CaO was mainly divided into two aspects according to step-by-step experiments. Less reactive sites available for adsorption because of the coexistence of SO_2 inhibited the reaction of HCOOH on the surface of CaO , resulting in the decrease of the formation of formate. On the other hand, HCOOH could prevent SO_2 from reacting with CaO so that the formation of sulfite decreased. (Wu Lingyan)

1.3 Characteristics and long-term trends of surface ozone at the Mt. Waliguan GAW station, China

Long-term variation trend of baseline ozone is highly needed information for environmental and climate change assessments. So far, studies about the long-term trends of ozone at representative sites are mainly available for European and North American sites. Similar studies are lacking for China and many other developing countries. Measurements of surface ozone were carried out at a global baseline Global Atmospheric Watch (GAW) station in the north-eastern Tibetan Plateau region (Mt. Waliguan, $36^\circ 17' \text{N}$, $100^\circ 54' \text{E}$, 3816 m a.s.l.) for the period of 1994 to 2013. In order to uncover the variation characteristics, long-term trends and influencing factors of surface ozone at this remote site in western China, a two-part study has been carried out, with this part focusing on the overall characteristics of diurnal, seasonal and long-term variations of surface ozone and its variation trends. To obtain reliable ozone trends, we performed the Mann-Kendall trend test

and the Hilbert-Huang Transform (HHT) analysis of the ozone data. Our results confirm that the mountain-valley breeze plays an important role in the diurnal cycle of surface ozone at Waliguan, resulting in higher ozone values during the night and lower ones during the day, as was previously reported. Systematic diurnal and seasonal variations were found in mountain-valley breezes at the site, which were used in defining season-dependent daytime and nighttime periods for trend calculation. Significant positive trends in surface ozone were detected for both daytime ($(2.4 \pm 1.6) \times 10^{-9}/10\text{yr}$) and nighttime ($(2.8 \pm 1.7) \times 10^{-9}/10\text{yr}$). The largest nighttime increasing rate occurred in autumn ($(2.9 \pm 1.1) \times 10^{-9}/10\text{yr}$), followed by spring ($(2.4 \pm 1.2) \times 10^{-9}/10\text{yr}$), summer ($(2.2 \pm 2.0) \times 10^{-9}/10\text{yr}$) and winter ($(1.3 \pm 1.0) \times 10^{-9}/10\text{yr}$), respectively. The HHT spectral analysis identified four different episodes with different positive trends, with the largest increase occurring around May 2000 and October 2010. The HHT results suggest that there were 2–4, 7 and 11 years periodicities in the time series of surface ozone at Waliguan. (Xu Wanyun)

1.4 Effect of aluminium dust on secondary organic aerosol formation in m-xylene/ NO_x photo-oxidation

As an important anthropogenic VOC, m-xylene attracts much attention due to its potential in SOA formation. In this study, effects of aluminium dust (boehmite and alumina) on SOA yield and aerosol size in m-xylene/ NO_x photo-oxidation were investigated in an indoor smog chamber at 30 °C and 50% RH. Compared to the seed-free system, the presence of aluminium seeds resulted in an increase in the SOA yield, and also enhanced the O_3 concentration in the chamber. The photolysis of O_3 is a major source of OH radical, which is the most important oxidant of m-xylene. The increase in O_3 concentration could result in the generation of more OH radicals, and finally contribute to the SOA formation. Seed particles influence the SOA size mainly by acting as condensation nuclei. SVOC_s were condensed onto these nuclei, resulting in the increase in SOA size. However, when aluminium seeds with high concentrations were introduced into the system, SVOC_s that had been condensed onto each particle were dispersed by these seeds, leading to the reduction in aerosol size. (Liu Chang)

1.5 Spatial and temporal variations of the concentrations of PM_{10} , $\text{PM}_{2.5}$ and PM_1 in China

Concentrations of PM_{10} , $\text{PM}_{2.5}$ and PM_1 were monitored at 24 CAWNET (China Atmosphere Watch Network) stations from 2006 to 2014. The highest particulate matter (PM) concentrations were observed at the stations of Xi'an, Zhengzhou and Gucheng, installed in the Guanzhong Plain and the Hua Bei Plain (HBP). The second highest PM concentrations were observed in Northeast China, followed by South China. According to the latest air quality standards of China, 14 stations reached the PM_{10} standard, and only 7 stations, mainly rural and remote stations, reached the $\text{PM}_{2.5}$ standard. The ratio of $\text{PM}_{2.5}$ to PM_{10} showed a clear increasing trend from northern to southern China, because of the substantial contribution of coarse mineral aerosol in northern China. The ratio of PM_1 to $\text{PM}_{2.5}$ was higher than 80% at most stations. PM concentrations tended to be highest in winter and lowest in summer at most stations, and mineral dust influenced the results in spring. A decreasing interannual trend was observed in the HBP and in southern China for the period 2006 to 2014, but an increasing trend occurred at some stations in northeast China. Bimodal and unimodal diurnal variation patterns were identified at urban stations. Both emissions and meteorological variations dominate the long-term PM concentration trend, while meteorological factors play a leading role in the short-term (Fig.1). (Wang Yaqiang)

1.6 CO_2 concentration in representative source and sink areas at Shangdianzi atmospheric background station in Beijing

In order to study the spatial representativeness of CO_2 source and sink at a single station and the regional

flux characteristics, the atmospheric inversion model FLEXPART was used to simulate and determine the main source of air mass impacting on observed concentration at Shangdianzi station. Carbon Tracker model was also used to inverse spatial and temporal distribution of CO₂ concentrations and fluxes. The optimal threshold of footprint function was found with a numerical iterative approach and correlation analysis, and then the distribution of source and sink areas of CO₂ observed concentration at the station was obtained. Then, the in-situ CO₂ observed concentrations were screened into two parts, the background and the non-background, for tracking the background and non-background source areas of a station with FLEXPART model. The results show that the background and non-background source regions were obviously different and changed with the seasons. In the potential source area where footprint function was greater than the threshold, the background and non-background regional net fluxes changed differently. The fossil fuel flux was smaller and the biosphere flux was larger in the background area. However, it was opposite for the non-background area. Therefore, source and sink areas, influencing the concentrations of an observing station, and regional characteristics of fluxes, could be quantified using inversion models.(Cheng Siyang)

1.7 Pollution levels, diurnal variation, source and sink of atmospheric peroxyacetyl nitrate in the summertime of Beijing

Atmospheric PAN is an important indicator in the photochemical smog, which plays a crucial role in the atmospheric chemistry and causes an adverse effect on human and plants. In this study, we conducted the simultaneous measurements of atmospheric PAN and PPN by using GC-ECD method in the summertime of Beijing. Their mean and maximum values were $(2.61 \pm 2.57) \times 10^{-9}$ and 12.50×10^{-9} for PAN, and $(0.52 \pm 0.38) \times 10^{-9}$ and 2.16×10^{-9} for PPN, respectively. In addition, they both show distinct diurnal variations and a very positive correlation with each other. Based on the simple steady method, we investigated the contributions of atmospheric oxygenated volatile organic compounds to the photochemical formation of PAN such as acetaldehyde, acetone, biacetyl, methyl vinyl ketone, methacrolein, methyl glyoxal, respectively. The results suggest that acetaldehyde was the predominant OVOC with the contribution of 59.7%, followed by acetone (19.7%) (Fig. 2–3). (Zhang Gen)

1.8 Two-year measurements of surface ozone at Dangxiong, a remote highland site in the Tibetan Plateau

Measurements of surface O₃ and carbon monoxide (CO) were made from September 2009 to August 2011 at Dangxiong (30.48°N, 91.10°E, 4187 m a.s.l.), a remote highland site in a southern valley of the Nyainqêntanglha Mountains in the Tibetan Plateau, China. The monthly mean O₃ mixing ratio ranged from 29.1×10^{-9} to 51.4×10^{-9} , with an average of 38.5×10^{-9} , and the maximum value was observed in May. The average diurnal cycle of O₃ concentration showed a minimum in early morning and a maximum in the afternoon, with a broader “high platform” from the late morning to the late afternoon, which resembled that of surface wind speed. The concentration of surface O₃ was highly significantly correlated with tropospheric column O₃ over the regions surrounding Dangxiong and with that of surface O₃ observed at a site north of the Nyainqêntanglha Mountains, suggesting a good regional representativeness of surface O₃ at Dangxiong. In the afternoon when stronger winds blew, surface air showed distinct features of free-atmospheric air, with higher O₃, lower CO, and lower relative humidity (RH). The negative O₃-CO and O₃-RH correlations in most months indicate a significant influence of air masses from the free troposphere. A trajectory analysis suggests that air masses originating from the south of the site make a negative net contribution to surface O₃ and a positive contribution to CO and humidity, and those from the northwest sector contribute conversely to the respective quantities(Fig. 4). (Xu Xiaobin)

1.9 Increased mixing ratio of surface ozone by a nighttime convection process over the North China Plain

Surface ozone and other reactive gases were observed at the Gucheng (39°08'57"N, 115°44'02"E) in Hebei Province of China from June to September in 2013. There were 10 cases with rapid increases in the mixing ratio of surface ozone and sharp decreases in the mixing ratios of nitric oxides and carbon monoxide when convection processes occurred at night. The mixing ratio of surface ozone mostly increased from less than 30×10^{-9} to 60×10^{-9} – 80×10^{-9} within less than 1 h and stayed at a higher level during the night and the next morning than that on the undisturbed days. Such phenomenon cannot be explained by photochemical production. The increase rate of surface ozone level is not correlated with wind speed. Therefore, the change in ozone cannot be attributed to horizontal transport of polluted air mass. In order to understand the phenomenon, meteorological data from Gucheng and from ECMWF reanalyses were analyzed. Surface pseudo-equivalent potential temperature (θ_{se}) for each case was calculated from the simultaneously measured meteorological data. In all nighttime cases of convection process, the surface θ_{se} values decreased dramatically within a short time, coinciding with the steep increases in the ozone level and the wind speed. This suggests that the mixing ratio of surface ozone is enhanced by descending air from aloft. The convective process occurred in the warm area ahead of the front in most cases and only once near the cold front. These clearly indicate that convective downdrafts transported air with higher ozone and lower θ_{se} from upper atmosphere to the surface layer. With the vertical profiles of θ_{se} values calculated from ECMWF reanalysis data, the levels of origins of convective downdrafts were estimated as from around 500–800 hPa. Vertical profiles of ozone observed using an unmanned aircraft near the station show that ozone mixing ratio over the boundary layer at dusk is higher than 60×10^{-9} , supporting the view that the increased mixing ratio of surface ozone during and after the nighttime convection process is caused by air descending from the lower to mid free-troposphere. The phenomenon with ozone enhancement is also observed at an urban station in Beijing. In most cases when Gucheng and Beijing urban are impacted by the same convective systems, ozone and θ_{se} at both sites show similar trends. All above implies that ozone mixing ratio maintains around 60×10^{-9} – 80×10^{-9} in the mid and lower free-troposphere over the North China Plain in summer and early autumn, and an ozone increase by convective downdrafts is able to impact a large area of the North China Plain. Compared with other places, a convection process causes a larger ozone increase, which may exert stronger impact on atmospheric environment. (Xu Xiaobin)

1.10 The characteristics of atmospheric ammonia at Gucheng, a rural site in the North China Plain in summer 2013

In-situ measurement of ambient ammonia (NH_3) and water-soluble ions in $\text{PM}_{2.5}$ was conducted at Gucheng station in Hebei Dingxing county from June to August 2013. The concentrations of NH_3 at Gucheng site ranged from 0.9×10^{-9} to 862.9×10^{-9} , with the average of $(43.9 \pm 65.9) \times 10^{-9}$. NH_3 concentrations increased sharply after fertilizer application in July for summer maize. Ammonia was of a significant diurnal variation during the sampling period. NH_3 concentration maxima occurred at 09:00 and the minima at 19:00. The average mass concentration of ammonium in $\text{PM}_{2.5}$ was $19.77 \pm 33.24 \text{ g m}^{-3}$ in summer 2013. Ammonium showed significantly positive correlations with NH_3 concentration. Higher sulfur oxidation ratio (SOR) and ammonia conversion ratio (NHR) led to an important effect of SO_2 to SO_4^{2-} and NH_3 to NH_4^+ conversion. The dependence of inorganic $\text{PM}_{2.5}$ on the NH_3 levels suggests that controlling NH_3 emission from agricultural sources is an efficient way to reduce secondary inorganic particle pollution in the North China Plain. (Meng Zhaoyang)

1.11 Characterization of submicron aerosols and their effect on visibility during a severe haze-fog episode in Yangtze River Delta

Particle size, composition and optical properties were measured at a regional atmospheric background station in the Yangtze River Delta (YRD) to understand the formation and evolution of haze-fog episodes in January 2013. The peak of particle number/size distribution was in the size range of 80–100 nm during the measurements. PM_{10} mass concentration contributed 84% to the total particle mass (PM_{10}). Based on visibility and ambient relative humidity, three types of weather conditions (i.e., clear, hazy and foggy) were classified in this study. The extinction coefficients of PM_{10} and PM_{10} under dry conditions were simulated by the Mie model. Under dry conditions, PM_{10} was found to contribute approximately 91% to the light extinction coefficient of PM_{10} . However, the PM_{10} in a dry state was found to contribute approximately 85% to the ambient extinction coefficient of PM_{10} during clear conditions, 58% during hazy conditions and approximately 41% during foggy conditions. The variation of the dry PM_{10} contribution was related to the water uptake of particles under different relative humidity conditions. A severe haze-fog event on January 14–17 was discussed in a more detail as a case study. Two episodes were chosen to show that nitrate and organics dominated the aerosol composition during the severe haze-fog episode, which was related to secondary aerosol formation and air mass origin. Nitrate played a more dominant role than sulfate in heavy haze formation in the YRD region, which was different from the North China Plain region. (Shen Xiaojing)

1.12 Multi-sensor quantification of aerosol-induced variability in warm clouds over eastern China

Aerosol-cloud (AC) interactions remain uncharacterized due to difficulties in obtaining accurate aerosol and cloud observations. In this study, we quantified the aerosol indirect effects (AIE) on warm clouds over eastern China based on near-simultaneous retrievals from MODIS/AQUA, CALIOP/CALIPSO, and CPR/CLOUDSAT between June 2006 and December 2010. The seasonality of aerosols from ground-based PM_{10} (aerosol particles with a diameter of 10 μm or less) significantly differed from that estimated using MODIS aerosol optical depth (AOD). This result was supported by the lower level frequency profile of aerosol occurrence from CALIOP, indicative of the significant role of CALIOP in the AC interaction. In order to focus on warm clouds, cloud layers of a base (top) altitude above 7 (10) km were excluded. The combination of CALIOP and CPR was applied to determine the exact position of warm clouds relative to aerosols out of the following six scenarios in terms of AC mixing states: (1) aerosol only (AO); (2) cloud only (CO); (3) single aerosol layer-single cloud layer (SASC); (4) single aerosol layer-double cloud layers (SADC); (5) double aerosol layers-single cloud layer (DASC); (6) others. The cases with a vertical distance between aerosol and cloud layer less (more) than 100 m (700 m) were marked as mixed (separated), and the rest as uncertain. Results show that only 8.95% (7.53%) were of the mixed (separated and uncertain) state among all of the collocated AC overlapping cases, including SASC, SADC, and DASC. Under mixed conditions, the cloud droplet effective radius (CDR) decreased with increasing AOD at a moderate aerosol loading ($AOD < 0.4$), and then became saturated at an AOD of around 0.5, followed by an increase in CDR with increasing AOD, a shape that is known as boomerang. Under separated conditions, no apparent changes in CDR with AOD were observed. We categorized the AC dataset into summer- and winter-season subsets to determine how the boomerang shape varied with a season. The response of CDR to AOD in summer exhibited similar but much more boomerang-like shape, as compared with the all year round case. (Guo Jianping)

1.13 CALIPSO inferred most probable heights of global dust and smoke layers

The vertical location of aerosol layers is critical for determining predominance of aerosol radiative and microphysical effects in the aerosol-cloud-precipitation-climate interaction. The space-borne lidar system, the

Cloud-Aerosol Lidar and Infrared Pathfinder Satellite Observations (CALIPSO), provides an unprecedented opportunity to observe vertical distributions of global aerosol layers. In this study we examine the most probable height (MPH) of dust and smoke layers, which are calculated either from aerosol occurrence frequency (OF) in vertical feature mask (VFM) or aerosol extinction profile. The study focused on six high-aerosol-loading regions where aerosols are of great interest to a range of scientific topics: Saharan Air Layer (SAL) over Tropical Atlantic, West African Monsoon region (WAM), Southeast Atlantic Ocean (SAO), Southeast Asia (SEA) and South China Sea, Amazon (AMZ) and Northwestern Pacific (NWP). The analysis reveals an interesting spatial and seasonal variability of different vertical mixtures over these regions: seasonal migration of dust layers over SAL, separation and mixture of dust and smoke layers over WAM and NWP, and smoke layer above clouds over SAO, SEA and AMZ. Results also indicate that the OF based MPH tends to be much higher than the AOD based MPH, owing to the predominating near-surface sources. Within the same vertical resolution grid of CALIPSO, aerosols are found with higher OF at higher levels but AOD tends to increase at lower levels, because most aerosol sources are near the surface and the aerosol layers transported to high altitudes are generally much more diluted over a larger spatial domain than those near the surface. (Guo Jianping)

1.14 Observations of relative humidity effects on aerosol light scattering in the Yangtze River Delta

Scattering of solar radiation by aerosol particles is highly dependent on relative humidity (RH) as hygroscopic particles take up water by RH. In order to achieve a better understanding of the effect of aerosol hygroscopic growth on light scattering properties and radiative forcing, the aerosol scattering coefficients at RH in the range of 40% to 90% were measured using a humidified nephelometer system in the Yangtze River Delta of China in March 2013. In addition, the aerosol size distribution and chemical composition were measured. During the observation period, the mean and standard deviation (SD) of enhancement factors at RH of 85% for the scattering coefficient, backscattering coefficient, and hemispheric backscattering fraction were 1.58 ± 0.12 , 1.25 ± 0.07 , and 0.79 ± 0.04 , respectively, i.e., aerosol scattering coefficient and backscattering coefficient increased by 58% and 25% as the RH increased from 40% to 85%. Concurrently, the aerosol hemispheric backscattering fraction decreased by 21%. The relative amount of organic matter (OM) or inorganics in PM_{10} was found to be a main factor determining the magnitude of $f(RH)$. The highest value of $f(RH)$ corresponded to the aerosols with a small fraction of OM, and vice versa. The relative amount of NO_3 in fine particles was strongly correlated with $f(85\%)$, which suggests that NO_3 played a vital role in aerosol hygroscopic growth during this study. The mass fraction of nitrate also had a close relationship with the curvature of the humidograms; higher mass fractions of nitrate were associated with humidograms that had the least curvature. Aerosol hygroscopic growth caused a 47% increase in the calculated aerosol direct radiative forcing at 85% RH, compared to that at 40% RH (Fig. 5). (Sun Junying)

1.15 The composition and source apportionment of saccharides in atmospheric particulate matter in Beijing

Based on the newly established high-performance anion exchange chromatography with pulsed amperometric detection (HPAEC-PAD), the saccharides in $PM_{2.5}$ and PM_{10} in Beijing from 2011 to 2012 were quantified. Fourteen saccharides were synchronously detected in the aerosols sampled in Beijing, which fell into three categories, i.e. anhydrosugar, sugar and alcohol dehydration. Anhydrosugar, coming from biomass burning, includes levoglucosan, mannosan and galactosan. Sugar and sugar alcohol, emitted by the primary biogenic emission, include glucose, fructose, trehalose, arabitol, mannitol, glycerol, threitol, 2-methyltrtols (2-methylthreitol and 2-methylerythritol), xylitol and inositol. The concentrations of monosaccharide

anhydrides in summer and autumn are obviously higher than that in spring and winter, while the concentrations of sugar and sugar alcohol in winter are significantly lower than in other seasons. The results of positive matrix factorization analysis suggest that saccharide compounds in atmospheric PM in Beijing are derived from biomass burning, suspended soil or dust, isoprene SOA, as well as direct release of airborne fungal spores and pollen. (Liang Linlin)

2 Model development and implementation, the impacts of atmospheric compositions on climate, weather, and human health

2.1 High-resolution monitoring, forecasting and assessment of environmental meteorology

The aerosol/chemical numerical simulation system (CUACE/Chem) was independently developed and improved, especially by the feedback mechanisms for the multi-component aerosol-radiation and aerosol-cloud-precipitation interactions, to achieve the two-way couplings of aerosols-CCN-cloud-precipitation cycles with the meteorology model. The group's environmental meteorology program contributed to four major national events, seven assessment reports for emission reduction measures, and more than 20 environmental meteorological consultation sessions, i.e., 2014 APEC event, 2015 Winter Olympics bidding preparation, and the 70th anniversary of the victory of anti-Japanese War. Among these, the assessment report for the APEC pollution control measures was read over and commented on by the General Secretary of CPC, Prime Minister and Deputy Prime Minister. To coordinate the national and regional centers for the fog and haze monitoring and forecasting operation, the group has transferred the CUACE system to the Beijing Meteorological Service to support its middle to long term (10–30 days) fog and haze forecasts and a GRAPES version of CUACE to Guangdong Meteorological Service to support its daily forecasts. The CUACE system now supports off-line nesting, arbitrary grid resolution setting and data matching technology, enabling the application of CUACE for arbitrary grid configuration and multiple-level nesting. It can meet the requirements for low, middle and high resolutions, the highest of which is of 1–3 km. (Liu Hongli)

2.2 Dispersion and transformation of hazardous materials in the atmosphere

The project “Dispersion and Transformation of Hazardous Materials in the Atmosphere” aimed at setting up a multi-scale meteorological transport and coupling model to describe the dispersion and transformation of hazardous chemicals in the atmosphere. The Urban Meteorological and Tracer Experiment, the Mobile Monitoring of Urban Air Pollutants Experiment, and the Indoor Tracer Dispersion Experiment were implemented under this project. A lot of valuable data have been obtained and the experimental methodology has been developed. The effect of boundary layer processes on the diffusion and transport of air pollutants was investigated by CFD model. The block-scale model Fluent has been coupled into the mesoscale model WRF, and the disaster alerting method has been proposed. (Ma Jianzhong)

2.3 Transport of pollutants and interaction of aerosols with PBL during a haze-fog episode

The interaction between $PM_{2.5}$ and PBL, and the contribution of particulate matter (PM) transported from surrounding regions to high $PM_{2.5}$ in Beijing were studied, the results of which demonstrate:

(1) Aerosol cools the PBL atmosphere but warms the atmosphere over it, leading to a more stable atmospheric stratification over the region, which causes a decrease in turbulence diffusion and in the PBL height. This consequently forms a positive feedback on the particle concentration at the PBL and the surface, favoring the haze formation. Additionally, aerosol direct radiative forcing (DRF) increases PBL wind speed and weakens the subtropical high, which aids the gravity of haze pollution and results in a negative feedback to

the haze episode. The synthetic impacts from the two opposite feedbacks result in an increase in surface $PM_{2.5}$. However, the persistence time of both high $PM_{2.5}$ and haze pollution is not subject to the aerosol DRF.

(2) A very closely positive correlation was found between the southerly wind speed over the plain to the south of Beijing and changes in $PM_{2.5}$ in the city, both reaching maximum values at about 900 hPa, suggesting that the lower atmosphere was the principal layer for pollutant PM transport from the neighbouring region to its south to Beijing. During haze episodes, and depending upon the period, Beijing was either a pollution source or sink for its surrounding areas. PM input from Beijing's environs was much higher than the output from the city, resulting in the most serious pollution episode, with the highest $PM_{2.5}$ value occurring from 00:00 to 10:00 UTC (08:00 to 18:00 LT), 7 December 2013. PM pollutants from the environs of the city accounted for over 50% of the maximum $PM_{2.5}$ values seen in Beijing. At other times, the Beijing area was a net contributor to pollution in its environs. (Wang Hong)

2.4 The effect of comprehensive reduction in emissions of black carbon and co-emitted species on the aerosol net cooling

The influence of removed sources of BC and other co-emitted species on the aerosol radiative effect is estimated by using an aerosol-climate atmosphere-only model BCC_AGCM2.0.1_CUACE/Aero with prescribed sea surface temperature and sea ice cover, in combination with the aerosol emissions from the Representative Concentration Pathways (RCPs) scenarios. We find that the global annual mean aerosol net cooling effect at the top of the atmosphere (TOA) will be enhanced by 0.12 W m^{-2} compared with recent year 2000 levels if the emissions of only BC are reduced to the level projected for 2100 based on the RCP2.6 scenario. This will be beneficial to the mitigation of global warming. However, both aerosol negative direct and indirect radiative effects are weakened when BC and its co-emitted species (sulfur dioxide and organic carbon) are simultaneously reduced. Relative to year 2000 levels, the global annual mean aerosol net cooling effect at the TOA will be weakened by $1.7\text{--}2.0 \text{ W m}^{-2}$ if the emissions of all these aerosols are decreased to the levels projected for 2100 in different ways based on the RCP2.6, RCP4.5, and RCP8.5 scenarios. Because there are no effective ways to remove the BC exclusively without influencing the other co-emitted components, our results therefore indicate that a reduction in BC emission can lead to an unexpected warming on the Earth's climate system in the future. (Wang Zhili)

2.5 Impact of four-stream radiative transfer algorithm on aerosol direct radiative effect and forcing

In this study, using an aerosol-climate model with two- and four-stream radiation schemes, we find that the aerosol shortwave direct radiative effects (DREs) and heating rate are underestimated significantly by the two-stream algorithm that is generally used in global climate models (GCMs). For present-day conditions, the four-stream algorithms are found to enhance global annual mean aerosol shortwave DREs by more than 8% (14%) at the top of the atmosphere (TOA), 15% (18%) in the atmosphere, and 12% (15%) at the surface in an all-sky (clear-sky) case. The DRE differences due to the four-stream algorithms are negative, except for the Arctic, Tibetan Plateau, Arabia, and Sahara, at the TOA, are positive in the atmosphere, and are negative at the surface, with the maximum exceeding 4.0 W m^{-2} . Increases in the aerosol shortwave heating rate due to the four-stream algorithms are generally more than 10% and may even exceed 100%. Our results also show that the two-stream algorithm underestimates the direct radiative forcings (DRFs) due to anthropogenic aerosols. Significant underestimation appears in the middle latitudes of the Northern Hemisphere, with the maximum being close to the quantity of 0.6 W m^{-2} in a clear-sky case. This study indicates that a multi-stream radiative transfer algorithm is necessary to reduce the uncertainties of aerosol DREs and DRFs estimated by GCMs. (Wang Zhili)

2.6 Study on inverse modeling of black carbon emissions over China using ensemble data assimilation

Emission inventories of black carbon (BC), which are traditionally constructed using a “bottom-up” approach based on activity data and emission factors, are considered to contain a large level of uncertainty. In our study this year, an ensemble optimal interpolation (EnOI) data assimilation technique was used to investigate the possibility of optimally recovering the spatially resolved emission bias of BC. An inverse modeling system for emissions was established for an atmospheric chemistry aerosol model and two key problems related to ensemble data assimilation in the top-down emission estimation were discussed. The emission sampling strategy was improved with an additional temporal correlation component, so that an ensemble forecast had a larger spread to include the observations. The effect of localization in the analysis was also studied. With reasonable localization, the effects of sample errors and spurious correlations are reduced. An experiment involving one year long simulation cycle with EnOI inversion of BC emissions was performed for 2008. The bias of the BC emission intensity in China at each grid point was corrected by this inverse system. The inversed emission over China in January is 240.1 Gg, and annual emission is about 2539.3 Gg, which is about 1.8 times of the bottom-up emission inventory. We also conducted the Monte Carlo simulation to quantify the uncertainty of the total bottom-up emission and the inversed emission inventory in China. The uncertainties of the bottom-up and inversed emission inventory are about $[-80\%, 227\%]$, and $[-58, 102\%]$. The results show that, even though only monthly mean BC measurements are employed to inverse the emissions, the accuracy of the daily model simulation improves. Using top-down emissions, the average root-mean-square error of simulated daily BC is decreased by nearly 30%. These results are valuable and promising for a better understanding of aerosol emissions and distributions, as well as for aerosol forecasting. (Wang Ping)

2.7 Construction of GRAPES-CUACE adjoint model

Compiling, assembling and testing the tangent linearity and the adjoint model of CUACE, writing and testing the interface program code between GRAPES and CUACE, and extracting, constructing and testing the code related with the chemical species transport process in GRAPES-Meso have been completed. The GRAPES-CUACE adjoint model simulated the sensitivity of concentration of emission and was adopted to track the most influential emission-source regions and most influential time intervals for the high BC concentration. Four types of regions were selected and compared based on administrative jurisdiction and adjoint sensitivity coefficient distribution. Effects of different emission reduction strategies based on adjoint sensitivity information show that the more influential regions (those with relatively larger sensitivity coefficients) do not necessarily correspond to the administrative regions, and the influence per unit area of sensitivity-based regions was greater than that of administrative jurisdictions. The influence of emissions on the objective function decreases sharply when pollutants are emitted 17–18 h previous to the objective time point. Therefore, controlling critical emission regions during critical time intervals on the basis of an adjoint sensitivity analysis is much more efficient than controlling administratively specified regions as shown during an experiential time period (Fig. 6). (An Xingqin)

2.8 Inverse modeling of SO₂ and NO_x emissions using an adaptive nudging scheme implemented in CMAQ model in North China during heavy haze episodes in January 2013

In this study, the SO₂ and NO_x emission sources in North China during a heavy haze episode in January 2013 were retrieved using an adaptive nudging scheme implemented in the Community Multiscale Air Quality (CMAQ) modeling system, based on the 2006 INTEX-B emission inventory. SO₂ and NO₂ concentrations during two sustaining heavy haze episodes occurring on January 9–15 and 28–31 were simulated using

the Weather Research Forecasting (WRF)-CMAQ model system with the above initial emission inventory (INTEX-B for 2006) and the improved emission estimate (inversed for January 2013), respectively. Simulated results were compared with the observations at 47 stations from the China National Environmental Monitoring Centre (CNEMC), and the difference caused by the two emission estimates and the advantage of nudging source over the initial emission inventory were analyzed. Reasonability and reliability of inversed SO_2 and NO_x emissions were evaluated using the 2012 MEIC emission inventory developed by the Tsinghua University (MEIC v1.2 inventory). It is shown that (1) the adaptive nudging scheme based on CMAQ model is suitable for simulating heavy haze pollution processes. Namely, the temporal and spatial variation characteristics of simulated SO_2 and NO_2 concentrations are consistent with those of observations, and the dynamic variation characteristics of SO_2 and NO_x emission sources are also captured. (2) An inversed source is obviously superior to the initial 2006 INTEX-B emission inventory for the simulation of SO_2 and NO_2 concentrations. The temporal variation trends of SO_2 and NO_2 , including their peak values, during the heavy haze pollution episodes are well simulated with the former, which is in a better agreement with the observations. (3) The regional SO_2 and NO_2 distributions simulated by inverting emission sources are in accordance with the observations, with the extreme values in heavily polluted areas being well reproduced. (4) Correlation coefficients between the simulated and observed concentrations of SO_2 and NO_2 increase and biases decrease using the inversed emissions compared to the initial emissions. There are more improvements in the simulation of SO_2 than NO_2 due to different impacts of emission sources on the concentrations of these two pollutants. (5) Differences in the spatial distribution and intensity of SO_2 and NO_x emission sources between the initial emission estimate and the MEIC v1.2 inventory are larger, whereas the results with the inversed emission sources are close to those with the MEIC v1.2 inventory, with high emission source intensity of SO_2 and NO_2 in the key areas being inversed. The results of this study will provide a new technique and idea for improving air quality forecasting during heavy haze pollution episodes, reducing the uncertainties in the emission inventory developed with the bottom-up approach, and assessing the impacts and dynamic control of regional SO_2 and NO_x emission sources under different weather conditions. (Cheng Xinghong)

2.9 Dynamical-statistical forecasting of $\text{PM}_{2.5}$ concentration based on CMAQ model and self-adapting partial least square regression method in China

In this study, hourly $\text{PM}_{2.5}$ concentrations at 252 environmental monitoring stations in China during January–December 2014 forecasted by the real-time running Fifth-Generation Penn State/NCAR Mesoscale Model (MM5)-Community Multiscale Air Quality (CMAQ) model system were corrected using the dynamical-statistical method based on CMAQ model and self-adapting partial least square regression technique. Temporal and spatial variation characteristics of $\text{PM}_{2.5}$ concentrations before and after correction were analyzed with a focus on the applicability of the dynamical-statistical method in different areas and seasons in China. It is shown that (1) the spatial distributions of both the yearly and seasonal (for autumn and winter) averages of $\text{PM}_{2.5}$ concentrations forecasted by the MM5-CMAQ model system are inhomogeneous. Namely forecasted $\text{PM}_{2.5}$ concentrations are larger than observations in parts of Liaoning and Shandong provinces, in Sichuan and Chongqing provinces and in most areas of Central China, East China and South China, whereas forecasting values are smaller in Beijing-Tianjin-Hebei region and in most areas of western China. After correction, the spatial distributions of forecasted $\text{PM}_{2.5}$ concentrations are in good consistence with observations, and forecasting errors in the above areas decrease obviously. Forecasting and corrected deviations of seasonally averaged $\text{PM}_{2.5}$ concentrations in autumn and winter in most areas of China are both larger than those of the yearly averaged values. (2) There is an obviously seasonal variation characteristic for the national average of observed $\text{PM}_{2.5}$ concentrations. Namely, observational values are larger in Jan., Feb., Mar., Nov. and Dec. than

in other months. Forecasting errors are larger, with prediction values being less than observations in most of the time, especially in Jan., Feb., Mar., Nov. and Dec. Corrected $PM_{2.5}$ concentrations and its temporal variation tendency are close to observations. Forecasting and corrected deviations in autumn and winter are larger than those in spring and summer. (3) During autumn and winter, among the four seriously polluted regions in China, the regional average of observed $PM_{2.5}$ concentrations in the Beijing-Tianjin-Hebei region is highest, Sichuan and Chongqing provinces take second place, and the lower values are found in the Yangtze River and Pearl River Delta regions. However, the forecasting and correction effects are best in the Pearl River Delta region, followed by Sichuan and Chongqing provinces and Yangtze River Delta region, and relatively worse in the Beijing-Tianjin-Hebei region. After corrections, correlation coefficients between corrected $PM_{2.5}$ concentrations and observations increase remarkably, and forecasting errors decrease obviously, especially for autumn and winter. (4) Error decreasing ratios after correction are largest in Sichuan and Chongqing provinces, followed by the Yangtze River Delta region and Beijing-Tianjin-Hebei region, and are relatively smaller in the Pearl River Delta region. (5) The method presented in this paper is applicable to the correction of $PM_{2.5}$ forecasted concentrations in both polluted and clean days in China. It is more effective for the correction of $PM_{2.5}$ forecasted concentrations during polluted processes in the Beijing-Tianjin-Hebei region, and correction effects are better during clean processes than in polluted days in other three regions. Results of this study will provide a new technique and scientific basis for improving air quality forecasting, early warning and prevention of heavy haze weather. (Cheng Xinghong)

消息与动态 News and Notes



2015年1月9日，中国气象局局长郑国光、副局长宇如聪等领导到气科院调研指导气象现代化建设和深化气象科技体制改革试点工作。郑国光局长一行听取了端义宏院长的专题汇报，并与气科院领导班子成员以及院各科研机构的主要负责人进行了交流研讨。

On 9 January 2015, CMA leaders including the Administrator, Dr. Zheng Guoguang, and the Deputy Administrator, Dr. Yu Rucong, etc, visited CAMS to study and provide guidance to the development of meteorological modernization and enhancing the pilot reform of scientific and technological mechanism. Dr. Zheng listened to the dedicated report given by Dr. Duan Yihong, CAMS President. Discussion and exchange of ideas were held among the CMA leaders, CAMS management group, as well as heads of relevant CAMS research units.

2015年1月4日，生态环境与农业气象研究所学术沙龙第6期举行。赵俊芳博士汇报了赴美国密苏里大学为期1年的访问交流情况，周莉博士汇报了赴澳大利亚为期3周的气象业务培训情况。所长郭建平主持了学术沙龙。

On 4 January 2015, the Sixth Academic Saloon of CAMS Institute of Ecological Environment and Agricultural Meteorology was held, during which Dr. Zhao Junfang and Dr. Zhou Li gave their respective reports on the outcomes of one-year academic visit to University of Missouri and three-week meteorological training in Australia. Head of the Institute, Guo Jianping chaired the saloon.





2015年1月12—13日，气科院2014年度学术年会在北京召开。年会特邀了秦大河院士、王建捷研究员、朱彤教授、杨修群教授、黄建平教授分别做了专题报告，年会还包括灾害性天气、云雾物理和探测、农业气象、气候、大气成分和城市气象研究等5个分会场，100多位科研人员进行了学术交流。

On 12–13 January 2015, the 2014 Annual Academic Meeting of CAMS was held in Beijing. Scientists including Academician Qin Dahe, Researcher Wang Jianjie, Profs. Zhu Tong, Yang Xiuqun and Huang Jianping were invited to give themed reports. The annual meeting also covered topics on severe weather, cloud physics and sounding, agrometeorology, climate, atmospheric composition as well as urban meteorology research in five sub-sessions, which were attended by over 100 research staff carrying out academic exchanges.



2015年1月15日，在中国气象局计划财务司司长谢璞的陪同下，国家发展和改革委员会农村经济司司长吴晓一行访问中国气象局人工影响天气中心。李集明主任和周毓荃研究员为来宾简要介绍了人工影响天气的基本原理、业务系统和作业实施过程等情况。

On 15 January 2015, Director-General of Department of Rural Economy, National Development and Reform Commission (NDRC), Mr. Wu Xiao and his colleagues visited CMA Weather Modification Centre, accompanied by Mr. Xie Pu, Director-General of CMA Department of Planning and Finance. Director-General of Weather Modification Centre, Mr. Li Jiming and Researcher Zhou Yuquan introduced the basic working principles, operational systems and operation processes of weather modification.

INTERNATIONAL WORKSHOP ON HIGH IMPACT WEATHER RESEARCH

Ningbo, 20-23 January, 2015



2015年1月20—23日，灾害天气国家重点实验室与世界气象组织（WMO）在浙江省宁波市联合举办了“高影响天气研究国际研讨会”，来自美国、印度、菲律宾、孟加拉国以及国内的专家学者110余人参加了会议，会议共收到论文120余篇。会议的组织得到WMO的高度肯定。

On 20–23 January 2015, CAMS State Key Laboratory on Severe Weather (LaSW) and World Meteorological Organization (WMO) jointly held “International Workshop on High-Impact Weather Research”, which was attended by over 110 domestic and overseas experts or scholars from countries such as US, India, Philippines, Bengal, with more than 120 submitted papers. The organizing of the workshop was highly acknowledged by WMO.



2015年1月30日，气科院召开2014年度领导班子述职述廉述学暨2015年工作会议。会上，院长端义宏全面总结了2014年气科院在科技创新等方面取得的可喜成果，并对2015年气科院深化体制机制改革、推进气象现代化建设、促进科研成果转化等重点工作进行了部署。

On 30 January 2015, CAMS held its 2014 Annual Meeting of Management Group Reporting Working Performance and Incorruptibility, i.e. the 2015 Annual Meeting of Work. President of CAMS, Dr. DuanYihong, reviewed the highlights of CAMS in 2014 such as scientific and technical innovation, etc. He also confirmed the key working areas of CAMS in 2015, including enhancing reforms of systems and mechanisms, advancing meteorological modernization, and promoting research outcome transformation, etc.



2015年3月11日，矫梅燕副局长到中国气象局人工影响天气中心调研指导工作。人工影响天气中心主任李集明汇报了“全国人工影响天气业务能力建设三年行动计划”的主要内容。矫梅燕副局长希望，通过实施“三年行动计划”，全国人工影响天气业务能力迈上一个新台阶。

On 11 March 2015, CMA Deputy Administrator, Ms. Jiao Meiyuan, visited CMA Weather Modification Centre to provide guidance. Director-General of Weather Modification Centre, Mr. Li Jiming, reported the main contents of the Three-Year Action Plan of National Weather Modification Operation Capacity Building. Ms. Jiao expressed her hope that the operation capability of national weather modification develops to a higher level through this “Three-Year Action Plan”.



2015年4月10日，气科院召开第3次青藏高原大气科学试验2015年度工作会议。项目专家指导组成员和各子项目组成员出席会议，会议由项目首席科学家赵平研究员主持。会议在总结评估2014年度试验情况的基础上，提出并讨论了各项目2015年的工作计划。

On 10 April 2015, CAMS held its 2015 Annual Meeting for “the Third Tibetan Plateau Scientific Experiment on Atmosphere”. Members of the project expert steering group and sub-projects group attended the meeting, which was presided over by the project chief scientist,

Researcher Zhao Ping. The meeting summarized and reviewed the experiments carried out in 2014, on the basis of which working plans for each sub-project in 2015 were presented and discussed.

2015年4月14日，成都信息工程大学周激流校长一行7人赴气科院调研。院长端义宏主持座谈会。双方就建立长效合作机制和开展深层次合作等问题进行了讨论。

On 14 April 2015, President of Chengdu University of Information Technology (CUIT), Mr. Zhou Jiliu, with six of his colleagues, visited CAMS. President of CAMS, Dr. DuanYihong, hosted the discussion, during which ideas of establishing long-term collaboration and deepening cooperation were exchanged.



2015年4月21日，中国地震局工程力学研究所副所长李明一行7人赴气科院调研，就如何提高科技创新能力和社会服务能力等问题与气科院相关领导及专家展开座谈，周广胜副院长接待并主持会议。

On 21 April 2015, Vice President of Institute of Engineering Mechanics, China Earthquake Administration, Mr. Li Ming, with six of his colleagues, visited CAMS and discussed with both leaders and experts of CAMS about how to improve the capability of scientific and technological innovation, as well as social service. The discussion was presided over by Vice President of CAMS, Mr. Zhou Guangsheng.

2015年4月14日至5月10日，气科院极地气象研究所丁明虎副研究员和魏婷助理研究员赴北极黄河站开展野外考察，并完成了2015年度北极黄河站大气和空间环境综合观测任务。

From 14 April to 10 May 2015, Associate Researcher, Ding Minghu and Research Assistant, Wei Ting from CAMS Institute of Polar Meteorology, carried out scientific expedition at Chinese Arctic Yellow River Station and completed the integrated observation of atmosphere and space environment at the station for the year of 2015.





2015年4月29日，国家重点基础研究发展计划（973计划）项目“登陆台风精细结构的观测、预报与影响评估”启动会在北京召开。科技部领域专家咨询组、项目专家组、各课题负责人及骨干成员40余人参加了会议，项目首席科学家端义宏研究员主持会议并介绍了项目的基本情况。

On 29 April 2015, the launching meeting of National Basic Research Program of China (973 Program), “Monitoring and Forecasting of Finescale Structure and Impact Assessment of Landfalling Typhoons” was held in Beijing. Over 40 members attended the meeting,

including those from the specialized expert advisory group of Ministry of Science and Technology (MOST), project expert group, task team leaders and cadres, etc. project chief scientist, Researcher Duan Yihong presided over the meeting and introduced the project.



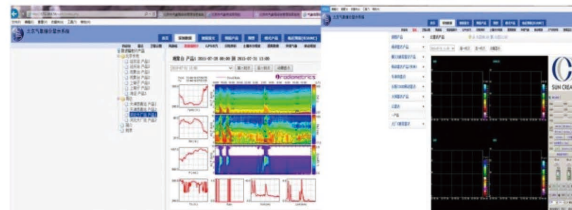
应急观测保障演练视频连线



微波辐射计



云雷达



微波辐射计产品截图

云雷达产品截图

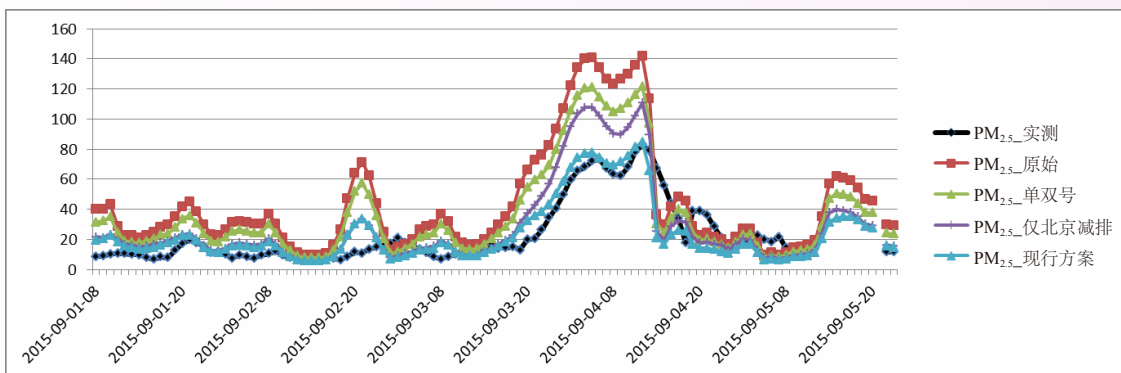
2015年6月10日，气科院启动了配合北京市气象局9月的重大纪念活动应急观测保障工作，气科院的云雷达和微波辐射计在7月28—29日第1次应急观测保障演练中表现良好。气科院的雷达专家刘黎平研究员和人工影响天气专家苏正军还对有关人员进行了专门的培训。

On 10 June 2015, CAMS launched its emergency observation supporting the meteorological service by Beijing Meteorological Service for significant memorial events in September of the year. The performance of CAMS’ cloud radar and microwave radiometer was satisfactory in the first drill of emergency observation service on 28–29 July. Researcher Liu Liping, CAMS radar expert, and Su Zhengjun, CAMS weather modification expert, trained the operation staff.



2015年7月23日下午，气科院召开全面深化科技体制改革启动会。院长端义宏主持会议，中国气象局副局长于新文、科技与气候变化司司长罗云峰、人事司副司长于玉斌、改革办副主任庞鸿魁及全院职工参加了会议。

On the afternoon of 23 July 2015, CAMS held its meeting that marked the launching of overall enhancement of scientific and technological system reform, which was chaired by CAMS President, Dr. Duan Yihong. CMA Deputy Administrator, Mr. Yu Xinwen; Director-General of CMA Department of Science & Technology and Climate Change, Mr. Luo Yunfeng; Deputy Director-General of CMA Department of Human Resource, Mr. Yu Yubin; Deputy Director-General of CMA Reform Office, Mr. Pang Hongkui, as well as the entire CAMS staff, attended the meeting.



受北京气候中心邀请，气科院在2015年6—8月全程参与了北京世锦赛及庆典活动期间的气候预测工作，利用CFS-CUACE模式预测8月下旬至9月上旬的天气和雾-霾情况。同时，为北京气候中心移植安装了CUACE模式的中长期预测版本。自2015年8月27日开始，提前7天准确预报了庆典期间的优良天气，并提出了不必采取过度减排的建议措施。

At the invitation of Beijing Climate Centre, CAMS participated in the entire meteorological supporting process during June-August 2015 and forecasted the climate and haze occurrences for late August and early September with CFS-CUACE model during the Beijing IAAF World Championships. At the same time, the forecasting system CFS-CUACE was transferred to the centre for its long term forecasting services. Starting from 27 August 2015, CAMS forecasted good visibility seven days ahead of the event and suggested a less controlled measure to be taken.

Contact:
 Name: Prof. Zhai Panmao
 Date of birth: May 5, 1962
 Nationality: Chinese
 Affiliation: Chinese Academy of Meteorological Sciences
 China Meteorological Administration (CMA)
 46 Zhongguancun Haidian Beijing 100080, China
 166-016640602
 Email: pmao@cma.gov.cn

Education:
 09/1987-07/1990, Major in Physical climatology, Graduate School, Nanjing University
 09/1990-07/1994, Major in Climatology, Department of Atmospheric Sciences, Nanjing University

Intergovernmental Panel on Climate Change (IPCC):
 2008-2015, Lead Author, WGI, IPCC AR5
 2003-2007, Lead Author, WGI, IPCC AR4
 1998-2001, Contributing Author, WGI, IPCC TAR



**CANDIDATE OF CHINA FOR IPCC
WGI CO-CHAIR
ZHAI Panmao**
pmao@cma.gov.cn

"Climate change is rapidly advancing science, it is of great concern to both general public and policymakers. I am determined to devote myself to the assessment of the latest research findings to keep the broader community informed of the changing climate in an objective and clear manner."

Professional Information

- ▶ Secretary-General, Chinese Meteorological Society
- ▶ Professor, Ph.D. supervisor, and Vice president, Chinese Academy of Meteorological Sciences
- ▶ Adjunct Professor, Ph.D. supervisor, Nanjing University of Information Science & Technology
- ▶ Director-General, Department of Forecasting and Networking, China Meteorological Administration (CMA)
- ▶ Chief Scientist, National Basic Research Programme (973 Programme) of China
- ▶ Visiting scientist in NCAR, USMC, and Meteorological Service of Canada
- ▶ Over 100 peer-reviewed publications, and 3 monographs
- ▶ First Prize for National Scientific and Technological Progress of China

Services to IPCC and WMO

- ▶ Lead author, WGI, IPCC AR4 and AR5, contributing author, WGI, IPCC TAR
- ▶ Co-chair, WMO CO-CHAD on Monitoring and Analysis of Climate Variability and Change (November 2005 - November 2005)
- ▶ Co-leader, WMO CAGM Implementation/Coordination Team on Climate Change/Variability and Natural Disasters in Agriculture (October 2008 - July 2010)
- ▶ Co-leader, WMO CO-Task Team on the Definition of Extreme Weather and Climate Events (July 2014 -)



2015年10月5—8日，政府间气候变化专门委员会（IPCC）第42次全会在克罗地亚杜布罗夫尼克召开，在此次会议上气科院研究员翟盘茂高票当选IPCC第1工作组联合主席。翟盘茂研究员曾在世界气象组织多个专家组担任领导职位，并作为主要作者参加过第4次和第5次IPCC第1工作组评估报告的编写。

On 5–8 October 2015, the 42th Plenary Session of Intergovernmental Panel on Climate Change (IPCC) was held in Dubrovnik, Croatia, during which CAMS Researcher Zhai Panmao was elected Co-chair of First Working Group of IPCC with the biggest number of votes. Dr. Zhai used to take leader's position in several WMO expert groups and he also participated in writing the Fourth and Fifth Assessment Reports of IPCC First Working Group as a core writer.



2015年9月8—9日，气科院和广东省气象局在广州市联合举办了“2015年雷电科学研讨会暨广东闪电综合观测试验10年总结会议”。气科院院长端义宏、广州市气象局局长梁建茵和国家自然科学基金委张朝林处长等领导出席会议，来自美国、日本以及国内几十家单位的科研业务人员参加了研讨会。

On 8-9 September 2015, CAMS and Guangdong Provincial Meteorological Service jointly held the “2015 Scientific Workshop on Lightning, i.e. the Summing-up Meeting of the Ten-Year Integrated Lightning Observation Experiment of Guangdong”. CAMS President, Dr. Duan Yihong, Director-General of Guangzhou Meteorological Service, Mr. Liang Jianyin and Director from National Science Foundation of China (NSFC), Mr. Zhang Chaoliln, etc, attended the activity. Experts from US, Japan as well as several research institutes in China also participated in the workshop.



2015年10月27日，浙江省气象局副局长王东法一行6人就核心业务技术对接到气科院调研，副院长李集明主持交流会。双方分别介绍了各自承担的核心攻关任务、重点研究领域和存在的关键技术难题，并就核心业务技术合作展开了深入的交流。

On 27 October 2015, Deputy Director-General of Zhejiang Provincial Meteorological Service, Mr. Wang Dongfa and five of his colleagues visited CAMS to

exchange ideas on core operation technologies. Vice President of CAMS, Mr. Li Jiming chaired the discussion. The two sides introduced their respective core tasks, key research areas as well as technical difficulties and exchanged ideas on potential cooperation in core technologies.

2015年10月28日，中国气象局气象干部培训学院河北分院院长张书余一行3人来到气科院调研，双方就环境气象基础理论课程、数值预报模式课程的授课教师和教材编写等事宜进行了研讨。周广胜副院长主持了交流会。

On 28 October 2015, President of Hebei Training Centre subordinating to the CMA Training Centre, Mr. Zhang Shuyu, with two of his colleagues, visited CAMS. The two sides exchanged ideas about the teachers and teaching materials for courses on basic theories of meteorology and NWP models. The discussion was chaired by Vice President of CAMS, Mr. Zhou Guangsheng.



2015年11月4日，2015年度何梁何利基金颁奖大会在京举行，气科院徐祥德院士（右二）荣获何梁何利“科学与技术进步奖”。徐祥德院士长期从事天气动力与气候动力学、城市环境等研究，先后承担了多项国家重大科研项目并多次主持了大气科学研究试验。

On 4 November 2015, the Awarding Ceremony of 2015 Annual Ho Leung Ho Lee Foundation was held in Beijing. Academician Xu Xiangde (the second person from the right) from CAMS won the “Scientific and

Technological Advancement Award” of this fund. Over many years, Dr. Xu has been engaged in the research of weather and climate dynamics, urban environment, etc, who has taken over a number of national key research projects and chaired several experiment in atmospheric science.

2015年11月，第16届（2014—2015年度）涂长望青年气象科技奖评选结果揭晓，气科院气候系统研究所副研究员陈昊明博士喜获二等奖。陈昊明对东亚区域云雨特征进行了较为系统的研究，并得到了一些有意义的结论，先后发表论文26篇，其中SCI论文18篇。

In November 2015, the 16th (2014–2015) Tu Changwang Youth Meteorological S&T Award announced the winners.

Dr. Chen Haoming, Associate Researcher of CAMS Institute of Climate Systems won a second prize. Dr. Chen has carried out systematic research on features of cloud and rain over East Asia and achieved significant results. 26 of his papers were published, among which 18 were accepted by SCI.



2015年12月2日，院长端义宏主持座谈，与到访的南京信息工程大学校长蒋建清就推进落实气科院与南京信息工程大学核心攻关任务合作计划事宜展开研讨。双方希望通过在核心攻关技术方面的合作，实现优势互补，取得教学和科研方面的新突破。

On 2 December 2015, CAMS President, Dr. Duan Yihong hosted the discussion at CAMS with Mr. Jiang Jianqing, President of Nanjing University of Information Technology (NUIST), about promoting and implementing the cooperation plan between CAMS and NUIST in core tasks. Both sides expressed their hope of complementing each other's advantage through the cooperation in solving key technologies and achieving further breakthroughs in teaching and research.



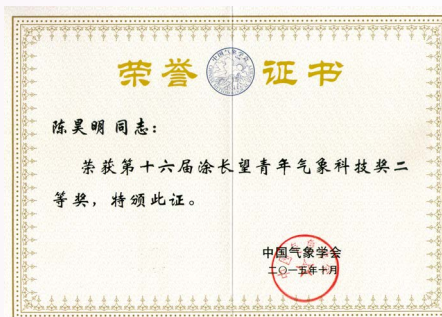
2015年12月14日，中国气象局党组书记、局长郑国光，副局长宇如聪到气科院调研，了解气科院推进改革的进展，与气科院的领导、专家共同研究灾害天气国家重点实验室未来发展。郑国光希望气科院通过深化体制机制改革，发挥气科院在科技引领创新驱动发展中的主力军作用。

On 14 December 2015, CMA Administrator and Secretary of CPC Party Committee, Dr. Zheng Guoguang, and CMA Deputy Administrator, Dr. Yu Rucong came to CAMS to see the progress of its reform and discussed with CAMS leaders and experts about the future development of State Key Laboratory on Severe Weather (LaSW). Dr. Zheng expressed his hope that CAMS takes its leading role in the S&T innovation and make expected contributions through the enhanced system and mechanism reform.



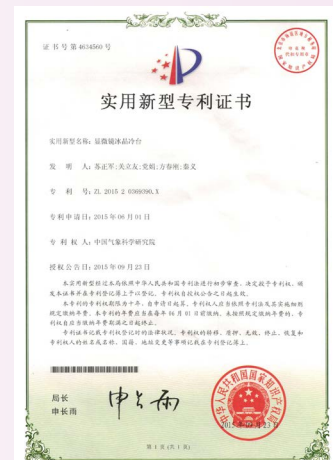
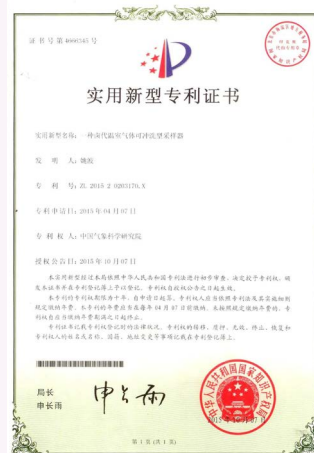
2015年12月22日，在中国气象局副局长于新文的陪同下，国务院发展研究中心副主任王一鸣一行到气科院调研。气科院院长端义宏主持接待。大气成分研究所副所长王亚强向来宾介绍了大气成分观测、雾霾数值预报系统的研发及其对雾-霾预报业务的支撑情况。

On 22 December 2015, accompanied by CMA Deputy Administrator, Mr. Yu Xinwen, the Vice Minister of Development Research Centre of China's State Council, Mr. Wang Yiming visited CAMS. President of CAMS, Dr. Duan Yihong received the guests. Deputy Director of CAMS Institute of Atmospheric Composition, Dr. Wang Yaqiang, introduced atmospheric composition observation, fog & haze NWP system development and its supports to fog & haze operational forecasts.



2015年，气科院获何梁何利科技进步奖1项、教育部科技进步一等奖1项、中国气象学会科技进步二等奖3项、中国颗粒学会青年科学家奖1项、浙江省科技进步二等奖1项，获国家专利6项。

In the entire year of 2015, CAMS won a S&T Advancement Award in Ho Leung Ho Lee Foundation, a first prize of S&T Advancement awarded by Ministry of Education, three second prizes of S&T Advancement awarded by Chinese Meteorological Society, a Young Scientist Award given by Chinese Society of Particology, a second prize of Zhejiang Provincial S&T Advancement, and 6 national patents.



2015年，气科院获何梁何利科技进步奖1项、教育部科技进步一等奖1项、中国气象学会科技进步二等奖3项、中国颗粒学会青年科学家奖1项、浙江省科技进步二等奖1项，获国家专利6项。

In the entire year of 2015, CAMS won a S&T Advancement Award in Ho Leung Ho Lee Foundation, a first prize of S&T Advancement awarded by Ministry of Education, three second prizes of S&T Advancement awarded by Chinese Meteorological Society, a Young Scientist Award given by Chinese Society of Particurology, a second prize of Zhejiang Provincial S&T Advancemen, and 6 national patents.



2015 年新项目
New Projects in 2015

课题名称 Title	项目类别 Project/Fund	执行期间 Duration	负责人 Principal Investigator
东北玉米积温稳定性及应用技术研究 A technical study on corn accumulated temperature stability and application in Northeast China	基金委：面上项目 NSFC: general program	2016—2019	郭建平 Guo Jianping
青藏高原土壤水分影响我国东部夏季降水的时空尺度 Spatial-temporal impact of soil moisture over the Tibetan Plateau on the summer monsoon rainfall in eastern China	基金委：青年科学基金项目 NSFC: youth program	2016—2018	吴辉 Wu Hui
青藏高原东南缘典型农田和森林下垫面关键陆面物理过程研究 Studies on key land surface processes over typical cropland and forests on southeastern Tibetan Plateau	基金委：青年科学基金项目 NSFC: youth program	2016—2018	张果 Zhang Guo
4—5 月南亚高压形态变化对 ENSO 的响应及其对南亚夏季风爆发的调控 The reshaping South Asian high in response to ENSO and its regulation of the South Asian summer monsoon onset in April–May	基金委：青年科学基金项目 NSFC: youth program	2016—2018	刘伯奇 Liu Boqi
中高纬外强迫因子对夏季欧亚中高纬度阻塞环流的协同影响机理 Impact of multiple external forcings over the mid-high latitudes on the summer Eurasian blocking circulation	基金委：青年科学基金项目 NSFC: youth program	2016—2018	张若楠 Zhang Ruonan
基于高分辨率云解析模式结果评估改进气候模式对云雨过程的模拟 Improve the simulation of cloud and precipitation by climate models based on cloud-resolving models	基金委：青年科学基金项目 NSFC: youth program	2016—2018	张祎 Zhang Yi
国际贸易中的转移排放对气候和环境影响的模拟研究 Modeling the impact of transfer emissions via international trade on climate and environment	基金委：青年科学基金项目 NSFC: youth program	2016—2018	魏婷 Wei Ting
复杂陆面过程模型的参数不确定性量化研究 Quantification of complex land surface models in parametric uncertainty	基金委：青年科学基金项目 NSFC: youth program	2016—2018	甘衍军 Gan Yanjun
气候变化对作物产量影响的不确定性研究 Uncertainty in simulating crop yields under climate change	基金委：青年科学基金项目 NSFC: youth program	2016—2018	张祎 Zhang Yi
华北地区二氧化硫日变化特征及其与霾爆发性增长的关系研究 The diurnal variation of sulfur dioxide and its relationship with the explosive growth of haze in North China	基金委：青年科学基金项目 NSFC: youth program	2016—2018	徐婉筠 Xu Wanyun

课题名称 Title	项目类别 Project/Fund	执行期间 Duration	负责人 Principal Investigator
气相色谱-热传导检测器法高精度测定大气 O ₂ /N ₂ 变化研究 Study on measuring changes in the atmospheric O ₂ /N ₂ by a high-precision gas chromatograph-thermal conductivity detector	基金委: 青年科学基金项目 NSFC: youth program	2016—2018	张根 Zhang Gen
大气本底站 CO ₂ 观测浓度的源汇区域代表性研究 Track source and sink areas of observed CO ₂ concentration at atmospheric background stations	基金委: 青年科学基金项目 NSFC: youth program	2016—2018	程巳阳 Cheng Siyang
“三重季风”背景下青藏高原东坡雨季 MCS 三维结构的卫星观测分析及诊断研究 Satellite observation-based analysis and diagnosis of the three dimensional structure of MCS over the eastern slope of the Tibetan Plateau under the “triple monsoons”	基金委: 面上项目 NSFC: general program	2016—2019	胡亮 Hu Liang
热带外地区异常波动传播对东亚夏季风环流影响机理 Impact of Rossby wave propagation over extratropical regions on East Asian summer monsoon circulation	基金委: 面上项目 NSFC: general program	2016—2019	王亚非 Wang Yafei
南海季风槽内热带气旋生成机理研究 Research on the mechanism of tropical cyclogenesis in the South China Sea monsoon trough	基金委: 面上项目 NSFC: general program	2016—2019	张胜军 Zhang Shengjun
中国降水持续性结构变化及其原因研究 Observed change in and its related causes for precipitation persistency structure in China	基金委: 面上项目 NSFC: general program	2016—2019	翟盘茂 Zhai Panmao
球面阴阳网格高阶离散守恒算法研究 A study on the high-order discretization and conservation scheme on the spherical Yin-Yang grid	基金委: 面上项目 NSFC: general program	2016—2019	彭新东 Peng Xindong
基于多站大气浓度观测的我国氢氟碳化物排放量及源强分布反演研究 Study on inverse modeling of Chinese hydrofluorocarbon emissions and source strength distributions based on observed atmospheric concentration at multiple sites	基金委: 面上项目 NSFC: general program	2016—2019	姚波 Yao Bo
东亚季风系统对过去和未来人为气溶胶排放变化响应的模拟研究 Modeling study on the response of East Asian monsoon system to changes in anthropogenic aerosol emissions in the past and future	基金委: 面上项目 NSFC: general program	2016—2019	王志立 Wang Zhili
基于伴随模式的大气污染优化控制方法研究 Research on optimal control of air pollution based on the adjoint model	基金委: 面上项目 NSFC: general program	2016—2019	安兴琴 An Xingqin



课题名称 Title	项目类别 Project/Fund	执行期间 Duration	负责人 Principal Investigator
基于多源卫星观测和精细化数值模式的云辐射过程研究 Cloud radiation study based on multiple satellite observations and high resolution numerical models	基金委：重点项目 NSFC: key program	2016—2020	王宏 Wang Hong
青藏高原 UTLS 气溶胶层形成机制及火山爆发影响的数值模拟研究 Model-based simulation of the formation of aerosols and the volcanic eruption effect on UTLS aerosol layer over the Tibetan Plateau	基金委：重点项目 NSFC: key program	2016—2018	马建中 Ma Jianzhong
青藏高原闪电活动与对流云结构的关系研究 Study on relationship between lightning activity and convective cloud structure in Qinghai-Tibet Plateau	基金委：重点项目 NSFC: key program	2016—2019	张义军 Zhang Yijun
青藏高原陆面过程参数化的不确定性及其对高原地-气耦合作用的影响 Uncertainties in land-surface modeling over Tibetan Plateau and their impacts on land-atmosphere interaction	基金委：重点项目 NSFC: key program	2016—2019	陈飞 Chen Fei
夏季南亚高压区臭氧和水汽的时空变化以及向平流层输送的物质通量 Temporal and spatial variations of ozone and water vapor and transport of mass flux to the stratosphere in the summer South Asia high	基金委：重点项目 NSFC: key program	2016—2019	刘煜 Liu Yu
公里尺度大气边界层湍流参数化研究 Research on parameterization of atmospheric boundary turbulence at kilometer scale	人事部：留学回国人员基金项目 SHRM: scientific research foundation for returned Chinese scholars	2015—2015	郑永骏 Zheng Yongjun
雷击建筑物过程中先导连接行为的观测和研究 Observation of and study on the connecting behavior of the leaders in the lightning flashes terminating on tall structures	人事部：留学回国人员基金项目 SHRM: scientific research foundation for returned Chinese scholars	2015—2016	吕伟涛 Lü Weitao
天气雷达数据分级质量控制关键技术研究 Development of key technology for graded quality control of weather radar data	中国气象局：行业专项 CMA: special fund for meteorological service	2015—2017	王改利 Wang Gaili
温室气体观测分析及比对校验集成技术 Greenhouse gases observation, analysis, inter-comparison, calibration and integration techniques	科技部：国际合作与交流项目 MOST: projects of international cooperation and exchanges	2015—2017	周凌晞 Zhou Lingxi
登陆台风精细结构的观测、预报与影响评估 Monitoring and forecasting of finescale structure and impact assessment of landfalling typhoons	科技部：973 课题 MOST: national basic research program	2015—2019	端义宏 Duan Yihong

课题名称 Title	项目类别 Project/Fund	执行期间 Duration	负责人 Principal Investigator
雷电监测信息特征分析系统的开发和应用 Development and application of lightning detection and analysis systems	中国气象局：关键技术集成应用项目 CMA: project of key technology integration and application	2015—2016	姚雯 Yao Wen
玉米干旱致灾临界气象条件及其监测预警技术 Research on critical meteorological conditions for maize drought and development of drought monitoring and warning technology	中国气象局：行业专项 CMA: special fund for meteorological service	2015—2017	周莉 Zhou Li
中国地区气溶胶光学特性数据集的研发和集成 Research and development of datasets for China aerosol optical properties	中国气象局：气候变化专项 CMA: special fund for climate change	2015—2016	车慧正 Che Huizheng

MOST: Ministry of Science and Technology (科技部)

NSFC: National Natural Science Foundation of China (国家自然科学基金)

SHRM: State Human Resource Ministry (国家人事部)

CMA: China Meteorological Administration (中国气象局)



2015年，气科院共招收44名硕士研究生、18名博士研究生，进站博士后10人；毕业46名硕士、14名博士。目前在校硕士研究生133人，博士研究生60人，在站博士后13人。

国家人力资源和社会保障部和全国博士后管理委员会每5年组织一次全国博士后科研工作站综合评估，在2015年的评估中气科院博士后科研工作站被评为优秀站（144/2079，<7%），是大气科学领域唯一受到通报表扬的单位。

In the year of 2015, CAMS enrolled 44 MSc graduates and 18 PhD students, and ten candidates joined the Post-Doctoral Working Station. 46 MSc and 14 PhD students graduated from CAMS this year. The current numbers of MSc, PhD and Post-Doctoral candidates at CAMS are 133, 60 and 13 respectively.

Every five years, Chinese Ministry of Human Resources and Social Security (MOHRSS) and National Post-Doctor Management Committee jointly organize nationwide comprehensive assessment of Post-Doctoral Working Stations. In 2015, CAMS Post-Doctoral Working Station was awarded station of excellence (only 144 among 2079 stations nationwide, <7%), which was the only one in the field of atmospheric science to win such award.

在中国气象局与中国科学院的合作协议框架下，2015年2月5日，中国科学院大学高鸿钧副校长、办公厅汪克强主任赴气科院调研。中国气象局宇如聪副局长、办公室余勇主任、科技司罗云峰司长出席调研活动，气科院端义宏院长、周广胜副院长及研究生部王欣主任参加了接待。双方就加强联合研究生培养等问题进行了研讨。

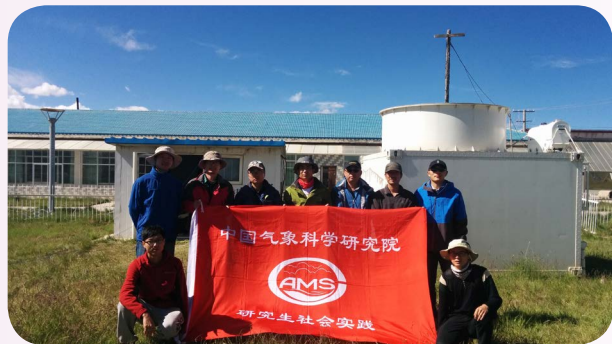


Under the framework of Cooperation Agreement between China Meteorological Administration (CMA) and Chinese Academy of Sciences (CAS), on 5 February 2015, the Vice President of University of CAS, Mr. Gao Hongjun and Director-General of its School Office, Mr. Wang Keqiang visited CAMS. They were received by CMA leaders including Deputy Administrator, Dr. Yu Rucong, Director-General of Headquarters Office, Mr. Yu Yong and Director-General of Department of S&T and Climate Change, Mr. Luo Yunfeng, etc, as well as CAMS leaders including President, Dr. Duan Yihong, Vice President, Mr. Zhou Guangsheng and Director of Graduates Office, Wang Xin. The two sides exchanged ideas about enhancing joint cultivation of graduate students.



2015年10月20日，气科院青联和团委联合举办了优秀青年赴国外访学交流报告会。王怀刚副院长参加报告会并讲话，青联副主席王亚强主持报告会。报告会上，人工影响天气中心副研究员段婧和气候系统研究所副研究员刘舸分别向青年科研人员和研究生做了访学成果汇报和交流。

On 20 October 2015, the Youth League and CPC Youth Committee of CAMS jointly held the Workshop for Foreign Visits Outcome Exchange by Excellent Youths. CAMS Vice President, Mr. Wang Huaigang attended and addressed the workshop, which was presided over by Deputy Head of Youth League of CAMS, Mr. Wang Yaqiang. Two associate researchers, Ms. Duan Jing from Weather Modification Centre and Mr. Liu Ge from Institute of Climate System reported respectively their overseas visiting outcomes to the young research staff and graduate students of CAMS and exchanged ideas with them.



为鼓励研究生积极参与重大课题的科研工作，为研究生提供实际锻炼平台，2015年7—8月研究生部选派9名硕士研究生参与了第3次青藏高原大气科学试验的那曲地区外场观测试验。

In order to encourage graduates to participate actively in significant research projects and provide graduates with practice platforms, in July and August 2015, CAMS Graduates Office selected and designated 9 MSc

graduates to participate in the field observation experiment in Naqu of Tibet, which was part of the Third Tibetan Plateau Scientific Experiment on Atmosphere.



2015年的“全国大气科学领域暑期学校”吸引了来自各高校的优秀学员的积极参与，扩大了气科院研究生教育在全国高校的知名度。

The National Training Workshop (Summer School) in Atmospheric Sciences in 2015 attracted excellent students from numerous universities and colleges nationwide, which raised the visibility of CAMS graduate training among the universities in China.



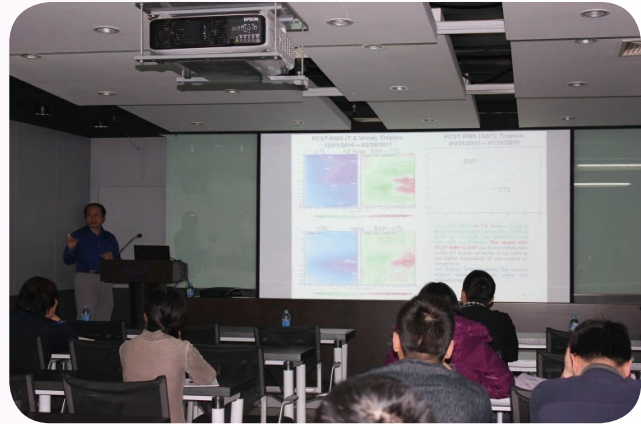
气科院在研究生教育中不仅重视学生专业知识及技能的学习, 同时注重学生们德智体全面发展, 注意培养学生关注社会关爱社会的意识, 在业余时间组织研究生为“太阳村”的孩子捐助衣服、书籍和床, 到养老院慰问孤寡老人, 举办研究生运动会等活动。

In its graduate education, CAMS attaches great importance not only to the study of expertise knowledge and techniques, but also to the all-round development of students in moral standards and physical health. The consciousness of caring the whole society has been well cultivated, e.g. the graduates were organized during their spare time to donate clothes, books and beds to children in “Sun Village”, to visit elderly people of no family in the senior citizen’s home, as well as to hold the sports meeting for graduates, etc.

合作与交流 Cooperation and Communication

2015年1月7日，NCEP/NOAA环境模式中心的李旭博士应邀访问气科院，并做了题为“数值天气预报中海洋因子的改进”的学术报告。李旭博士介绍了目前海温分析的现状和在海温分析中观测资料的使用等方面存在的问题，并提出了改进的科学基础和方案。张人禾研究员主持了报告会。

On 7 January 2015, Dr. Li Xu from NCEP/NOAA was invited to visit CAMS and presented his academic report themed “Improving the Ocean in Numerical Weather Prediction”. Dr. Li introduced the current status of sea temperature analysis and existing problems of using observation data in sea temperature analysis. He also proposed the improvement scheme of sea temperature analysis and pointed out its scientific basis. The presentation was chaired by CAMS Researcher, Dr. Zhang Renhe.



2015年1月22日，美国马里兰大学Russell R. Dickerson教授应邀访问大气成分研究所，并做了题为“美国东部臭氧与气溶胶：政策相关的科学进展”的学术报告。Dickerson教授主要介绍了其研究团队近年在美国东部开展的飞机观测试验，以及与卫星数据和模式结果比对的研究成果。

On 22 January 2015, Prof. Russell R. Dickerson from US University of Maryland was invited to visit CAMS Institute of Atmospheric Composition and presented his academic report titled “Ozone and Aerosols over the Eastern US: Progress through Policy Relevant Science”. Prof. Dickerson introduced the aircraft observation experiment carried out in eastern US by his research team, as well as the comparison results between aircraft observation and satellite data with model outputs.



2015年1月26日，美国纽约州立大学大气科学研究中心主任Everette Joseph博士和闵启龙教授应邀访问大气探测研究所，并分别做了题为“纽约州立大学大气科学研究中心：研究现状及合作机会”和“综合利用可见光、红外和微波传感器观测亚马孙森林的季节性变化”的学术报告。Joseph是气溶胶、云物理和气候模式方面的著名专家，闵启龙教授在遥感、大气探测和仪器研发等方面都有很多突出的工作。交流会由副所长吕伟涛研究员主持。

On 26 January 2015, Dr. Everette Joseph, Director of Atmospheric Science Research Center, State University of New York, together with Prof. Min Qilong, visited CAMS Institute of Atmospheric Sounding. They presented their respective reports entitled “Atmospheric Sciences Research Center: Research and Opportunities for Collaboration” and “Synthesizing the Visible, Infrared and Microwave for Observing Amazon Forest Seasonality”. Dr. Joseph is a renowned expert in aerosol, cloud physics and climate model while Prof. Min is well recognized by his remarkable contribution in remote sensing, atmospheric sounding and equipment development. Dr. Lü Weitao, CAMS Researcher and Deputy Director of the Institute of Atmospheric Sounding, presided over the presentation.



2015年1月26日，英国气象局的Brian Golding教授应邀访问灾害天气国家重点实验室，并做了题为“高影响天气的预报：英国洪水灾害与高影响天气”的学术报告。Golding教授主要介绍了洪水灾害对英国地区的影响以及英国气象局最近开发的2.2 km（分辨率）集合预报系统及其业务应用等情况。

On 26 January 2015, Prof. Brian Golding from UK Met-Office visited CAMS State Key Laboratory on Severe Weather (LaSW) and presented the academic report themed “Forecasting High Impact Weather: UK Surface

Water Floods and HI Weather”. Prof. Golding introduced the impact of floods on UK, as well as the ensemble prediction system with a resolution of 2.2 km recently developed by Met-Office and its application in operation.



2015年4月14—17日，英国詹姆斯赫顿研究所作物模型专家Davide Cammarano研究员访问了生态环境与农业气象研究所，并做了题为“气候变化与作物产量：从区域到全球的粮食安全研究进展”的学术报告，同时介绍了农业技术推广决策支持系统作物模式理论和方法。报告会由房世波研究员主持，相关科研人员和研究生参加了报告会。

On 14–17 April 2015, Dr. Davide Cammarano, crops modeling expert from UK James Hutton Institute (JHI) visited CAMS Institute of Ecological Environment and

Agrometeorology, presented the academic report titled “Climate Change and Crops Yields: Research Development in Food Security from Local to Global”, in which he also introduced the theories and methods of Decision Support System for Agrotechnology Transfer (DSSAT). The presentation was chaired by Dr. Fang Shibo, CAMS researcher, and was attended by CAMS research staff and graduate students.

2015年6月30日，应灾害天气国家重点实验室邀请，美国宾夕法尼亚州立大学张福青教授前来访问交流，并做了题为“集合数据同化的进展与挑战”的学术报告。灾害天气国家重点实验室副主任徐晶主持了报告会。

On 30 June 2015, invited by CAMS State Key Laboratory on Severe Weather (LaSW), Prof. Zhang Fuqing from US State University of Pennsylvania visited CAMS and gave the report entitled “Advances and Challenges in Ensemble-Based Data Assimilation”. The presentation was chaired by Deputy Director of LaSW, Ms. Xu Jing.





2015年7月6日，WMO的大气环境研究部Oksana Tarasova博士和Alexander Baklanov博士、GAW城市气象环境研究科学指导组主席Greg Carmichael教授一行来气科院进行工作交流。院长端义宏出席工作会议并致辞。气科院承担的WMO先导性项目“空气质量预报中近实时数据应用”负责人张小曳研究员汇报了项目情况，WMO专家充分肯定了项目取得的进展和成果。

On 6 July 2015, Dr. Oksana Tarasova and Dr. Alexander Baklanov from WMO Atmospheric

Environment Research Unit, together with Prof. Greg Carmichael, chairman of the scientific steering group of Urban Meteorological Environment Research, WMO GAW program, visited CAMS. President of CAMS, Dr. Duan Yihong chaired and addressed the discussion. The WMO GURME Pilot Project “Near Real Time Data Application in Air Quality Forecast” undertaken by CAMS was introduced to the visiting guests by Researcher Zhang Xiaoye, who was in charge of the program. The progress and outcomes achieved by CAMS was well recognized by the visiting WMO experts.



2015年7月6日，德国气象局（DWD）局长Gerhard Adrian教授一行3人参观了气科院大气化学重点实验室，周广胜副院长出席接待。大气成分研究所所长孙俊英向来宾介绍了气科院大气成分的基础观测、预报模式的发展及应用等情况。

On 6 July 2015, Prof. Gerhard Adrian, President of DWD, together with two of his colleagues, visited CAMS Key Laboratory on Atmospheric Chemistry, and CAMS Vice President, Mr. Zhou Guangsheng received the guests. Director of CAMS Institute of Atmospheric Composition, Dr. Sun Junying introduced the basic observation of atmospheric composition, development and application of its forecasting models, etc.

2015年7月7日，美国马里兰大学大气和海洋科学系、美国国家海洋和大气管理局空气资源实验室的资深研究员任信荣博士应邀访问大气成分研究所，并做了题为“美国巴尔的摩-华盛顿地区的温室气体排放：2015年冬季飞机观测结果”的学术报告。任信荣博士目前为马里兰大学飞机观测计划的负责人。

On 7 July 2015, Dr. Ren Rongxin, senior researcher from Department of Atmospheric and Oceanic Science, US University of Maryland, as well as Air Resource Laboratory of NOAA (US National Oceanic and Atmospheric Administration), visited CAMS Institute of Atmospheric Composition and presented the academic report titled “Greenhouse Gas Emissions from the Baltimore-Washington Area: Results from the Winter 2015 Aircraft Observations”. Dr. Ren Rongxin was the person in charge of the aircraft observation plan at University of Maryland.



2015年7月14日，蒙古国家气象与环境监测局新任局长Donio Tsogt-Ochir先生和外事官Erdenebat Eldev-Ochir先生一行2人访问中国气象局人工影响天气中心。人工影响天气中心副主任郭学良向来宾介绍了人工影响技术研究、仪器装备、运行体制等方面的基本情况。

On 14 July 2015, the new Director-General of Hydrology and Environment Monitoring of Mongolia (NAMEM), Mr. Donio Tsogt-Ochir, together with Mr. Erdenebat Eldev-Ochir, international cooperation official of

NAMEM, visited CMA Weather Modification Centre. The Deputy Director-General of the centre introduced the technology research, equipment and operational system of weather modification.



2015年7月16日，国际大气边界层研究知名专家、美国圣何塞州立大学Robert Bornstein教授应邀到灾害天气国家重点实验室进行学术交流，并做了题为“气候变迁下城市边界层的观测与模拟”的学术报告。报告会由气科院“千人计划”专家陈飞教授主持。

On 16 July 2015, Prof. Robert Bornstein from US San Jose State University, who is an internationally renowned expert in atmospheric boundary research, visited CAMS LaSW to present his academic report themed “Observation and Simulation of Urban PBLs in

a Changing Climate”. The presentation was presided over by Prof. Chen Fei from CAMS, who is a member of the Chinese Government sponsored Recruitment Program of Global Experts.

2015年8月10日，美国强风暴实验室（NSSL）张芃菲博士应邀访问灾害天气国家重点实验室，并做了题为“美国双线偏振雷达研究新进展”的学术报告。张芃菲博士主要从事双线偏振雷达和多普勒雷达数据质量控制、降水估测方法等方面的研究。刘黎平研究员主持了报告会。

On 10 August 2015, Dr. Zhang Pengfei from US National Severe Storm Laboratory (NSSL) visited CAMS LaSW and made the report titled “Some Progresses in the Applications of Dual Polarimetric Radar in US” and

CAMS Researcher, Liu Liping, chaired the presentation. Dr. Zhang Pengfei has been specialized in the research of dual polarization radar and Doppler radar data quality control, precipitation estimation methods, etc.





2015年8月27日，在泰国驻华使馆工作人员的陪同下，泰国农业部皇家造雨和农业航空司代表团一行40人参观访问中国气象局人工影响天气中心。中心副主任郭学良和相关专家为来宾介绍了中国人工影响天气的概况以及国家级人工影响天气业务平台的运行情况。泰方希望未来与中方在人工增雨领域开展深入的技术交流与合作。

On 27 August 2015, a 40-member delegation from the Royal Rain Making Department of Ministry of Agriculture and Cooperatives of Thailand visited CMA Weather Modification Centre, accompanied by the official from Thailand Embassy to China. Deputy Director-General of the centre, Mr. Guo Xueliang and CAMS experts introduced weather modification in China as well as the national weather modification platform. The Thailand guests expressed their hope of establishing close collaboration with CMA in weather modification techniques.



2015年9月16日，香港理工大学教授、国际全球大气化学计划（IGAC）科学指导委员会委员王韬博士应邀访问大气成分研究所并做了题为“氮氧化物的非均相过程及对臭氧的影响”的学术报告。徐晓斌研究员主持了报告会。

On 16 September 2015, Dr. Wang Tao from Hong Kong Polytechnic University, visited CAMS Institute of Atmospheric Composition and gave the report “Heterogeneous Processes of Nitrogen Oxides and Impact on Ozone”. Dr. Wang is a member of the Scientific Steering Committee of International Global

Atmospheric Chemistry Program (IGAC). The presentation was chaired by CAMS Researcher, Dr. Xu Xiaobin.

2015年10月26日，英国洛桑实验室高级研究员吴连海博士在生态环境与农业气象研究所做了题为“量化研究草地生态系统的未来变化”的学术报告，详细介绍了由他主持开发的土壤-植物-大气连续系统模型（SPACSYS）。该模型已在英国、欧洲、加拿大和中国的一些大型研究项目中应用。谭凯炎副研究员主持了报告会。

On 26 October 2015, Dr. Wu Lianhai from UK Rothamsted Experimental Station made the academic presentation “Quantify Future Dynamics of Grassland Ecosystem” at CAMS Institute of Ecological Environment and Agrometeorology, in which he introduced in detail the model of Soil-Plant-Atmosphere Continuum System (SPACSYS) that he developed. Such model has been applied by several significant research programs in UK, Europe, Canada and China. The presentation was chaired by CAMS Associate Researcher, Mr. Tan Kaiyan.



2015年12月7日，挪威奥斯陆大学化学系Claus Nielsen和Armin Wisthaler教授应邀访问大气成分研究所，分别做了题为“与基于胺的碳捕获技术相关的环境问题”和“基于化学转移反应的飞行时间质谱技术的气体 and 颗粒物在线实时化学分析”的报告。孙俊英研究员主持了报告会。

On 7 December 2015, Profs. Claus Nielsen and Armin Wisthaler from the Department of Chemistry, University of Oslo, Norway, were invited to visit CAMS Institute of Atmospheric Composition. They gave respective reports with the titles “Environmental Issues Related to Amine-Based Carbon Capture Technology” and “On-Line Chemical Analysis of Gas and Particulate Phase Organics in the Atmosphere by PTR-ToF-MS”. The presentation was presided over by CAMS Researcher, Dr. Sun Junying.

2015 年出版物
 Publications in 2015

作者 Author (rank)	题名 Title	出版物名/出版社 Publication name or Publisher	年, 卷(期) Year, Volume (Issue)	备注 Notes
An Xingqin	Tracking influential haze source areas in North China using an adjoint model, GRAPES-CUACE	Geoscientific Model Development Discussions	2015, 8	
An Xingqin	Association between PM ₁₀ and respiratory hospital admissions in different seasons in Lanzhou	Journal of Environmental Health	2015, 77(6)	
An Xingqin (2nd)	Application of a model to study emission reduction schemes for critical emission sources	Atmospheric Environment	2015, 9(1)	SCI
Che Huizheng	Fine mode aerosol optical properties related to cloud and fog processing over a cluster of cities in Northeast China	Aerosol and Air Quality Research	2015, 15(5)	SCI
Che Huizheng (2nd)	Investigation of Aerosol Optical Depth (AOD) and angström exponent over the desert region of Northwestern China based on measurements from the China aerosol Remote Sensing Network (CARSNET)	Aerosol and Air Quality Research	2015, 15(5)	SCI
Che Huizheng (2nd)	Temporal variability of the visibility, particulate matter mass concentration and aerosol optical properties over an urban site in Northeast China	Atmospheric Research	2015, 166(2)	SCI
Che Huizheng (3rd)	Study of aerosol optical properties at Kunming in Southwest China and long-range transport of biomass burning aerosols from North Burma	Atmospheric Research	2015, 169(9)	SCI
Che Huizheng (3rd)	Column-integrated aerosol optical properties and direct radiative forcing based on sun photometer measurements at a semi-arid rural site in Northeast China	Atmospheric Research	2015, 157(4)	SCI
Che Huizheng, et al.	Fine mode aerosol optical properties related to cloud and fog processing over a cluster of cities in Northeast China	Aerosol and Air Quality Research	2015, 15(5)	SCI
Che Huizheng, et al.	Ground-based aerosol climatology of China: Aerosol optical depths from the China Aerosol Remote Sensing Network (CARSNET) 2002–2013	Atmospheric Chemistry and Physics	2015, 15(1)	SCI
Che Huizheng, et al.	Application of aerosol optical properties to estimate aerosol type from ground-based remote sensing observation at urban area of northeastern China	Journal of Atmospheric and Solar-Terrestrial Physics	2015, 132(1)	SCI
Che Huizheng, et al.	Analyses of aerosol optical properties and direct radiative forcing over urban and industrial regions in Northeast China	Meteorology and Atmospheric Physics	2015, 127(3)	SCI

作者 Author (rank)	题名 Title	出版物名/出版社 Publication name or Publisher	年, 卷(期) Year, Volume (Issue)	备注 Notes
Chen Bin	Spatio-temporal structure of the moisture sources feeding heavy precipitation events over the Sichuan Basin	International Journal of Climatology	doi:10.1002/joc.4567	SCI
Chen Bin (3rd)	The derivation of moist baroclinic Ertel-Rossby invariant in fast manifold and its application to typhoons	Science China: Earth Sciences	2015, 58(6)	SCI
Ding Minghu	Surface mass balance and its climate significance from the coast to Dome A, East Antarctica	Science China: Earth Sciences	2015, 58(10)	SCI
Fang Shibo	Spectra and vegetation index variations in moss soil crust in different seasons, and in wet and dry conditions	International Journal of Applied Earth Observation and Geoinformation	2015, 38(1)	SCI
Fang Shibo, et al.	Effects of increased day and night temperature with supplemental infrared heating on winter wheat growth in North China	European Journal of Agronomy	2015, 64(1)	SCI
Fang Shuangxi, et al.	The determination of regional CO ₂ mole fractions at the Longfengshan WMO/GAW station: A comparison of four data filtering approaches	Atmospheric Environment	2015, 116(1)	SCI
Gan Yanjun	Stepwise sensitivity analysis from qualitative to quantitative: Application to the terrestrial hydrological modeling of a Conjunctive Surface-Subsurface Process (CSSP) land surface model	Journal of Advances in Modeling Earth Systems	2015, 7(2)	
Guo Jianping (2nd)	Multi-sensor quantification of aerosol-induced variability in warm	Atmospheric Environment	2015, 113	SCI
Guo Jianping (2nd)	CALIPSO inferred most probable heights of global dust and smoke layers	Journal of Geophysical Research	2015, 120(10)	SCI
Guo Jianping, et al.	Effects of adjusting cropping systems on utilization efficiency of climate	Physics and Chemistry of the Earth	2015, 1	SCI
Guo Xueliang	Advances in cloud physics and weather modification in China	Advances in Atmospheric Sciences	2015, 32(2)	SCI
Guo Xueliang (2nd)	Ice crystal habits and growth processes in stratiform clouds with embedded convection examined through aircraft observations in northern China	Journal of the Atmospheric Sciences	2015, 72(2)	SCI
Hu Liang	Seasonal and interannual variation of diurnal precipitation over the Tibetan Plateau	Atmospheric and Oceanic Science Letters	2015, 8(6)	
Hu Liang (3rd)	The impact of Guizhou topography on the distribution of freezing rain in early January 2011	Quarterly Journal of the Royal Meteorological Society	2015, 141(693)	

作者 Author (rank)	题名 Title	出版物名/出版社 Publication name or Publisher	年, 卷(期) Year, Volume (Issue)	备注 Notes
Hu Zhiqun, et al.	A comparison of de-noising methods for differential phase shift and associated rainfall estimation	Journal of Meteorological Research	2015, 29(2)	SCIE
Huo Zhiguo (2nd)	Rice flooding disaster diagnosis analysis and growth monitoring based on HJ-CCD data	Transactions of the Chinese Society of Agricultural Engineering	2015, 31(Z2)	EI
Jiang Zhina, et al.	Exploring phase strength asymmetry of the North Atlantic oscillation by using conditional nonlinear optimal perturbation	Advances in Atmospheric Sciences	2015, 32(5)	SCI
Li Jian (2nd)	Two major circulation structures leading to heavy summer rainfall over central North China	Journal of Geophysical Research	2015, 120(10)	SCI
Li Jian (2nd)	Recent reversal of the upper-tropospheric temperature trend and its role in intensifying the East Asian summer monsoon	Scientific Reports	2015, 5	SCI
Li Jian (3rd)	Correlation between peak intensity of extreme afternoon short-duration rainfall and humidity and surface air temperature in southeast coast of China	Journal of Tropical Meteorology	2015, 21(3)	SCIE
Li Jian, et al.	Precipitation over East Asia simulated by NCAR CAM5 at different horizontal resolutions	Journal of Advances in Modeling Earth Systems	2015, 7(2)	SCI
Li Lun (2nd)	Seasonal spatial heterogeneity of warming rates on the Tibetan Plateau over the past 30 years	Scientific Reports	2015, 5	SCI
Li Yi, et al.	Ambient temperature enhanced acute cardiovascular-respiratory mortality effects of PM _{2.5} in Beijing, China	International Journal of Biometeorology	2015, 59(12)	
Li Ying (3rd)	Interaction between Typhoon Vicente (1208) and the Western Pacific subtropical high during the Beijing extreme rainfall of 21 July 2012	Journal of Meteorological Research	2015, 29(2)	SCIE
Liang Zhaoming, et al.	Numerical study of the evolution of a sea-breeze front under two environmental flows	Journal of Meteorological Research	2015, 29(3)	SCIE
Liu Chang, et al.	Effect of aluminium dust on secondary organic aerosol formation in m-xylene/NO _x photo-oxidation	Science China: Earth Sciences	2015, 58(2)	SCI
Liu Ge, et al.	Synergic contribution of precipitation anomalies over Northwestern India and the South China sea to high temperature over the Yangtze River Valley	Advances in Atmospheric Sciences	2015, 32(1)	SCI
Liu Ge, et al.	Spatial and temporal characteristics of summer precipitation events spanning different numbers of days over Asia	International Journal of Climatology	doi: 10.1002/joc.4495	SCI

作者 Author (rank)	题名 Title	出版物名/出版社 Publication name or Publisher	年, 卷(期) Year, Volume (Issue)	备注 Notes
Liu Ge, et al.	Preceding factors of summer Asian-Pacific oscillation and the physical mechanism for their potential influences	Journal of Climate	2015, 28(1)	SCI
Liu Jiandong	Changes in the relationship between solar radiation and sunshine duration in large cities of China	Energy	2015, 82(1)	SCI
Liu Liping, et al.	Comprehensive radar observations of clouds and precipitation over the Tibetan Plateau and preliminary analysis of cloud properties	Journal of Meteorological Research	2015, 29(4)	SCI
Liu Yu	A method for solving relative dispersion of the cloud droplet	Science China: Earth Sciences	2015, 58(6)	SCI
Liu Yu (2nd)	Changes in stratospheric ClO and HCl concentrations under different greenhouse gas emission scenarios	Journal of Meteorological Research	2015, 29(4)	SCIE
Luo Yali, et al.	Investigation of the predictability and physical mechanisms of an extreme-rainfall-producing mesoscale convective system along the Meiyu front in East China: An ensemble approach	Journal of Geophysical Research	2015, 120(20)	SCI
Lü Weitao (2nd)	Optical progression characteristics of an interesting natural downward bipolar lightning flash	Journal of Geophysical Research	2015, 120(1)	SCI
Lü Weitao (2nd)	A hybrid method based on extreme learning machine and k-nearest neighbor for cloud classification of ground-based visible cloud image	Neurocomputing	2015, 160	SCI
Lü Weitao, et al.	Three-dimensional propagation characteristics of the leaders in the attachment process of a downward negative lightning flash	Journal of Atmospheric and Solar-Terrestrial Physics	2015, 136	SCI
Peng Xindong (2nd)	An improved dynamic core for a non-hydrostatic model system on the Yin-Yang grid	Advances in Atmospheric Sciences	2015, 32(5)	SCIE
Qian Tingting, et al.	Rainy-season precipitation over the Sichuan Basin and adjacent regions in southwestern China	Monthly Weather Review	2015, 143(1)	
Ren Fumin	Changes in regional heavy rainfall events in China during 1961–2012	Advances in Atmospheric Sciences	2015, 32(5)	SCI
Shen Xiaojing, et al.	Characterization of submicron aerosols and effect on visibility during a severe haze-fog episode in Yangtze River Delta, China	Atmospheric Environment	2015, 120	SCI
Su Jingzhi (2nd)	What hindered the El Niño pattern in 2014?	Geophysical Research Letters	2015, 42(16)	SCI
Sun Junying (2nd)	Chemical composition of PM _{2.5} based on two-year measurements at an urban site in Beijing	Aerosol and Air Quality Research	2015, 15(1)	SCI

作者 Author (rank)	题名 Title	出版物名/出版社 Publication name or Publisher	年, 卷(期) Year, Volume (Issue)	备注 Notes
Sun Junying (2nd)	Observations of relative humidity effects on aerosol light scattering in the Yangtze River Delta of China	Atmospheric Chemistry and Physics	2015, 15(14)	SCI
Tan Kaiyan, et al.	Responses of irrigated winter wheat yield in North China to increased temperature and elevated CO ₂ concentration	Journal of Meteorological Research	2015, 29(4)	SCIE
Wang Donghai, et al.	In-situ measurements of cloud-precipitation microphysics in the East Asian monsoon region since 1960	Journal of Meteorological Research	2015, 29(2)	SCIE
Wang Fei, et al.	Impact of the vertical velocity field on charging processes and charge separation in a simulated thunderstorm	Journal of Meteorological Research	2015, 29(2)	SCIE
Wang Gaili, et al.	Improvement of forecast skill for severe weather by merging radar-based extrapolation and storm-scale NWP corrected forecast	Atmospheric Research	2015, 154(2)	SCI
Wang Gaili, et al.	Inter-comparison of radar-based nowcasting schemes in Jianghuai River Basin, China	Meteorological Applications	2015, 22(3)	SCI
Wang Hong (2nd)	Modeling study of PM _{2.5} pollutant transport across cities in China	Atmospheric Chemistry and Physics	2015, 15(15)	SCI
Wang Hong, et al.	Mesoscale modelling study of the interactions between aerosols and PBL meteorology during a haze episode in China Jing-Jin-Ji and its near surrounding region—Part 2: Aerosols radiative feedback effects	Atmospheric Chemistry and Physics	2015, 15(15)	SCI
Wang Hong, et al.	Mesoscale modeling study of the interactions between aerosols and PBL meteorology during a haze episode in Jing-Jin-Ji (China) and its nearby surrounding region—Part 1: Aerosols distributions and meteorological features	Atmospheric Chemistry and Physics	2015, 15(15)	SCI
Wang Hui, et al.	Synoptic pattern and weather phenomena in association with extreme wide convection over Southeast China during summer monsoon period	Journal of Meteorological Research	2015, 29(1)	SCIE
Wang Ping (3rd)	Warm-dry collocation of recent drought in southwestern China tied to moisture transport and climate warming	Chinese Physics B	2015, 24(4)	SCI
Wang Yaqiang (2nd)	Widespread albedo decreasing and induced melting of Himalayan snow and ice in the early 21st century	PloS One	2015, 10(6)	SCI
Wang Yaqiang (3rd)	Detection and attribution of regional CO ₂ concentration anomalies using surface observations	Atmospheric Environment	2015, 123(1)	SCI

作者 Author (rank)	题名 Title	出版物名/出版社 Publication name or Publisher	年, 卷(期) Year, Volume (Issue)	备注 Notes
Wang Yaqiang, et al.	Spatial and temporal variations of the concentrations of PM ₁₀ , PM _{2.5} and PM ₁ in China	Atmospheric Chemistry and Physics	2015, 15(4)	SCI
Wang Zhili (2nd)	Impact of four-stream radiative transfer algorithm on aerosol direct radiative effect and forcing	International Journal of Climatology	2015, 35(14)	SCI
Wang Zhili (3rd)	The influence of different black carbon and sulfate mixing methods on their optical and radiative properties	Journal of Quantitative Spectroscopy & Radiative Transfer	2015, 161	SCI
Wang Zhili, et al.	Simultaneous reductions in emissions of black carbon and co-emitted species will weaken the aerosol net cooling effect	Atmospheric Chemistry and Physics	2015, 15(7)	SCI
Wei Ting (3rd)	Simulated spatio-temporal characteristics of climate change in China during the Han Dynasty (1–200 A.D.)	Atmospheric and Oceanic Science Letters	2015, 8(6)	
Wu Bingyi (2nd)	Enhancement of winter Arctic warming by the Siberian high over the past decade	Atmospheric and Oceanic Science Letters	2015, 8(5)	
Wu Bingyi, et al.	Patterns of Asian winter climate variability and links to sea ice	Journal of Climate	2015, 28(9)	SCI
Wu Lingyan (2nd)	Heterogeneous chemistry of trace atmospheric gases on atmospheric aerosols: An overview	Science Foundation in China	2015, 23(3)	
Xiao Dong, et al.	Plausible influence of Atlantic Ocean SST anomalies on winter haze in China	Theoretical and Applied Climatology	2015, 122(1)	SCI
Xu Hongxiong	A numerical study on impact of Taiwan Island surface heat flux on super Typhoon Haitang (2005)	Advances in Meteorology	2015, 22	
Xu Hongxiong	The impact of Typhoon Danas (2013) on the torrential rainfall associated with Typhoon Fitow (2013) in East China	Advances in Meteorology	2015, 1–12	
Xu Hongxiong, et al.	A numerical study of the Beijing extreme rainfall of 21 July 2012 and the impact of topography	Advances in Meteorology	2015, 1–12	
Xu Jing	A statistical analysis on the dependence of tropical cyclone intensification rate on the storm intensity and size in the North Atlantic	Weather and Forecasting	2015, 30(3)	SCI
Xu Jing (3rd)	Numerical simulation and analysis of the Yangtze River Delta rainstorm on 8 October 2013 caused by binary typhoons	Atmospheric Research	2015, 166(12)	SCI
Xu Xiaobin (2nd)	Two-year measurements of surface ozone at Dangxiong, a remote highland site in the Tibetan Plateau	Journal of Environmental Sciences	2015, 31(1)	SCI

作者 Author (rank)	题名 Title	出版物名/出版社 Publication name or Publisher	年, 卷(期) Year, Volume (Issue)	备注 Notes
Xue Haile	An online model correction method based on an inverse problem: Part II—Systematic model error correction	Advances in Atmospheric Sciences	2015, 32(11)	SCI
Xue Haile	An online model correction method based on an inverse problem: Part I—Model error estimation by iteration	Advances in Atmospheric Sciences	2015, 32(10)	SCI
Yang Jianying, et al.	Water consumption in winter wheat and summer maize cropping system based on SEBAL model in Huang-Huai-Hai Plain, China	Journal of Integrative Agriculture	2015, 14(10)	SCIE
Yang Jun, et al.	An automated cloud detection method based on the green channel of total-sky visible images	Atmospheric Measurement Techniques	2015, 8	SCI
Yang Jun, et al.	A passive and active microwave-vector radiative transfer (PAM-VRT) model	Journal of Quantitative Spectroscopy & Radiative Transfer	2015, 165	SCI
Yin Jinfang	An investigation into the three-dimensional cloud structure over East Asia from the CALIPSO-GOCCP data	Science China: Earth Sciences	2015, 58(12)	SCI
Yu Rucong (2nd)	Three-dimensional circulation structure of summer heavy rainfall in central North China	Weather and Forecasting	2015, 30(1)	SCI
Yu Rucong, et al.	Improvement of rainfall simulation on the steep edge of the Tibetan Plateau by using a finite-difference transport scheme in CAM5	Climate Dynamics	2015, 45(9)	SCI
Yu Rucong, et al.	The definition and characteristics of regional rainfall events demonstrated by warm season precipitation over the Beijing Plain	Journal of Hydrometeorology	2015, 16(1)	SCI
Yuan Naiming (3rd)	Impact of previous one-step variation in positively long-range correlated processes	Theoretical and Applied Climatology	2015, 124	SCI
Yuan Naiming, et al.	On the long-term climate memory in the surface air temperature records over Antarctica: A nonnegligible factor for trend evaluation	Journal of Climate	2015, 28(1)	SCI
Yuan Naiming, et al.	Detrended partial-cross-correlation analysis: A new method for analyzing correlations in complex system	Scientific Reports	2015, 5	SCI
Zhang Gen, et al.	Summertime distributions of peroxyacetyl nitrate (PAN) and peroxypropionyl nitrate (PPN) in Beijing	Atmospheric Environment	2015, 103(1)	SCI
Zhang Guo (2nd)	An observational and modeling study of impacts of bark beetle-caused tree mortality on surface energy and hydrological cycles	Journal of Hydrometeorology	2015, 16(2)	SCI
Zhang Renhe	Natural and human-induced changes in summer climate over the East Asian monsoon region in the last half century: A review	Advances in Climate Change Research	2015, 11(2)	

作者 Author (rank)	题名 Title	出版物名/出版社 Publication name or Publisher	年, 卷(期) Year, Volume (Issue)	备注 Notes
Zhang Renhe	Changes in East Asian summer monsoon and summer rainfall over eastern China during recent decades	Science Bulletin	2015, 60(13)	SCI
Zhang Renhe (2nd)	Interannual variation of the South Asian high and its relation with Indian and East Asian summer monsoon rainfall	Journal of Climate	2015, 28(7)	SCI
Zhang Renhe (2nd)	Improvement of ocean data assimilation system and climate prediction by assimilating Argo data	Journal of Tropical Meteorology	2015, 21(2)	SCIE
Zhang Renhe (2nd)	Impact of ENSO on the precipitation over China in winter half-years	Journal of Tropical Meteorology	2015, 21(2)	SCIE
Zhang Renhe, et al.	Role of intraseasonal oscillation in asymmetric impacts of El Niño and La Niña on the rainfall over southern China in boreal winter	Climate Dynamics	2015, 45(3)	SCI
Zhang Wenjuan, et al.	Relationship between lightning activity and tropical cyclone intensity over the Northwest Pacific	Journal of Geophysical Research	2015, 120(9)	SCI
Zhang Xiaoye (2nd)	Improving aerosol interaction with clouds and precipitation in a regional chemical weather modeling system	Atmospheric Chemistry and Physics	2015, 15(11)	SCI
Zhang Xiaoye (2nd)	Significant concentration changes of chemical components of PM ₁ in the Yangtze River Delta area of China and the implications for the formation mechanism of heavy haze-fog pollution	Science of the Total Environment	2015, 538	SCI
Zhang Xiaoye (3rd)	Influence of relative humidity on aerosol composition: Impacts on light extinction and visibility impairment at two sites in coastal area of China	Atmospheric Research	2015, 153	SCI
Zhang Yang, et al.	Preliminary breakdown, following lightning discharge processes and lower positive charge region	Atmospheric Research	2015, 161–162	SCI
Zhang Yi, et al.	Prediction of maize yield response to climate change with climate and crop model uncertainties	Journal of Applied Meteorology and Climatology	2015, 54(4)	SCI
Zhang Yi, et al.	Simulations of stratus clouds over eastern China in CAM5: Sources of errors	Journal of Climate	2015, 28(1)	SCI
Zhang Zhengqiu, et al.	Investigation of North American vegetation variability under recent climate: A study using the SSiB4/TRIFFID biophysical/dynamic vegetation model	Journal of Geophysical Research	2015, 120(4)	SCI
Zhao Junfang (3rd)	An improved mean shift segmentation method of high-resolution	Applied Mechanics and Materials	2015, 713–715	EI

作者 Author (rank)	题名 Title	出版物名/出版社 Publication name or Publisher	年, 卷(期) Year, Volume (Issue)	备注 Notes
Zhao Junfang (3rd)	The comparison of segmentation results for high-resolution remote	Applied Mechanics and Materials	2015, 713–715	EI
Zhao Junfang (3rd)	Soil moisture inversion based on AMSR-E and MODIS data fusion: A case study of Huaihe River Basin	Applied Mechanics and Materials	2015, 716–717	EI
Zhao Junfang (3rd)	Study on insect pests detection based on digital image	Applied Mechanics and Materials	2015, 701–702	EI
Zhao Junfang (3rd)	A novel model based on LBP and meanshift for UAV image segmentation	Applied Mechanics and Materials	2015, 701–702	EI
Zhao Junfang (3rd)	A comparative study of image segmentation based on the improved meanshift software with Edison	Applied Mechanics and Materials	2015, 701–702	EI
Zhao Junfang, et al.	Effects of climate change on cultivation patterns of spring maize and its climatic suitability in Northeast China	Agriculture, Ecosystems and Environment	2015, 202	SCI
Zhao Junfang, et al.	Exploring the relationships between climatic variables and climate-induced yield of spring maize in Northeast China	Agriculture, Ecosystems and Environment	2015, 207	SCI
Zhao Junfang, et al.	Exploring the dynamics of agricultural climatic resource utilization of spring maize over the past 50 years in Northeast China	Physics and Chemistry of the Earth	2015, 87	SCI
Zhao Junfang, et al.	Multidecadal changes in moisture condition during climatic growing period of crops in Northeast China	Physics and Chemistry of the Earth	2015, 87	SCI
Zheng Dong	Characteristics of flash initiations in a suprcell cluster with tornadoes	Atmospheric Research	2015, 167(1)	SCI
Zheng Xiangdong (3rd)	Variation characteristics of carbon monoxide and ozone over the course of the 2014 Chinese National Arctic Research Expedition	Advances in Polar Science	2015, 26(3)	SCI
Zheng Xiangdong, et al.	Mass and isotopic concentrations of water-insoluble refractory carbonin total suspended particulates at Mt. Waliguan Observatory (China)	Particuology	2015, 20(3)	SCI
Zheng Yongjun (3rd)	Improved tropical storm forecasts with GEOS-13/15 imager radiance assimilation and asymmetric vortex initialization in HWRF	Monthly Weather Review	2015, 143	
Zhong Lingzhi, et al.	An observational analysis of warm-sector rainfall characteristics associated with the 21 July 2012 Beijing extreme rainfall event	Journal of Geophysical Research	2015, 120(8)	SCI
Zhou Guangsheng (2nd)	Interactive effects of elevated CO ₂ and precipitation change on leaf nitrogen of dominant <i>Stipa L.</i> species	Ecology and Evolution	2015, 5(14)	

作者 Author (rank)	题名 Title	出版物名/出版社 Publication name or Publisher	年, 卷(期) Year, Volume (Issue)	备注 Notes
Zhou Guangsheng (2nd)	Climatic suitability of the potential geographic distribution of <i>Fagus longipetiolata</i> in China	Environmental Earth Sciences	2015, 73(3)	
Zhou Guangsheng (2nd)	The spatial and temporal dynamics of the carbon budget in the alpine grasslands on the Qinghai-Tibetan Plateau using the TEM model	Journal of Cleaner Production	2015, 107	
Zhou Guangsheng (2nd)	Remote estimation of the fraction of absorbed photosynthetically active radiation for a maize canopy in Northeast China	Journal of Plant Ecology	2015, 8(4)	SCI
Zhou Guangsheng (2nd)	Increase in flood and drought disasters during 1500–2000 in Southwest China	Natural Hazards	2015, 77	
Zhou Guangsheng (2nd)	Response and adaptation of photosynthesis, respiration, and antioxidant systems to elevated CO ₂ with environmental stress in plants	Plant Science	2015, 6	
Zhou Guangsheng (2nd)	Estimation of canopy water content by means of hyperspectral indices based on drought stress gradient experiments of maize in the North Plain China	Remote Sensing	2015, 7(11)	
Zhou Lingxi (2nd)	Atmospheric CO ₂ and its δ ¹³ C measurements from flask sampling at Lin'an regional background station in China	Atmospheric Environment	2015, 117	SCI
Zhou Xiuji (2nd)	Stochastic dynamic simulation of the 100-kyr cycles in climate system	Science China: Earth Sciences	2015, 58(3)	SCI
Zuo Zhiyan, et al.	Extreme cold and warm events over China in wintertime	International Journal of Climatology	2015, 35(35)	SCI
Zuo Zhiyan, et al.	Response of summer rainfall over China to spring snow anomalies over Siberia in the NCEP CFSv2 reforecast	Quarterly Journal of the Royal Meteorological Society	2015, 141(688)	SCI

作者 Author (rank)	题名 Title	出版物名/出版社 Publication name or Publisher	年,卷(期) Year, Volume (Issue)	备注 Notes
丁明虎	中国南极维多利亚新站气象特征分析	极地研究	2015, 27(4)	
丁明虎(第2)	大气水汽氢氧同位素观测研究进展——理论基础、观测方法和模拟	地理科学进展	2015, 34(3)	
丁明虎(第3)	北极夏季大气垂直结构与空间分布特征	海洋学报	2015, 37(11)	
马玉平(第2)	GECROS 模型在黄淮海地区模拟夏玉米生长的适应性评价	作物学报	2015, 41(1)	
马玉平等	预测未来 40 年气候变化对我国玉米产量的影响	应用生态学报	2015, 26(1)	
马玉平等	持续性温强和土壤水分对玉米发育进程的影响及其模拟	中国农学通报	2015, 31(3)	
马玉平等	黄淮海夏玉米不同发育阶段对旱涝灾害的敏感性	自然灾害学报	2015, 24(6)	
王东海(第2)	多普勒雷达资料同化在“7·21”北京特大暴雨两个例中的应用	气象学报	2015, 73(4)	
王东海(第2)	混合集合预报法在华南暴雨短期预报中的试验	应用气象学报	2015, 26(6)	
王东海(第3)	GFS 对我国南方持续性强降水可预报性评估	气象	2015, 41(1)	
王东海(第3)	2008 年春夏华南地区 MCS 时空分布和活动特征分析	热带气象学报	2015, 31(4)	
王东海(第3)	基于 DEM 的贵州山区气温和降水推算方法研究	西南大学学报: 自然科学版	2015, 37(1)	
王红艳等	利用雷达资料对自动雨量计实时质量控制的方法研究	大气科学	2015, 39(1)	
王培娟等	气候变暖对东北三省春玉米布局的可能影响及其应对策略	自然资源学报	2015, 30(8)	
车慧正(第3)	塔克拉玛干沙漠西南缘大气气溶胶光学特性	干旱区研究	2015, 32(5)	
方双喜(第2)	气相色谱-脉冲氦离子化检测法(GC-PDHID)分析大气中分子氢(H ₂)浓度	环境科学	2015, 36(1)	
方双喜(第2)	龙凤山站大气 CO ₂ 浓度 2 种筛分方法对比研究	中国环境科学	2015, 35(2)	EI
尹金方	冰核对云物理属性和降水影响的研究	地球科学进展	2015, 30(3)	
吕伟涛(第2)	双站摄像资料重建闪电三维通道的方法	高原气象	2015, 34(3)	
吕伟涛(第2)	不同高度建筑物上的下行地闪回击特征	应用气象学报	2015, 26(3)	
吕伟涛(第2)	2011—2012 年广州高建筑物雷电磁场特征统计	应用气象学报	2015, 26(1)	
邬定荣(第3)	华北平原夏玉米主要发育期对气候变化的响应	中国农业气象	2015, 36(4)	

作者 Author (rank)	题名 Title	出版物名/出版社 Publication name or Publisher	年,卷(期) Year, Volume (Issue)	备注 Notes
邬定荣等	基于作物生长模型及 CAST 的华北夏玉米生产力区划研究	气象科学	2015, 35(1)	
刘伯奇	2014 年赤道东太平洋 El Niño 事件发展以及停滞过程的成因	科学通报	2015, 60(22)	
刘伯奇(第3)	春季青藏高原表面感热加热的年际变化特征及其对印度夏季风爆发时间的影响	大气科学	2015, 39(6)	
刘伯奇(第3)	6 种地表热通量资料在伊朗-青藏高原地区的对比分析	气象科学	2015, 35(4)	
刘建栋(第2)	华北冬小麦品种演变过程中 CO ₂ 补偿点变化分析	气象与环境学报	2015, 31(1)	
刘煜	一个求解云滴谱相对离散度的方法	中国科学: 地球科学	2015, 45(5)	
刘黎平(第2)	基于区域跟踪的增雨效果分析方法新探	暴雨灾害	2015, 34(1)	
刘黎平(第2)	基于雷达回波概率特征的雷达部分遮挡区域识别算法	高原气象	2015, 34(2)	
刘黎平(第2)	C 波段车载双偏振雷达 ZDR 资料处理方法研究	高原气象	2015, 34(1)	
刘黎平(第2)	人工增雨催化区跟踪方法与效果评估指标研究	气象	2015, 41(1)	
刘黎平(第2)	基于模糊逻辑的大气云粒子相态反演和效果分析气象	气象	2015, 41(2)	
刘黎平等	2014 年青藏高原云和降水多种雷达综合观测试验及云特征初步分析结果	气象学报	2015, 73(4)	
刘黎平等	X 波段一维扫描有源相控阵天气雷达测试定标方法	应用气象学报	2015, 26(2)	
齐艳军等	与中国东部天气气候相关的大气季节内振荡研究及业务应用	热带气象学报	2015, 31(4)	
宇如聪(第2)	中国大陆雨季时空差异特征分析	气象学报	2015, 73(1)	
安兴琴(第2)	污染源减排时刻和减排比例对北京市 PM _{2.5} 浓度的影响	中国环境科学	2015, 35(7)	
阮征	降水回波谱参数估算雨滴谱参数的算法研究	高原气象	2015, 34(4)	
阮征(第2)	垂直探测雷达的降水云分类方法在北京地区的应用	高原气象	2015, 34(3)	
阮征(第2)	风廓线雷达估测降水云中大气垂直速度的一种方法	高原气象	2015, 34(3)	

作者 Author (rank)	题名 Title	出版物名/出版社 Publication name or Publisher	年,卷(期) Year, Volume (Issue)	备注 Notes
阮征等	C 波段调频连续波天气雷达探测系统及观测试验	气象学报	2015, 73(3)	
苏正军(第3)	关于人工影响消减雾霾的思考	科技导报	2015, 6	
李宏宇	利用声学方法采集人工影响天气高射炮作业数据	应用气象学报	2015, 26(5)	
李英(第2)	台湾地形对台风 Meranti (1010) 经过海峡地区时迅速增强的影响研究	大气科学	2015, 39(4)	
李英(第2)	孟加拉湾风暴费林(1302)对藏南一次暴雪过程的影响分析	气象	2015, 41(9)	
李建(第2)	横断山系云岭余脉点苍山东西侧小时降水特性对比	气象	2015, 41(1)	
杨建莹等	西南地区水稻洪涝等级评价指标构建及风险分析	农业工程学报	2015, 16	EI
吴玲燕	大气中 SO ₂ 和 HCOOH 在 CaO 表面的耦合相互作用	化学学报	2015, 73(2)	
张人禾	青藏高原 21 世纪气候和环境变化预估研究进展	科学通报	2015, 60(32)	
张人禾(第2)	中国冬季积雪变异及其与北极涛动的联系	大气科学	2015, 39(3)	
张人禾(第2)	2013 年 5 月华南强降水与中国南海夏季风爆发	气象学报	2015, 73(3)	
张阳(第2)	两种类型 M 分量物理特征和机制对比	应用气象学报	2015, 26(4)	
陈军明(第2)	多普勒天气雷达资料同化对江淮暴雨模拟的影响	应用气象学报	2015, 26(5)	
林祥等	近百年来的南极绕极波变化特征	气候与环境研究	2015, 20(1)	
罗亚丽(第2)	青藏高原、中国东部及北美副热带地区夏季降水系统发生频次的 TRMM 资料分析	气象	2015, 41(1)	
罗亚丽(第2)	CMORPH 卫星-地面自动站融合降水数据在中国南方短时强降水分析中的应用	热带气象学报	2015, 31(3)	
罗亚丽(第2)	基于多信息源的强降水过程综合分析	人民长江	2015, 46(8)	
周广胜	气候变化对中国农业生产影响研究展望	气象与环境科学	2015, 38(1)	
周广胜	生态医生——脆弱性评价与适应性管理	生命世界	2015, 2	
周广胜(第2)	内蒙古地带性针茅植物对 CO ₂ 和气候变化的适应性研究	生态学报	2015, 35(14)	

作者 Author (rank)	题名 Title	出版物名/出版社 Publication name or Publisher	年,卷(期) Year, Volume (Issue)	备注 Notes
周广胜(第2)	1961—2010年中国橡胶寒害的时空分布特征	生态学杂志	2015, 34(5)	
周广胜(第2)	夏玉米叶片含水率及光合特性对不同强度持续干旱的响应	生态学杂志	2015, 34(11)	
周广胜(第2)	基于涡度相关的春玉米逐日作物系数及蒸散模拟	应用气象学报	2015, 26(6)	
周广胜(第2)	未来气候变化对中国天然橡胶种植气候适宜区的影响	应用生态学报	2015, 26(7)	
周广胜(第2)	中国橡胶树种植气候适宜性区划	中国农业科学	2015, 48(12)	
周广胜(第3)	温度与降水协调作用对短花针茅生物量及其分配的影响	生态学报	2015, 35(3)	
周广胜等	陆地生态系统对气候变化的脆弱性评价与适应性管理	中国基础科学	2015, 3	
周秀骥(第2)	一种改进的 TSI 3563 积分浊度误差校正方法	应用气象学报	2015, 26(1)	
周秀骥(第2)	气候系统 10 万年周期变化的随机动力学模拟	中国科学	2015, 45(5)	
周凌晞(第2)	不同源汇信息提取方法对区域 CO ₂ 源汇估算及其季节变化的影响评估	环境科学	2015, 36(7)	
郑向东(第2)	龙凤山和瓦里关臭氧总量异常变化与天气过程关系研究	北京大学学报: 自然科学版	2015, 51(4)	EI
郑向东(第2)	风云-3A 卫星 TOU 臭氧总量的地基验证分析	空间学报	2015, 35(6)	EI
郑向东(第2)	大气低压模拟舱研制与初步应用	气象科技	2015, 43(1)	
郑向东(第2)	西藏当雄地基紫外线指数观测研究	应用气象学报	2015, 26(4)	
宝兴华	WRF-EnKF 系统对中国南方一次暴雨过程确定性预报的试验	气象	2015, 41(5)	
房世波	近 50 年来中国东、西部地面太阳辐射变化及其与大气环境变化的关系	物理学报	2015, 64(8)	SCIE
孟昭阳等	2013 年夏季华北乡村站点固城大气氨变化特征	应用气象学报	2015, 26(2)	
赵俊芳等	基于干热风危害指数的黄淮海地区冬小麦干热风灾损	生态学报	2015, 35(16)	
赵俊芳等	近 50 年东北地区 $\geq 10^{\circ}\text{C}$ 农业热量资源对气候变化的响应	自然灾害学报	2015, 24(3)	
赵琳娜	北京降雨过程分型特征及短历时重现期研究	暴雨灾害	2015, 34(4)	

作者 Author (rank)	题名 Title	出版物名/出版社 Publication name or Publisher	年,卷(期) Year, Volume (Issue)	备注 Notes
赵琳娜	黄淮地区夏季日降水分区概率预报方法研究	气象	2015, 41(12)	
赵琳娜	观测资料概率不确定性对集合预报概率 Brier 技巧评分结果的分析	应用气象学报	2015, 26(6)	
俄有浩等	北方春小麦种植区小麦种植结构变化的气候依据与冻害风险	自然灾害学报	2015, 24(5)	
施晓晖(第3)	山东半岛冷流强降雪和非冷流强降雪的对比分析	气象	2015, 41(5)	
施晓晖等	中国持续性暴雨特征及青藏高原热源的影响	高原气象	2015, 34(3)	
祝从文(第2)	冬季北太平洋海温主模态在 1990 年前后调整及其成因初探	大气科学	2015, 39(5)	
姚波(第2)	中国区域 HCFC-142b 排放量模式反演研究	中国环境科学	2015, 35(4)	EI
姚雯等	秒级探空数据随机误差评估	应用气象学报	2015, 26(5)	
袁乃明(第2)	长时间大气温度序列的外部变化趋势判别研究	物理学报	2015, 64(2)	SCI
徐晓斌(第2)	华北平原夜间对流性天气对地面 O ₃ 的抬升效应	应用气象学报	2015, 26(3)	
郭学良(第2)	2011—2013 年中国冻雨、冻毛毛雨和冻雾的特征分析	大气科学	2015, 39(5)	
郭学良(第2)	华北一次积层混合云微物理和降水特征的数值模拟与飞机观测对比研究	大气科学	2015, 39(2)	
郭学良(第2)	利用地基多通道微波辐射计遥感反演华北持续性大雾天气温、湿度廓线的检验研究	气象学报	2015, 73(2)	
郭建平	气候变化对中国农业生产的影响研究进展	应用气象学报	2015, 26(1)	
梁钊明等	一次台风变性并入东北冷涡过程的动力诊断分析	大气科学	2015, 39(2)	
梁林林	北京市大气气溶胶中糖类化合物的组成及来源	环境科学	2015, 36(11)	
彭新东(第2)	结合历史资料的数值天气预报误差订正	气象学报	2015, 73(2)	
程巳阳等	北京上甸子大气本底站 CO ₂ 浓度的源汇区域代表性研究	中国环境科学	2015, 35(9)	EI
程兴宏等	2013 年 1 月华北地区重霾污染过程 SO ₂ 和 NO _x 的 CMAQ 源同化模拟研究	环境科学学报	2015, 36(2)	
程兴宏	基于 CMAQ 模式和自适应偏最小二乘回归法的中国地区 PM _{2.5} 浓度动力—统计预报方法研究	环境科学研究	2015, 36(7)	

作者 Author (rank)	题名 Title	出版物名/出版社 Publication name or Publisher	年,卷(期) Year, Volume (Issue)	备注 Notes
程兴宏(第2)	太阳辐射预报滚动订正方法研究	气象科技	2015, 43(1)	
楼小凤等	霰粒子参数对强对流云降水和催化影响	大气科学	2015, 39(3)	
谭凯炎等	高温胁迫对华北地区冬小麦灌浆及产量的影响	生态学报	2015, 35(19)	
霍治国(第2)	1961—2010年长江中下游地区农业洪涝灾害时空变化	地理研究	2015, 34(6)	
霍治国(第2)	海南冬种瓜菜气象灾害风险评估与区划	地理研究	2015, 34(2)	
霍治国(第2)	南方洪涝灾害综合风险评估	生态学杂志	2015, 34(10)	
霍治国(第2)	基于大尺度因子的小麦白粉病长期预测模型	生态学杂志	2015, 34(3)	
霍治国(第2)	海南省辣椒春季干旱灾害等级指标	生态学杂志	2015, 34(11)	
霍治国(第2)	河北省小麦白粉病发生气象等级动态预警	生态学杂志	2015, 34(9)	
霍治国(第2)	10—11月海南省瓜菜苗期湿涝风险评估与区划	应用气象学报	2015, 26(4)	
霍治国(第2)	西南地区农业洪涝等级指标构建及时空分布特征	应用生态学报	2015, 26(8)	
霍治国(第2)	海南冬种瓜菜干旱风险评估与区划	中国农业气象	2015, 36(2)	
霍治国(第2)	典型区域小麦白粉病发生气象等级动态预警模型	中国农业气象	2015, 36(5)	
霍治国(第3)	农业气象灾害风险评估研究进展与展望	气象学报	2015, 73(1)	
魏婷	近期碳排放趋势对气候变化历史责任归因的影响	科学通报	2015, 60(7)	



中国气象科学研究院年报 2015

主办单位：中国气象科学研究院
编辑出版：《中国气象科学研究院年报》编辑部
主 编：端义宏
执行主编：袁凤杰
制作印刷：北京永峰印刷有限责任公司
地 址：北京中关村南大街 46 号，邮编 100081
<http://qikan.camscma.cn>
Email: kjdt@camscma.cn

ANNUAL REPORT OF CAMS 2015

Sponsor: Chinese Academy of Meteorological Sciences
Publication: Annual Report of CAMS Editorial Division
Chief Editor: Duan Yihong
Executive Chief Editor: Yuan Fengjie
Design and Printing: Beijing Yongzheng Printing Ltd. Co.
Address: 46 Zhongguancun Nandajie, Beijing, 100081, China
<http://qikan.camscma.cn>
Email: kjdt@camscma.cn